SYNTHESIS, CHARACTERIZATION, AND APPLICATION OF STARCH AND GRAPHENE OXIDE DERIVATIVES FOR POLYMERS

By

ISHAN NIRANGA, JAYALATH ARACHCHIGE DON

Graduateship in Chemistry
Institute of Chemistry Ceylon
Colombo, Sri Lanka
2012

Master of Science in Analytical Chemistry
University of Colombo
Colombo, Sri Lanka
2016

Submitted to the Faculty of the
Graduate College of the
Oklahoma State University
in partial fulfillment of
the requirements for
the Degree of
DOCTOR OF PHILOSOPHY
December, 2022

SYNTHESIS, CHARACTERIZATION, AND APPLICATION OF STARCH AND GRAPHENE OXIDE DERIVATIVES FOR POLYMERS

Dissertation Approved:

Dr. Frank D. Blum

Dissertation Adviser

Dr. Gabriel Cook

Dr. Christopher J. Fennell

Dr. Jeffery L. White

Ranji K. Vaidyanathan

ACKNOWLEDGEMENTS

I offer my sincere gratitude to my advisor, Prof. Frank D. Blum, for his guidance, motivation, exceptional patience, and mentoring during my time as a graduate student. Also, I am very grateful to my graduate committee, Dr. Ranji Vaidyanathan and Dr. Bhishma R. Sedai, for their support and cooperation during my research.

Special thanks go to Kevin Keith, Haylie Keith, and MITO Material Solutions, for partially funding my research work. I would also like to thank all the faculty and staff members of the Department of Chemistry, Oklahoma State University, for their help and friendship.

I am also grateful to my fellow researchers, Dr. Ugo Arua, Reza Y. Azarfam, and Anuj Maheshwari, for their support, kind motivational words, and excellent collaboration during my time in the lab. Finally, I would like to thank my parents, brother, wife (Lakjayani), and all of my friends who gave me invaluable support, encouragement, love, and motivation during my doctoral studies.

Name: ISHAN NIRANGA, JAYALATH ARACHCHIGE DON

Date of Degree: DECEMBER, 2022

Title of Study: SYNTHESIS, CHARACTERIZATION, AND APPLICATION OF STARCH AND GRAPHENE OXIDE DERIVATIVES FOR POLYMERS

Major Field: CHEMISTRY

Abstract: Graphene oxide (GO) and starch have often been tested for use as fillers, additives, and interfacial modifiers for polymer composites. However, using pristine GO and starch has several drawbacks, including dispersion constraints resulting in incompatibility with hydrophobic polymers, low reactivity, and agglomerations. To overcome these drawbacks, GO and starch can be chemically modified to increase their compatibility with polymers to meet the requirements for various applications.

Polyhedral oligomeric silsesquioxane (POSS) is a class of molecules with good potential as a modifier for starch and GO. However, limited attention has been paid to using POSS-modified starch and GO as an additive or filler for polymers. Once grafted to the starch and GO, aminopropylisobutyl POSS (POSS-NH_2) is a hydrophobic molecule that can play an important role in composite materials. This family of molecules can increase the hydrophobic characteristics of starch and GO by breaking internal hydrogen bonds and facilitating effective dispersion in the a wider variety of resins. Once a filler has been mixed with resin, the van der Waals attractions between the isobutyl groups and the resin improve the dispersion, which yields improved mechanical properties, including strength, modulus, and toughness. The silica core is a cage that can act as a “heat sink”, reducing the thermal conduction in the composites and increasing its thermal stability. POSS-modified starch and GO were characterized using ^{1}H NMR, FT-IR spectroscopy, thermogravimetric analysis, X-Ray diffraction analysis (XRD) and elemental analysis. The chemically modified materials were dispersed in epoxy resin using a shear mixer that is feasible for use in industrial setups. The thermo-mechanical properties of the neat and filler/additive-loaded resins were studied as a function of different filler/additive loadings using a dynamic mechanical analyzer (DMA).

The interphase between reduced graphene oxide (rGO) and polyvinyl pyrrolidone (PVP) is critical in the behavior of its composites. The thermal behavior of PVP on rGO suggested that a tightly bound polymer existed on the rGO surface that had a much broader glass transition compared to the bulk polymer. The quantification of this polymer fraction suggests that the amount of tightly bound polymer on the rGO was approximately 0.84 mg PVP/m^2 rGO surface.

TABLE OF CONTENTS

LIST OF TABLES

LIST OF FIGURES

Figure Page

Figure Page

Figure Page

Figure Page

CHAPTER I

INTRODUCTION, BACKGROUND, AND METHODS FOR STARCH BASED DERIVATIVES

1.1 POLYMER COMPOSITES

Polymer composites combine two or more chemically or physically different materials to create a material with different, hopefully, better properties. Composites are often composed of continuous (matrix/polymer) and discontinuous (additives/fillers/reinforcement) phases. Numerous choices are available for matrix materials, including polymers, metals, ceramics, etc. The main function of the matrix is to transfer the load and protect the discontinuous phase. The discontinuous phase is often comprised of fiber or filler, such as glass fibers, carbon fibers, natural fibers, inorganic fillers, and carbon fillers. The reinforcements mainly function as the load-bearing component of the composite.

The interface between the matrix and the reinforcement shows heterogeneous characteristics specific to each component and plays a vital role in the overall properties of the composite. Most importantly, appropriate interactions and adhesion in the interfacial layers are required for efficient stress transfer during load-transfer applications. However, the inherent incompatibility of the organic and inorganic materials often used as matrixes and reinforcements, ultimately results in weak adhesion between the two phases. Therefore , interphase modifier are often used to increase compatibility and obtain composites with superior characteristics. Starch has shown good potential as an additive and interfacial modifier for polymer matrixes and fiber-reinforced composites.[1,2] However, the use of pristine starch has several drawbacks, including incompatibility with hydrophobic polymers, low reactivity, dispersion problems, and moisture absorption.[3] The following sections of Chapter 1 briefly summarize some of the background and work done so far to increase the compatibility of starch used as additives in polymer composites.

1.2 STARCH AND POLYMER COMPOSITES

Starch is a highly abundant carbohydrate polymer comprised of amylose and amylopectin molecules. The monomer unit of starch is called α-D-glucose, which forms 1-4-α-(amylose) and 1-6-α-linkages (amylopectin) to make a polymeric starch molecule. The numbering system of starch carbon atoms, chemical structures, and schematic representation of amylose and amylopectin components of starches are shown in Figure 1.1.

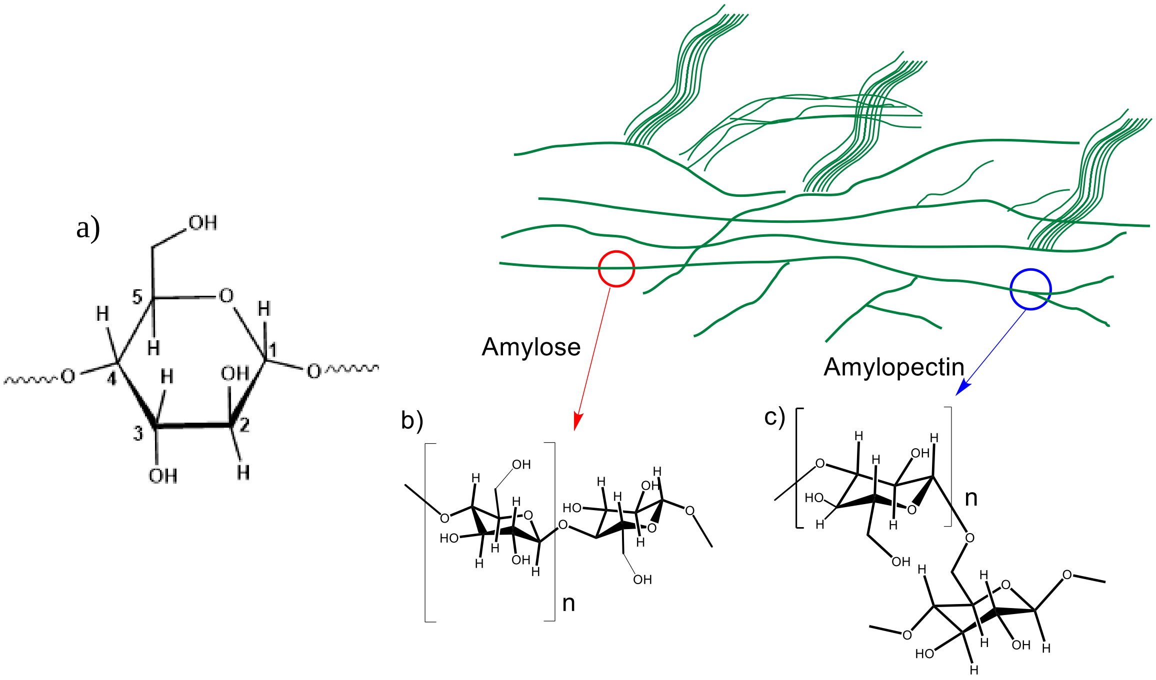

Figure 1.1. a) The numbering system of starch, the chemical structure of b) linear starch (amylose) and c) branched starch (amylopectin) molecule.

Starch is a condensation polymer formed from the condensation of glucose units that have several characteristics similar to conventional synthetic polymers. Starch is available as granules containing both amorphous and crystalline regions, where crystallinity results from the ordered structures of long-length amylopectin branches.[4] The amorphous regions of the starch are primarily made by amylose molecules. The properties of the amorphous regions are unique to a specific polymer that contributes to its glass transition temperature (T_g). However, determining the T_g of dry starch is difficult due to its small thermal sensitivity. In addition, the presence of plasticizers, such as water, significantly changes its properties.[5] The crystalline regions of starch tend to melt at higher temperatures than where amorphous regions decompose. Therefore, the estimation of the melting temperature is challenging due to the thermal degradation of starch molecules below their melting point.

There are numerous types of starches commercially available at reasonable costs, including those from corn, rice, wheat, and potato.[6] These starches have different characteristics, such as moisture content, crystallinity, and amylose/amylopectin ratio. Amylopectin is similar to amylose except that it has a 1-6-α-linkages compared to 1-4-α-linkages in amylose. The amylose/amylopectin ratio of starches varies depending on their source and processing conditions.[7] Most commercial starches contain approximately 20–30 wt% of amylose, although some processed starches and genetically modified products contain up to 70 wt% amylose.[8]

The use of high-amylose corn starches (HACS) has several advantages over amylopectin-rich starches, including ease of dispersion in solvents, ease of chemical modification, better thermal stability, and low viscosity after gelatinization.[9,10] Commercially, corn starch is readily available on the market and it has a market share of approximately 80% of all starches.[7] The HACS consist up to 70% glucose units bonded with 1-4-α-linkages to produce linear molecules. However, 30% of the glucose units are bonded by 1-6-α-linkages to make side chains, yielding branched molecules. The side chains can range from 4–100 monomer units.[9,11] Naturally formed amylose molecules produce a stiff left-handed single helix or a left-handed double helix.[8] A schematic representation of the single and double helix structures of starch is shown in Figure 1.2.

In the helix structure, the hydroxyl groups of starch molecules at positions 2 and 6 point out from the helix while the hydroxyl groups at position 3 point inward.[8,12] As a result, the inner core of the helix is more hydrophobic than its outer regions. Also, the hydroxyl groups at positions 2 and 6 are more susceptible to modification reactions than the hydroxyl groups at position 3 carbon atom.[8,12]

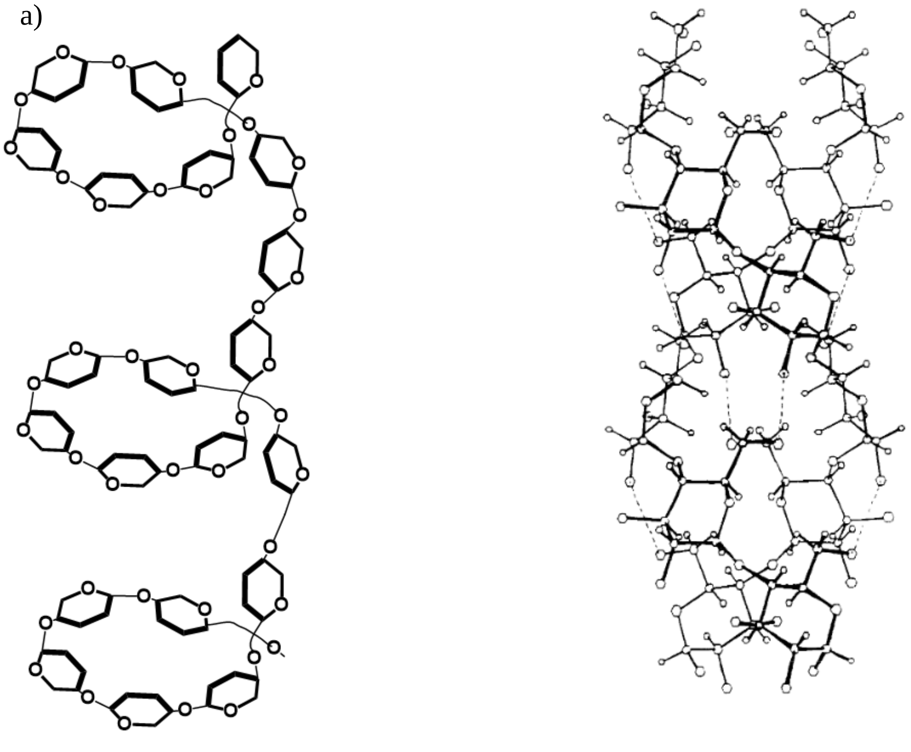

Figure 1.2. a) The single helix b) the double helix structure of starch. From Imberty et al.[8]

The molecular mass of the starch plays an important role in the synthesis of starch-based additives and their application in polymer composites.[13] Size exclusion chromatography (SEC) coupled with a laser light scattering (LLS) detector is widely used to estimate the molecular mass and degree of polymerization of the starch.[14] SEC separates macromolecules based on their hydrodynamic volumes. The LLS detector determines the size of the molecule by measuring the angular variation of the scattered light. According to Rayleigh's theory, the intensity of light scattering is specific to a particular polymer, size, and molecular mass. The average molecular mass (M_w) of the HACS decreases with the increased amylose content of the starch.[9] The M_w of HACS falls in a narrow range from 4×10^5 to 7×10^5. The M_w for the 70% HACS that we used in our work is approximately 6×10^5 g/mol according to the provider's specifications.[9]

The crystallinity of amylose-rich starch is another important characteristic of starch. There are different types of crystal structures: types A and B, or cereal and tubular, respectively.[8,12] The third type is a hybrid of types A and B, called type C (or Vh) crystallinity. The X-ray diffraction (XRD) spectra of the three types of starches are shown in Figure 1.3a.

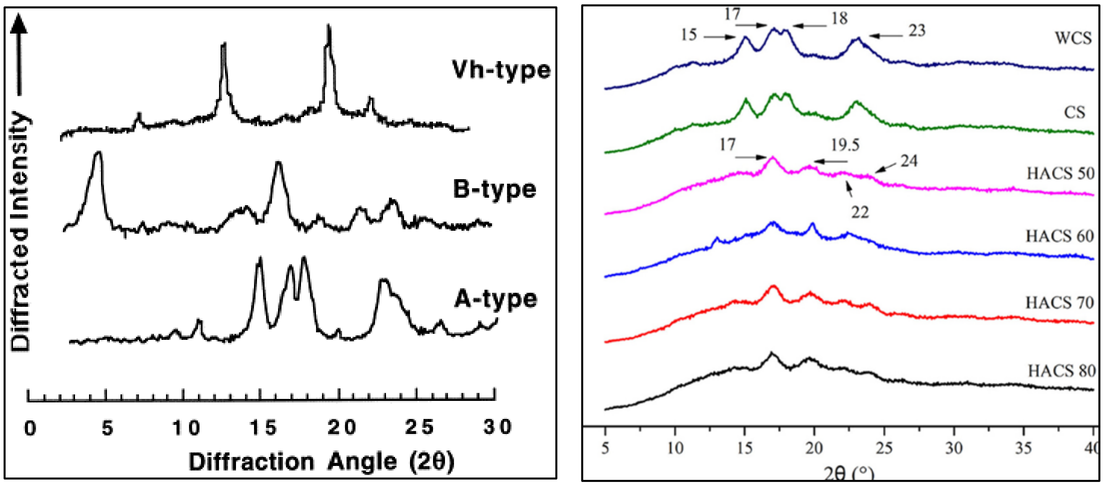

Figure 1.3. a) The XRD patterns of A B and V type starch crystal structures, and b) the variation of crystallinity of HACS with amylose content. From Lv et al.[9]

The amylose content in corn starch can be estimated based on its crystallinities from XRD analysis. The XRD spectra of waxy corn starch (WCS), corn starch (CS), and HACS has shown in

Figure 1.3b indicates the types of crystallinity for each.[9] The crystallinity results from the amylopectin side chains and the amount of crystallinity changes with increased amylose content. Therefore, as amylose content increases, the crystallinity decreases due to decreased molecular mass and the reduced number of amylopectin side chains. Based on XRD spectra, high amylose content corn starches can be assigned to type B crystallinity.[9]

1.3 STARCH-BASED ADDITIVES FOR POLYMERS

Starch is a biodegradable, renewable, and readily available natural polymer that has a proven ability to reinforce resins.[15] Therefore, starch is a promising candidate to replace more expensive materials such as graphene and petroleum-based additives that are currently used in the composites industry.[16-19] Various starches have been tested as fillers for polymers and interfacial modifiers for resins, polymers, and fiber-reinforced composites. The different approaches adopted in the literature for using starch in polymer composites will be discussed briefly in the following sections.

1.3.1 Raw starch as an additive in composites

Raw starch has been studied as an additive and filler for polymers and resins. Starch has been used as an additive for pre-vulcanized natural rubber latex composites that ultimately have partially biodegradable composites.[20] The biodegradability of the material was studied by a soil burial test and measured the effect of biodegradation on the tensile strength of the overall composite. The biodegradation of the material was carried out over 10 weeks and tested for the tensile strength of the composites.[20] The study suggested that the tensile strength of the composites after one week under the soil was drastically reduced due to the biodegradation of starch in the composite.

Composites made using starch and PP by injection molding have shown that increased starch content has a detrimental effect on tensile strength.[21] The results were interpreted as due to (1) Weak interphase adhesion occurring between the hydrophilic starch and the hydrophobic PP in the composite. (2) Spherical crystalline structure of the raw starch which caused poor dispersion in the PP matrix. However, these results showed increased tensile modulus, flexural strength, and flexural modulus for the PP composites. The melting temperature, the heat of fusion, and the percentage crystallization of PP were increased with starch content. Starch was tested as a stiffening agent for jute yarn-reinforced PP composites.[22] The composites showed improved mechanical properties, such as increased tensile strength and modulus, at the cost of higher water uptake capacity. As a result of moisture adsorption, the composites showed reduced mechanical strength over time.

Starch has been used effectively as a biodegradable additive in poly(propylene carbonate) (PPC) composites.[23] A series of starch–PPC composites have been made by increasing starch content from 35–70% by weight. The biodegradation of starch composites has been studied for over 180 days using a soil burial test. The possible degradation mechanism of the composites was believed to involve three steps: colonization by microorganisms, degradation of the starch, and degradation of PPC. The degradation results suggested that the composites with more than 50% starch loading degraded more than 50% in 80 days. Starch has been used as an additive for PPC composites that were made using a hot-melt method with a twin rotary mixer.[24] The effect of starch loading (10%, 20%, and 30%) on the thermal stability and T_g of the PPC were studied using thermogravimetric analysis (TGA) and dynamic mechanical analysis (DMA). The addition of 30% starch increased the degradation temperature of PPC from 226 to 296 °C; that is, by approximately 70 °C. From mechanical studies, the tan (δ) vs. temperature plot showed T_g increased by 6 °C, suggesting the miscibility of starch with PPC.

The interactions between starch and PPC in their composites have been studied using density functional theory (DFT)-based B3LYP, semi-empirical AM1, and PM3 methods.[25] Their results showed the hydrogen bonding interactions between the carbonyl group of the PPC polymer and the hydroxyl group of the starch molecules. Fourier-transform infrared (FTIR) spectra of the composites have shown the shift of the hydroxyl band from 3397 to 3391 cm^{-1}.

1.3.2 Starch derivatives as fillers and interfacial modifiers

Extrusion processing is a fundamental method that is widely used in the industry for preparing physically modified starch derivatives. In this method, the starch undergoes a thermomechanical process that changes its microstructures. The processing is conducted above the gelatinization temperature of the starch, which causes breakage of the intermolecular and intramolecular interactions, such as hydrogen bonding. During this process, the crystallinity of the starch decreases, and the starch molecules swell.[15] The processing conditions such as temperature, and time depend on the source of starch and water content. The extrusion-processed starch is used as a raw material for chemical reactions due to its ease of dispersion and ability to carry out grafting reactions.

Starch can be chemically modified to increase its compatibility with hydrophobic polymers and resins when extrusion processing cannot meet the requirements for applications. Morantes et al.[26] have reported the synthesis of positively charged nanocrystals (CNC) by activating the primary alcohol groups of the CNC by sodium hydroxide (NaOH) and subsequent attack on the epoxide group of epoxypropyltrimethylammonium chloride (EPTMAC). The physical properties of the starch, such as shape, structure, and crystallinity, were unaffected after the modification.[26]

The hydrophobic modification of starch with long-chain hydrocarbons has been used to reduce the hydrophilic character of the starch.[27-33] Lauryl chloride has successfully been tested as a potential organic molecule for the hydrophobic modification of cellulose.[27] The sessile drop water contact angle on modified starch was 78° and was significantly larger than that of raw starch. The performance of modified starch in the epoxy resin was tested using DMA. The modified starch showed an excellent reinforcing ability, increasing the tensile strength and flexural modulus of the epoxy resin.

The grafting of plant-based polyphenols is an environment-friendly approach to increasing the hydrophobic characteristics of CNC,[29] and the reaction was performed in the presence of NaOH. The modified starch was characterized using FTIR spectroscopy, ^{1}H nuclear magnetic resonance (NMR) spectroscopy, X-ray fluorescence (XRF), and X-ray photoelectron spectroscopy (XPS). The degree of substitution of polyphenols on starch was not estimated in the study. However, the change in crystallinity of starch after the grafting was determined by XRD analysis. The results showed that the chemical modification did not significantly disturb the crystalline structure of starch. Most importantly, the modified starch showed a sessile drop water contact angle of 74°.

The grafting of octyl succinic acid (OSA) to starch has been studied several times.[30,34] Hydrophobically modified starch using OSA was studied its effects on emulsification using multiple light scattering and particle size analyses were performed. Potato starch was modified by OSA to increase its compatibility with polymers.[28] The work optimized the reaction conditions, including temperature, time, pH, and the ratio of starch to OSA. The crystallinity of starch remained unaffected. Another study[31] has shown that after the modification of starch using ring-opening polymerization of e-caprolactone, starch-grafted polycaprolactone (starch-g-PLC) showed a sessile drop water contact angle of 75° on modified starch.

The low reactivity of starch alcohol groups is a major drawback of starch-based additives. Therefore, to address reactivity limitations, starch can be modified with organic molecules in which the functional groups react with the matrix and resin during curing. Based on the literature, epoxidation of starch is a common approach used to increase the reactivity of starch with resin. The use of epoxy-modified starch has been tested in several studies as an additive for poly(lactic acid) (PLA). In another study[35] it was demonstrated that epoxy-modified starch dispersed efficiently in a PLA matrix, resulting in superior mechanical and thermal properties. The starch was modified using epoxidized itaconic acid (EIA) or epoxidized cardanol (Epicard) in the presence of the catalyst tetrabutylammonium bromide (TBAB). This modification of starch resulted in increased hydrophobicity and interfacial adhesion between starch and PLA. Differential scanning calorimetry (DSC) was used to study the effect of the modified starch on PLA crystallization. The pure PLA did not show any crystallization during the first cooling curve. However, the second cooling step showed a crystallization peak at 104 °C for the PLA. Starch–PLA composites showed a sharper crystallization peak for PLA that shifted to 100 °C in the presence of modified starch. Therefore, this study suggests that modified starch particles may have behaved as nucleation sites to promote PLA crystallization. In another work[36] epoxidized soybean oil (ESO) has been used as a plasticizer for the maleic acid–modified starch to increase the toughness of the PLA composites. The ESO-blended composites have shown a 140% increase in elongation at break and a 5% increase in impact strength. ESO and glycerol have successfully been used as surface modifiers and plasticizers for thermoplastic starch.[37] The resultant composites have shown increased hydrophobicity with a significant difference in equilibrium water uptake compared to raw starch. The amylose-to-amylopectin ratio plays a vital role in the adhesion of epoxy-modified starch.[38] The epoxidation reaction favorably occurred in higher amylopectin starch, resulting in the highest degree of substitution and higher viscosity than the amylose starch reaction. That study could not identify a clear boundary of the effect of amylose/amylopectin content on mechanical properties. However, the mixture of amylose and amylopectin behaved differently than starches with high amylose or high amylopectin content.

1.4. CORN STARCH MODIFIED BY POSS

The ring–opening of epoxides by alcohols is an important type of reaction in organic synthesis.[39] In this reaction mechanism, the activation of the epoxide group takes place with an acid or base catalyst and the subsequent attack of nucleophiles to open the epoxide ring. Under basic conditions, the leaving group is the alkoxide anion, which is a weak leaving group. As a result, the nucleophile induces ring–opening due to the ring strain of the epoxide. In asymmetrically substituted epoxides, the major product results from an S_N2 reaction, where nucleophiles attack the less hindered carbon atom of the epoxide ring followed by the protonation to produce an alcohol.[40] Based on the mechanism, nucleophiles attack from the backside of the electrophilic carbon, and inversion of the stereocenter takes place. However, the acid-catalyzed reactions are considered borderline S_N2 type reactions, where nucleophiles attack the more substituted carbon atom. More-substituted carbons have more hyperconjugation than less-substituted carbon atoms. Several studies have been carried out to investigate the activation of alcohol groups as leaving groups for the nucleophilic substitution reaction by heteroatoms.[41,42]

1.4.1 Aluminum triflate as a potential catalyst for ring opening of the epoxide

$Al(OTf)_3$ has been used for the ring opening of styrene oxide by various alcohols.[39] The reactions were performed in a polar solvent (methanol) with a range of catalyst loadings compared to styrene oxide. The reaction product was a glycol ether, in which the methanol nucleophile attacks the most substituted carbon atom. The major side product of the reaction was the oligomer resulting from the self-polymerization of styrene oxide. Oligomer formation was facilitated by the amount of heat and duration of the reaction. The best reaction conditions for the smallest amounts of by-products were 0.002% catalyst loading with reflux in methanol.

Aluminum triflate (Al[OTf]$_3$) has been reported as an efficient catalyst for the ring opening of epoxides by molecules including alcohols, amines, and thiols.[39,41-44] Gohain et al.[42] have shown the direct nucleophilic substitution of the propargylic alcohol group by several heteroatom-centered nucleophiles in the presence of Al(OTf)$_3$. The hydroxyl group of propargylic alcohol has been displaced by the amine nucleophile in the presence of Al(OTf)$_3$. The alkene group of propargylic compounds makes the hydroxyl a better leaving group due to the resonance structure of the resultant carbocation. The reaction has proven to be efficient in high-polarity solvents, such as acetonitrile. The catalytic mechanism of Al(OTf)$_3$ is important for optimizing reaction conditions of an unknown reaction, such as that between starch and octaglycidyl polyhedral oligomeric silsesquioxane (OGPOSS). Therefore, the ring–opening of butene oxide by methanol was studied to understand the mechanism by computational methods.[44] Based on these molecular modeling studies, the proposed mechanism of ring opening of butene oxide by methanol in the presence of Al(OTf)$_3$ is shown in 1.4.

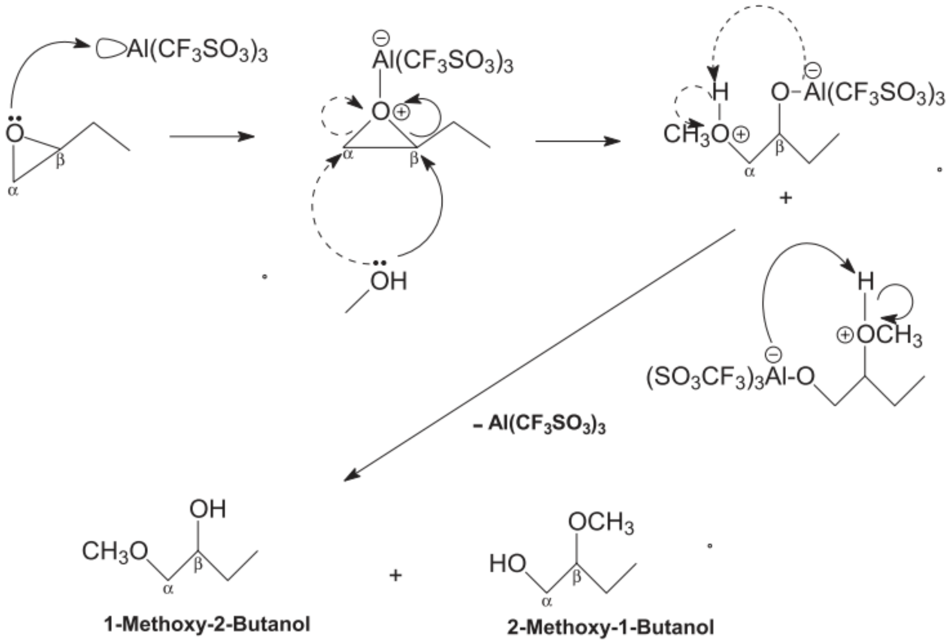

Figure 1.4. Proposed mechanism of butene oxide ring–opening by methanol. From Terblans et al.[44]

Based on the mechanism, the epoxide oxygen coordinates with the aluminum ion to form the intermediate. Then, the nucleophile attacks the less-substituted carbon atom of the epoxide, and the regeneration of the catalyst takes place. In general, ring-opening reactions are highly exothermic due to the release of the ring strain. In $Al(OTf)_3$ catalyzed reactions, regeneration of the catalyst after the coordination to the epoxide is slightly endothermic. The ring-opening step also has low activation energy. As a result, $Al(OTf)_3$ shows very high efficiency for the ring–opening under such a small catalyst load in the reaction.

1.4.2 Bicyclic amidine catalysts

Bicyclic amidine catalysts have also been used for the ring opening of epoxides by several nucleophiles, including amines and thiols.[45] Baidya and Mayr[2] have studied the Lewis basicity and nucleophilicity of bicyclic amidines. The nucleophilicity and Lewis basicity of this series of catalysts to the C_{sp2} centers have been estimated in their study. The nucleophilicity is a kinetic parameter that is determined based on the reaction rate toward a common substrate. The Lewis basicity is a thermodynamic factor estimated using an equilibrium constant. The nucleophilicity and Lewis basicity of 4–dimethylaminopyridine (DMAP), 1,8-diazabicyclo[5.4.0]undec-7-ene (DBU), 1,5-diazabicyclo[4.3.0]non-5-ene (DBN), and 1,4-diazabicyclo[2.2.2]octane (DABCO) is important for understanding the reaction profile. The nucleophilicity increases from DMAP $<$ DBU $<$DBN $<$ DABCO while Lewis basicity increases DABCO $<$ DMAP $<$ DBU $<$ DBN.

DABCO possesses unique characteristics and can act as a highly efficient catalyst in the ring opening of epoxide reactions. DABCO has been used in the ring opening of epoxides with amines and thiols.[45] In that study, the reactions were conducted at room temperature in an aqueous medium within 12 h with a 98% yield. In the asymmetrically substituted epoxides, the nucleophile attacked the less-substituted carbon atom.[45] The study investigated the effect of the temperature and polarity of solvents (THF, toluene, water, and DMF) on the yield of the product. Several reactions performed efficiently in the presence of 1% catalyst loading and had good to excellent yields.[46] In a typical mechanism, the amidine catalyst activates the nucleophile through hydrogen bonding with the nitrogen or sulfur atom of the nucleophile. Then the nitrogen or sulfur nucleophile attacks the epoxide ring at the least substituted carbon atom. In the final step, the regeneration of the catalyst occurs due to the abduction of a proton from the epoxide oxygen by the catalyst.

Starch is composed of bio-macromolecules that do not dissolve in organic solvents. Therefore, catalytic systems reported for small organic molecules do not give the expected results on starch. In such situations, the reactivity of starch is increased by introducing carboxylic and carbonyl functional groups by the oxidation of starch. The oxidation of starch is briefly discussed in the next section.

1.4.3 Oxidation of starch

Starch modification reactions have more constraints than conventional organic reactions due to the low reactivity of the alcohol groups and poor expansion of starch in the solvent. These drawbacks ultimately lead to poor reaction rates and small substitution amounts with the guest organic molecules. The oxidation of starch is widely used to increase the reactivity of raw starch. The amount of oxidation depends on various factors, including the type of oxidation agent, temperature, the origin of the starch, and reaction time. The work in this dissertation used high amylose content corn starch as the starch source. The starch was oxidized using hydrogen peroxide (H_2O_2) in the presence of a metal catalyst, such as Cu^{2+}, Fe^{2+}, and V^{5+} which have been reported extensively in the literature.[47,48] The purpose of oxidation was to increase the reactivity of the starch and use it as a reactant for the grafting reaction with different types of POSS molecules, as discussed in Chapter 3.

During oxidation, the alcohol groups at positions C(1), C(3), and C(6) of starch were oxidized to aldehydes, ketones, and carboxylic acids. The degree of oxidation (DO) can be calculated using acid-base titrimetry using:[49]

$$DO = \left(\frac{0.162 \times (V \times M)/W}{1 - [0.210 \times (V \times M)/W]}\right) \tag{1.1}$$

where V and M are the volume and molarity of sodium hydroxide used for the titration, respectively, and W is the dry weight of raw starch. The oxidation mechanism depends on the type of oxidation agent and the catalyst used for the reaction. The mechanism of starch oxidation using hydrogen peroxide and a metal catalyst is shown in Figure 1.5.

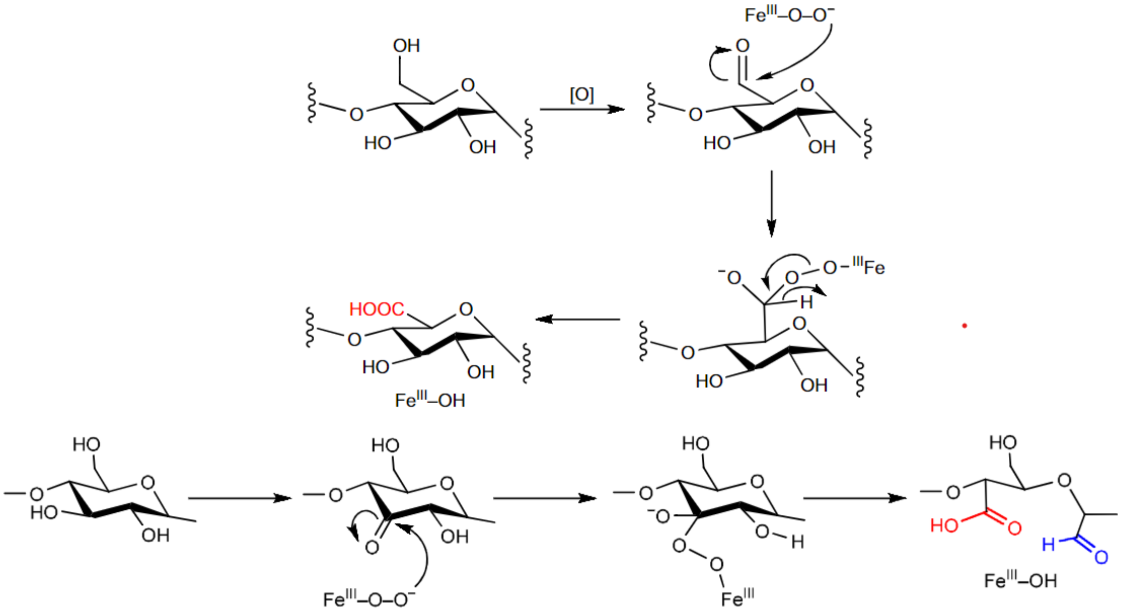

Figure 1.5. Mechanism of starch oxidation using H_2O_2 and a metal catalyst. From Tapio et al.[47]

The oxidation of starch has been widely studied; many different reagents and catalysts have been used. Within the scope of this dissertation, the oxidation of starch using hydrogen peroxide and a metal catalyst will be considered. The oxidized starch has chemical and thermal properties distinct from those of pristine starch. The functional groups introduced during the oxidation make the starch molecules more reactive than the pristine starch. The oxidation of the primary and secondary alcohol groups of starch occurs during the oxidation reaction. However, the thermal stability of the oxidized starch compared to the pristine starch depends on the degree of oxidation (DO) and type of hydroxyl group (primary vs. secondary) involved in the reaction. In general, the thermal stability of oxidized starch is less than raw starch due to depolymerization. The ring–opening of starch, and ultimately the degradation of the polymer molecules, are major drawbacks to this process. However, completing the reaction at lower temperatures over a shorter reaction time should successfully address this concern. The oxidation conditions, effect of oxidation reagent, catalyst concentration on the thermal stability, and DO are reported in Chapter 3. Finally, the oxidized starch was used as a reactant for the grafting reaction for POSS-NH_2.

1.5 EXPERIMENTAL METHODS FOR CHARACTERIZATION

1.5.1. ^1H and ^{13}C nuclear magnetic resonance (NMR) spectroscopy

The ^1H and ^{13}C NMR spectroscopy are powerful, highly reproducible, and widely used methods for determining the chemical identity of hydrogen and carbon atoms in the molecule. For an atom to be NMR active, the spin quantum number of the nucleus must be $I > 0$. In that case, the magnetic moments of the nuclei can show different spin alignments in a magnetic field called spin states. The number of spin states (S) of an atom can be calculated using $S = 2I + 1$ where I is referred to as the spin quantum number. In an external magnetic field (B_o), the Larmor equation gives the precession frequency of the nucleus, v_o (in Hertz) given by:

$$v_o = \frac{\gamma B_o}{2\pi} \qquad (1.2)$$

where γ is the magnetogyric ratio and B_0 is the magnetic field strength that is oriented along the z-axis in the laboratory frame of reference. Based on the equation above, the precession frequency depends on the type of nucleus and the strength of the NMR magnet. E.g., a 9.4 T (400 MHz) NMR magnet yields a smaller proton frequency than 18.4 T (800 MHz) one. The energy difference for example, for spin I=1/2 nuclei between two spin states of an atom, is given by:

$$\Delta E = \frac{\gamma h B_o}{2\pi} \tag{1.3}$$

where h is the plank's constant and ΔE is the energy difference in the two spin states of the nuclei. A further modification of equation 1.3 can account for the shielding of the nuclei resulting in a chemical shift. It is this chemical shift upon which most chemical identification is made.

The chemical characterization of starch, oxidized starch, and starch-grafted POSS hybrid materials was carried out using ^{1}H and ^{13}C nuclear magnetic resonance (NMR) spectroscopy (both I = 1/2 nuclei). NMR spectra were obtained with an Avance 400 MHz NMR spectrometer (Bruker, Ettlingen, Germany). The sample preparation for ^{1}H NMR and ^{13}C NMR was challenging due to the low solubility of the starch, oxidized starch, and starch–POSS hybrid material in the chosen solvents. First, an NMR tube was filled with 0.2 mL of deuterated dimethyl sulfoxide (DMSO–d_6). Then some of the solid samples were packed into the NMR tube containing solvent. Finally, an additional 0.3 mL of DMSO–d_6 was added to the tube and heated at 80 °C for 1 h. Several samples were made in this way and then stored in a desiccator for a week before the ^{1}H or ^{13}C NMR spectra were collected at room temperature. The spectral width, pulse angle, acquisition time, delay time, and the number of scans were selected to obtain a useful NMR spectrum. The chemical shifts of the protons were used to identify the changes that occurred on the starch molecules before and after the reaction with POSS molecules.

1.5.2. Attenuated total reflection-Fourier transform infrared (ATR-FTIR) spectroscopy

ATR-FTIR spectroscopy was used as a primary chemical characterization method of reactants and products throughout this dissertation. In a typical FTIR experiment, the sample (liquid or solid) was placed on an ATR crystal, and moderate pressure was applied by a screw located above the ATR crystal. Then, the background spectrum was collected and subtracted from the sample spectrum. The spectra were recorded using a Nicolet i550 spectrometer (Thermo Scientific, Waltham, Massachusetts, USA) equipped with an ATR diamond. The spectra were collected from 500–4500 cm^{-1}. The ATR-FTIR method is based on the total reflectance and the evanescent wave that can be explained using Snell's law. Two conditions should be satisfied for the total reflection to occur: 1) the refractive index of the second medium (that is, the sample) should be smaller than the first medium (the ATR crystal), and 2) the angle of incident light should be larger than the critical angle, which is calculated using Snell's law, as shown by:[50]

$$\theta_c = sin^{-1}\left(\frac{n_1}{n_2}\right) \tag{1.4}$$

where n_1 and n_2 are the refractive indices of the sample and the ATR crystal, respectively, and θ_c is the critical angle of the incident wave above which total reflection occurs as shown in Figure 1.6.

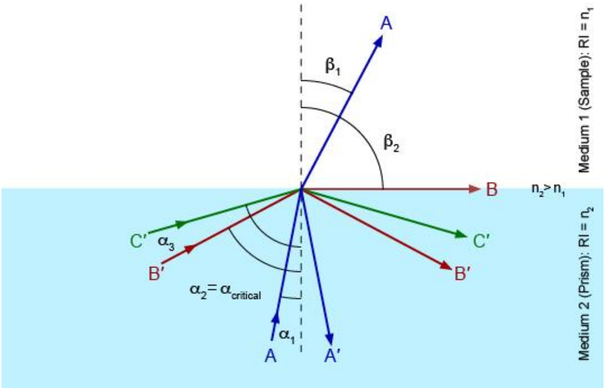

Figure 1.6. Schematic representation of the critical angle, partially reflected, and partially refracted waves. From https://wiki.anton-paar.com/us-en/attenuated-total-reflectance-atr/

During the experiment, IR radiation is directed to a high refractive index crystal, such as diamond, zinc selenide, or germanium. The IR radiation reflects from the inner surface of the crystal and results in an evanescent wave. Part of the evanescent wave is absorbed by the sample, and the transmitted radiation is detected by the detector. A schematic representation of IR absorption by a sample at the ATR crystal surface is shown in Figure 1.7.

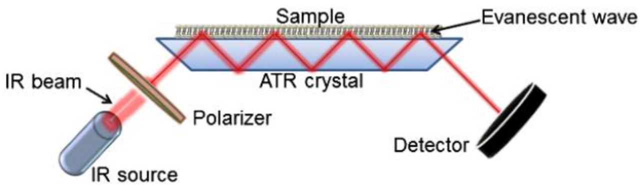

Figure 1.7. Schematic representation of IR absorption of sample on the crystal. From Ausili et al.[51]

The quality of the collected FTIR spectrum depends on several factors. Good contact between the sample and the crystal is important for the proper progress of the evanescent wave through the sample. Therefore, the sample is pressurized using a screw to ensure proper contact is obtained between the sample and the crystal. The penetration depth of the evanescent wave is also important to obtain a high-quality FTIR spectrum. The penetration depth of the evanescent wave is given by:

$$d_p = \frac{\lambda}{2\pi n_1 \sqrt{\mathrm{Sin}^2\theta - \left(\frac{n_1}{n_2}\right)^2}} \tag{1.5}$$

where d_p and λ are the penetration depth of the evanescence wave through the sample and the wavelength of the incident light in the vacuum, respectively.

1.5.3. Contact angle measurement

The contact angle provides useful information on the wettability of solid surfaces. The contact angle is measured where the liquid and vapor phases meet the solid phase. When more than one liquid is involved, the measurement is made using the side of the denser liquid. The water contact angle provides an estimation of the hydrophobic characteristics of the starch after the modification reaction. A small water contact angle indicates the good wettability of the water on a solid surface (hydrophilic surface), and a large contact angle indicates the poor wettability of the liquid (hydrophobic) on the surface. The sessile drop method is one of the most popular and convenient methods for estimating the contact angle of solids.

Pristine starch and graphene oxide were compared with the modified hybrid material to study the effect of the grafting reaction on the hydrophobic characteristics of the material. The contact angle measurements reported throughout this dissertation were determined using the sessile drop method from a custom instrumental setup. The instrumental setup is shown in Figure 1.8.

Figure 1.8. Custom sessile drop contact angle measurement device constructed by Hamid Mortazavian.

1.5.3.1. Experiment procedure

The sessile drop contact angle measurement of a solid material can be divided into three steps. First, approximately 300 mg of the solid material was added to a 3-mm diameter metal mold to obtain a compressed pellet. Then the mold was compressed using a hydraulic press at 15 kPa for 15 min. Second, the compressed pellet was placed on the stage of the contact angle measurement device and 5 μm of distilled water was added using a micropipette. Then the camera focus, height, position, and light were adjusted to obtain a good image of the water droplet. A photograph was taken and saved for data analysis. Finally, the data analysis was performed with ImageJ (NIST) software using the low bond axisymmetric drop shape analysis (LB-ADSA) plug-in.

1.5.4. Dynamic mechanical analysis

The first dynamic mechanical analysis of the viscoelastic properties of material was conducted in 1909 by Poynting.[52] Dynamic mechanical analysis (DMA) provides information on the viscoelastic properties of a material under sinusoidal load or force as a function of temperature, time, or frequency. The working principle of DMA can be summarized as follows: during the experiment, a sinusoidal force is applied to a sample with known geometry (width, length, and thickness). A typical force-displacement curve neat and the additive-loaded epoxy sample is shown in Figure 1.9.

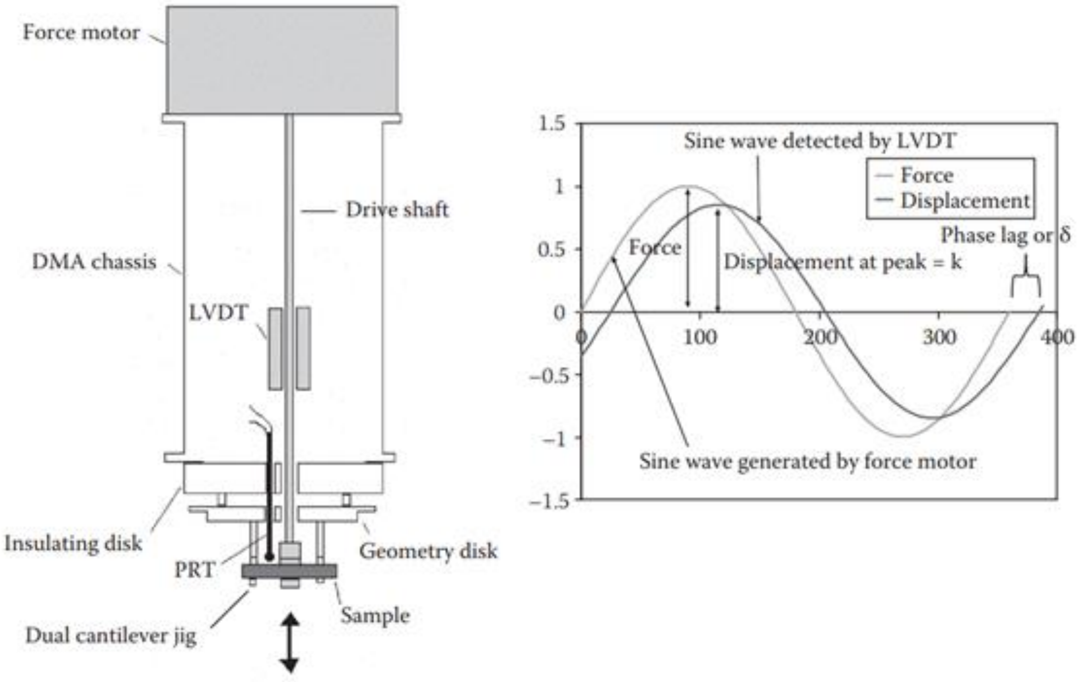

Figure 1.9. The variation of strain with applied sinusoidal applied stress and resultant phase lag. From Menard and Menard.[53]

The sinusoidal stress of the DMA load can be expressed as the following Equation[50,52]

$$\sigma\ (t) = \sigma_0 \sin \omega t \tag{1.6}$$

where ω is the angular velocity of the stress vector equal to 2πf, where f is the cyclic frequency in Hz during sinusoidal oscillations. Both stress and strain are in the same phase for purely elastic materials (no viscous component). Therefore, for a purely elastic response, the strain can be expressed as:

$$\varepsilon\ (t) = \varepsilon_0 \sin \omega t \tag{1.7}$$

However, the strain does not follow the same phase as stress for viscoelastic materials like elastomers. The strain will lag relative to the application of stress due to its viscous nature. Therefore, a time-dependent component should be included in Equation 1.7 The modified stress Equation for elastomers is shown as:[50]

$$\sigma\ (t) = \sigma_0 \sin(\omega t + \delta) \tag{1.8}$$

which can be rewritten as:

$$\sigma\ (t) = \sigma_0 \sin \omega t \cos \delta + \sigma_0 \cos \omega t \sin \delta \tag{1.9}$$

Based on the above analysis, two dynamic moduli can be defined as the real or storage modulus (G') and the imaginary or loss modulus (G''). The imaginary component is 90° out of phase with the real component.

$$G' = \frac{\sigma_0 \cos \delta}{\varepsilon_0} \tag{1.10}$$

$$G'' = \frac{\sigma_0 \sin \delta}{\varepsilon_0} \tag{1.11}$$

Using the definition of storage and loss modulus can be rewritten as follows:

$$\varepsilon = \varepsilon_0\, G' \sin \omega t + \varepsilon_0\, G'' \cos \omega t \tag{1.12}$$

G' and G'' are shown on the phase diagram where G' leads G'' by 90° (Figure 1.9).

The complex modulus (G*) can be expressed as:

$$\mathrm{G}^* = \frac{\sigma}{\varepsilon} = \mathrm{G}' + \mathrm{i}\mathrm{G}'' \tag{1.13}$$

1.5.5. Fixed-frequency temperature sweep DMA experiment

During this experiment, a sinusoidal force is applied to the material in which several parameters, such as frequency and temperature, can be changed. The fixed-frequency experiments of this dissertation were carried out at 1 Hz frequency and room temperature above the T_g of the material with a 3 °C/min temperature ramp rate. The change in temperature in each cycle was insignificant. The experimental results enable the calculation of the modulus of the sample under various temperatures at a fixed frequency. The ratio of stress to strain is a modulus and gives information about the resistance to the deformation of the material (stiffness). In classical mechanical analysis, the slope of the linear part of the stress-strain curve for elongation is called Young's modulus. However, in DMA analysis the moduli calculated from the response of the material to the applied sine wave are the storage modulus (G''), loss modulus (G'), and complex modulus (G^*). These provide more information about the viscoelastic characteristics of the materials.

1.6. MOTIVATION

Starch is a commercially available, highly abundant, and biodegradable carbohydrate that has been widely tested as a potential additive for polymers. However, the hydrophilic characteristics and low reactivity of starch must be addressed before it can be used as an additive for hydrophobic polymer systems. Among several approaches, modification with hydrophobic molecules containing reactive functional groups has huge potential. Aminopropyl isobutyl polyhedral oligomeric silsesquioxane (POSS-NH_2) can be considered one possible candidate for the fabrication of modified starch. After the grafting reaction with starch, the isobutyl groups of POSS-NH_2 have the potential to provide hydrophobic characteristics to the starch. There has also been very limited attention given to the synthesis of POSS-NH_2 grafted starch nanocomposite.[24,54]

1.7. REFERENCES

1. Hsissou, R.; Seghiri, R.; Benzekri, Z.; Hilali, M.; Rafik, M.; Elharfi, A., Polymer composite materials: A comprehensive review. *Composite Structures* **2021,** *262*.

2. Baidya, M.; Mayr, H., Nucleophilicities and carbon basicities of DBU and DBN. *Chemical Communications* **2008,** (15), 1792-4.

3. Altin Karataş, M.; Gökkaya, H., A review on machinability of carbon fiber reinforced polymer (CFRP) and glass fiber reinforced polymer (GFRP) composite materials. *Defence Technology* **2018,** *14* (4), 318-326.

4. Beck, M.; Jekle, M.; Becker, T., Starch re-crystallization kinetics as a function of various cations. *Starch - Stärke* **2011,** *63* (12), 792-800.

5. Liu, P.; Yu, L.; Wang, X.; Li, D.; Chen, L.; Li, X., Glass transition temperature of starches with different amylose/amylopectin ratios. *Journal of Cereal Science* **2010,** *51* (3), 388-391.

6. Le Corre, D.; Bras, J.; Dufresne, A., Starch Nanoparticles: A Review. *Biomacromolecules* **2010,** *11* (5), 1139-1153.

7. Zhang, Z.; Macquarrie, D. J.; Clark, J. H.; Matharu, A. S., Chemical modification of starch and the application of expanded starch and its esters in hot melt adhesive. *RSC Advances* **2014,** *4* (79), 41947-41955.

8. Imberty, A.; Chanzy, H.; Pérez, S.; Bulèon, A.; Tran, V., The double-helical nature of the crystalline part of A-starch. *Journal of Molecular Biology* **1988,** *201* (2), 365-378.

9. Lv, X.; Hong, Y.; Zhou, Q.; Jiang, C., Structural features and digestibility of corn starch with different amylose content. *Frontiers in Nutrition* **2021,** *8* (263).

10. Palanisamy, C. P.; Cui, B.; Zhang, H.; Jayaraman, S.; Kodiveri Muthukaliannan, G., A Comprehensive review on corn starch-based nanomaterials: properties, simulations, and applications. *Polymers (Basel)* **2020,** *12* (9).

11. Wang, S.; Li, C.; Copeland, L.; Niu, Q.; Wang, S., Starch retrogradation: A comprehensive review. *Comprehensive Reviews in Food Science and Food Safety* **2015,** *14* (5), 568-585.

12. Buléon, A.; Colonna, P.; Planchot, V.; Ball, S., Starch granules: structure and biosynthesis. *International Journal of Biological Macromolecules* **1998,** *23* (2), 85-112.

13. Harding, S. E.; Adams, G. G.; Gillis, R. B., Molecular weight analysis of starches: Which technique? *Starch - Stärke* **2016,** *68* (9-10), 846-853.

14. Mua, J. P.; Jackson, D. S., Fine structure of corn amylose and amylopectin fractions with various molecular weights. *Journal of Agricultural and Food Chemistry* **1997,** *45* (10), 3840-3847.

15. Jiang, T.; Duan, Q.; Zhu, J.; Liu, H.; Yu, L., Starch-based biodegradable materials: Challenges and opportunities. *Advanced Industrial and Engineering Polymer Research* **2020,** *3* (1), 8-18.

16. Hung, P.-y.; Lau, K.-t.; Fox, B.; Hameed, N.; Jia, B.; Lee, J. H., Effect of graphene oxide concentration on the flexural properties of CFRP at low temperature. *Carbon* **2019,** *152*, 556-564.

17. Saeb, M. R.; Bakhshandeh, E.; Khonakdar, H. A.; Mader, E.; Scheffler, C.; Heinrich, G., Cure kinetics of epoxy nanocomposites affected by MWCNTs functionalization: a review. *Scientific World Journal* **2013,** *2013*, 703708.

18. Salavagione, H. J.; Martínez, G.; Gómez, M. A., Synthesis of poly(vinyl alcohol)/reduced graphite oxide nanocomposites with improved thermal and electrical properties. *Journal of Materials Chemistry* **2009,** *19* (28).

19. Kuila, T.; Bose, S.; Hong, C. E.; Uddin, M. E.; Khanra, P.; Kim, N. H.; Lee, J. H., Preparation of functionalized graphene/linear low density polyethylene composites by a solution mixing method. *Carbon* **2011,** *49* (3), 1033-1037.

20. Izmar, M. H.; Afiq, M. M.; Azura, A. R., Effects of different additions of sago starch filler on physical and biodegradation properties of pre-vulcanized NR latex composites. *Composites Part B: Engineering* **2012,** *43* (7), 2746-2750.

21. Roy, S. B.; Ramaraj, B.; Shit, S. C.; Nayak, S. K., Polypropylene and potato starch biocomposites: Physicomechanical and thermal properties. *Journal of Applied Polymer Science* **2011,** *120* (5), 3078-3086.

22. Khan, M. A.; Khan, R. A.; Haydaruzzaman; Ghoshal, S.; Siddiky, M. N. A.; Saha, M., Study on the physico-mechanical properties of starch-treated jute Yarn-reinforced polypropylene composites: Effect of gamma radiation. *Polymer-Plastics Technology and Engineering* **2009,** *48* (5), 542-548.

23. Lu, X. L.; Du, F. G.; Ge, X. C.; Xiao, M.; Meng, Y. Z., Biodegradability and thermal stability of poly(propylene carbonate)/starch composites. *J Biomed Mater Res A* **2006,** *77* (4), 653-8.

24. Wang, X. L.; Li, R. K. Y.; Cao, Y. X.; Meng, Y. Z., Essential work of fracture analysis for starch filled poly(propylene carbonate) composites. *Materials & Design* **2007,** *28* (6), 1934-1939.

25. Joshi, S. S.; Mebel, A. M., Computational modeling of biodegradable blends of starch amylose and poly-propylene carbonate. *Polymer* **2007,** *48* (13), 3893-3901.

26. Morantes, D.; Munoz, E.; Kam, D.; Shoseyov, O., Highly charged cellulose nanocrystals applied as a water treatment flocculant. *Nanomaterials (Basel)* **2019,** *9* (2).

27. Trinh, B. M.; Mekonnen, T., Hydrophobic esterification of cellulose nanocrystals for epoxy reinforcement. *Polymer* **2018,** *155*, 64-74.

28. Hui, R.; Qi he, C.; Ming liang, F.; Qiong, X.; Guo qing, H., Preparation and properties of octenyl succinic anhydride modified potato starch. *Food Chemistry* **2009,** *114* (1), 81-86.

29. Hu, Z.; Berry, R. M.; Pelton, R.; Cranston, E. D., One-Pot water-based hydrophobic surface modification of cellulose nanocrystals using plant polyphenols. *ACS Sustainable Chemistry & Engineering* **2017,** *5* (6), 5018-5026.

30. Marefati, A.; Matos, M.; Wiege, B.; Haase, N. U.; Rayner, M., Pickering emulsifiers based on hydrophobically modified small granular starches Part II - Effects of modification on emulsifying capacity. *Carbohydrate Polymers* **2018,** *201*, 416-424.

31. Zerroukhi, A.; Jeanmaire, T.; Raveyre, C.; Ainser, A., Synthesis and characterization of hydrophobically modified starch by ring opening polymerization using imidazole as catalyst. *Starch - Stärke* **2012,** *64* (8), 613-620.

32. Peng, S. X.; Chang, H.; Kumar, S.; Moon, R. J.; Youngblood, J. P., A comparative guide to controlled hydrophobization of cellulose nanocrystals via surface esterification. *Cellulose* **2016,** *23* (3), 1825-1846.

33. Habibi, Y., Key advances in the chemical modification of nanocelluloses. *Chemical Society Reviews* **2014,** *43* (5), 1519-42.

34. Marefati, A.; Wiege, B.; Haase, N. U.; Matos, M.; Rayner, M., Pickering emulsifiers based on hydrophobically modified small granular starches – Part I: Manufacturing and physico-chemical characterization. *Carbohydrate Polymers* **2017,** *175*, 473-483.

35. Xiong, Z.; Ma, S.; Fan, L.; Tang, Z.; Zhang, R.; Na, H.; Zhu, J., Surface hydrophobic modification of starch with bio-based epoxy resins to fabricate high-performance polylactide composite materials. *Composites Science and Technology* **2014,** *94*, 16-22.

36. Xiong, Z.; Yang, Y.; Feng, J.; Zhang, X.; Zhang, C.; Tang, Z.; Zhu, J., Preparation and characterization of poly(lactic acid)/starch composites toughened with epoxidized soybean oil. *Carbohydrate Polymers* **2013,** *92* (1), 810-816.

37. Belhassen, R.; Vilaseca, F.; Mutjé, P.; Boufi, S., Thermoplasticized starch modified by reactive blending with epoxidized soybean oil. *Industrial Crops and Products* **2014,** *53*, 261-267.

38. Tratnik, N.; Kuo, P.-Y.; Tanguy, N. R.; Gnanasekar, P.; Yan, N., Biobased epoxidized atarch wood adhesives: Effect of amylopectin and amylose content on adhesion properties. *ACS Sustainable Chemistry & Engineering* **2020,** *8* (49), 17997-18005.

39. Williams, D. B.; Lawton, M., Aluminium triflate: a remarkable Lewis acid catalyst for the ring opening of epoxides by alcohols. *Organic Biomolecular Chemistry* **2005,** *3* (18), 3269-72.

40. Hansen, T.; Vermeeren, P.; Haim, A.; van Dorp, M. J. H.; Codée, J. D. C.; Bickelhaupt, F. M.; Hamlin, T. A., Regioselectivity of epoxide ring-openings via SN_2 reactions under basic and acidic conditions. *European Journal of Organic Chemistry* **2020,** *2020* (25), 3822-3828.

41. Payard, P. A.; Gu, Q.; Guo, W.; Wang, Q.; Corbet, M.; Michel, C.; Sautet, P.; Grimaud, L.; Wischert, R.; Pera-Titus, M., Direct Amination of Alcohols Catalyzed by Aluminum Triflate: An Experimental and Computational Study. *Chemistry* **2018,** *24* (53), 14146-14153.

42. Gohain, M.; Marais, C.; Bezuidenhoudt, B. C. B., Al(OTf)3: an efficient recyclable catalyst for direct nucleophilic substitution of the hydroxy group of propargylic alcohols with carbon- and heteroatom-centered nucleophiles to construct C–C, C–O, C–N and C–S bonds. *Tetrahedron Letters* **2012,** *53* (9), 1048-1050.

43. Bastola, K., Prasas; Vaidyanathan,Ranji,K; System and method for synthesis of POSS–starch derivatives as effective fillers for developing high performacnce composites. World 2015/143434 Al, 09-24-2015, 2015.

44. Williams, D. B. G.; Cullen, A., Al(OTf)3-mediated epoxide ring-opening reactions: toward piperazine-derived physiologically active products. *The Journal of Organic Chemistry* **2009,** *74* (24), 9509-9512.

45. Wu, J.; Xia, H.-G., Tertiary amines as highly efficient catalysts in the ring-opening reactions of epoxides with amines or thiols in H2O: expeditious approach to β-amino alcohols and β-aminothioethers. *Green Chemistry* **2005,** *7* (10), 708-710.

46. Baidya, M.; Kobayashi, S.; Brotzel, F.; Schmidhammer, U.; Riedle, E.; Mayr, H., DABCO and DMAP--why are they different in organocatalysis? *Angew Chemie International Edition* **2007,** *46* (32), 6176-9.

47. Salmi, T.; Tolvanen, P.; Wärnå, J.; Mäki-Arvela, P.; Murzin, D.; Sorokin, A., Mathematical modeling of starch oxidation by hydrogen peroxide in the presence of an iron catalyst complex. *Chemical Engineering Science* **2016,** *146*, 19-25.

48. Łabanowska, M.; Bidzińska, E.; Pietrzyk, S.; Juszczak, L.; Fortuna, T.; Błoniarczyk, K., Influence of copper catalyst on the mechanism of carbohydrate radicals generation in oxidized potato starch. *Carbohydrate Polymers* **2011,** *85* (4), 775-785.

49. Pietrzyk, S.; Juszczak, L.; Fortuna, T.; Ciemniewska, A., Effect of the oxidation level of corn starch on its acetylation and physicochemical and rheological properties. *Journal of Food Engineering* **2014,** *120*, 50-56.

50. Ferry, J. D., *Viscoelastic Properties of Polymers*. John Wiley & Sons, Inc.: New York, 1980.

51. Ausili, A.; Sánchez, M.; Gómez-Fernández, J., Attenuated total reflectance infrared spectroscopy: A powerful method for the simultaneous study of structure and spatial orientation of lipids and membrane proteins. *Biomedical Spectroscopy and Imaging* **2015,** *4*, 159-70.

52. Menard, K. P., *Dynamic mechanical analysis : a practical introduction*. CRC Press LLC: Florida, 1999

53. Menard, K. P., & Menard, N. (2020), *Dynamic Mechanical Analysis* 3rd edition ed.; CRC press.

54. Sadrykia, F.; Arsalani, N., Preparation and characterization of hydrogel nanocomposites based on oxidized starch and incompletely condensed polyhedral oligomeric silsesquioxanes. *Procedia Materials Science* **2015,** *11*, 531-535.

CHAPTER II

HYDROPHOBIC MODIFICATION OF OXIDIZED STARCH USING AMINOPROPYLISOBUTYL POSS (POSS-NH_2)

Ishan N. Jayalath,[a] Ujith S. K. Madduma-Bandarage,[a] Dilli Dhakal,[b] Bhishma Sedai,[c] Ranji Vaidyanathan,[b] Frank D. Blum[a] *

[a] Department of Chemistry, Oklahoma State University, Stillwater, OK

[b] School of Materials Science and Engineering, Oklahoma State University, Tulsa, OK,

[c] MITO Material Solutions, Inc. Indianapolis, IN

2.1. ABSTRACT

Aminopropyl isobutyl polyhedral oligomeric silsesquioxane (POSS-NH_2) was grafted to oxidized starch (oxystarch–POSS-NH_2) via amide linkages. The product was characterized using ^{1}H NMR, FT-IR, thermogravimetric analysis, X-ray photoelectron spectroscopy, and elemental analysis. After the grafting of POSS-NH_2, oxidized starch showed significantly larger contact angles (increased hydrophobicity) compared to unmodified starch. Furthermore, the oxystarch–POSS-NH_2 showed improved dispersion in various hydrophobic solvents and a commercial epoxy resin.

The thermo-mechanical properties of the neat and filler-loaded resins were studied as a function of different filler loadings. The mechanical results revealed that 15% oxystarch–POSS-NH_2 loaded samples improved the storage and loss modulus by 40% and 46%, respectively. The oxystarch–POSS-NH_2 loaded resin showed improved mechanical properties and can be considered as a potential modified starch-based filler.

2.2. INTRODUCTION

Starch can be a useful biodegradable filler for polymer composites due to its larger natural abundance, biodegradability, renewability, and low cost. Recently, several attempts have been made to enhance the performance of starch and make it a low-cost alternative to more expensive graphene-based additives and fillers.[1-3] The poor dispersion of starch in polymers and resins remains a major barrier that prevents starch from reaching its optimum performance as a filler. The inherent hydrophilicity, inter and intra-molecular hydrogen bonding of starch are the main reasons for weaker interactions between hydrophilic starch nanofillers and hydrophobic polymers. As a result, starch fillers tend to aggregate and agglomerate in the polymer matrix, disrupting the desired outcomes.[3] Therefore, developing a novel starch-based filler with efficient dispersion, improved modulus, and good thermal stability is desirable.

Hydrophobic modification of starch is a promising approach to increase its dispersion in moderately hydrophobic resins such as epoxies.[2-5] Hydrophobic modifications of starch facilitate their dispersion in polymers and can improve the overall mechanical properties of the resin.[1,2,4-8] For example, lauryl chloride has successfully been used as a potential hydrophobic modification of cellulose.[2] The sessile drop water contact angle for this modification was 78° and was significantly larger than that of raw starch[9] which is approximately 35–45°. The modified starch showed an increased reinforcing ability, tensile strength, and flexural modulus of the epoxy resin. In a more environment-friendly approach, plant-based polyphenol was grafted in cellulose nanocrystals (CNC) and resulted in increased hydrophobic characteristics with a sessile drop contact angle of 74° after the reaction.[5] The grafting of octyl succinic acid (OSA) to starch has been studied several times.[1,10] Potato starch was modified by OSA to increase its compatibility with polymers.[6] In another study,[4] the modification of starch was conducted by ring-opening polymerization of e-caprolactone. The resulting starch-grafted polycaprolactone (starch-g-PLC) showed a sessile drop water contact angle of 75°. Although several studies have been targeted to increase the hydrophobicity of starch, polyhedral oligomeric silsesquioxane (POSS), which is a novel class of molecules, has not yet been considered as a potential approach, even though it has shown improved mechanical properties of polymer composites as a reinforcing agent.

Aminopropyl isobutyl POSS (POSS-NH_2) is a hybrid inorganic and organic nanomaterial comprised of a nanoscale silica cage that has seven isobutyl vertex groups attached to Si–O– moieties.[11-13] The isobutyl groups can play an important role when used in polymer composites. These can increase the hydrophobic characteristics of starch by breaking the internal hydrogen bonding and facilitating effective dispersion in resins. Also, once a filler is mixed with resin, the van der Waals attractions between isobutyl groups and resin improve the dispersion which has resulted in improved mechanical properties of the composites, including strength, modulus, and toughness.[14,15] Also, the silica core is a cage that can act as a “heat sink”, which can reduce the thermal conduction in the composites and increase thermal stability. It appears that only a limited number of studies have been done to evaluate the effect of starch–POSS hybrid materials in reinforcing resins.[16] To the best of our knowledge, no study has been done to evaluate the effect of the hydrophobic modification of starch using POSS-NH_2 on the dispersion and mechanical properties of epoxy resins. The grafting of POSS-NH_2 to the starch is believed to provide thermal stability and several other advantages mentioned in the starch.

In this work, we propose a new approach to fabricate oxidized starch through a reaction with POSS-NH_2. First, starch was oxidized using hydrogen peroxide as oxidizing agent and Cu^{2+} as a catalyst. Then the POSS-NH_2 was covalently grafted to starch via the amine groups of POSS-NH_2 and carboxyl acid groups of oxidized starch. The hybrid material was thermally and chemically characterized, and then mechanical analysis was done. A 20% dispersion (masterbatch) of oxystarch–POSS-NH_2 hybrid material was prepared using a commercially available epoxy resin (EPON 862). Finally, the masterbatch was diluted to obtain a series of dispersions, and the synergistic effect of the oxystarch–POSS-NH_2 hybrid material on the mechanical properties of the epoxy resin was evaluated.

2.3. MATERIALS AND METHODS

2.3.1. Materials

EPON 862 (Skygreek Inc, LaGrangeville, NY, USA) was used as a resin system due to its wide applications in industry. The viscosity of the resin was reported as 2500– 4500 cP at 25 °C and the epoxy equivalent weight was 165–173 g/mol. Epicure 3370 (Skygreek Inc, LaGrangeville, NY, USA) was used as the curing agent with viscosity and amine values reported to be 8500–14500 cP, and 384–407 mg/g, respectively. The mixing ratio of EPON 862 to hardener was 100:44 by mass. The corn starch (Hylon® VII), which has an amylose content of up to 70%, was purchased from the National Chemical Starch Company (Westchester, Illinois, USA). POSS-NH_2 was obtained from Hybrid Plastics (Hattiesburg, Mississippi, USA). Analytical grade dimethyl sulfoxide (DMSO), and 99% isopropyl alcohol (IPA) were purchased from Thermo Fisher Scientific (Waltham, Massachusetts, USA). Hydrogen peroxide, 4-dimethyl aminopyridine (DMAP), and 1-ethyl-3-(3-dimethyl aminopropyl)-carbodiimide (EDC) were purchased from Spectrum Chemicals. These materials were used directly without further purification, modification, or other treatments.

2.3.2. The oxidation of corn starch

The oxidation of the corn starch was carried out according to the procedure described by Zhang et al.[17] Briefly, starch (2 g) was gelatinized in 15 ml of deionized (DI) water in a 100 mL round bottom flask at 85 ℃ for 1 h with moderate stirring in an oil bath. The temperature of the oil bath was reduced to 55 ℃ after the gelatinization of starch. Then, 10 mg of $CuSO_4 \cdot 5H_2O$ was dissolved in 4 mL of DI water and added to the starch slurry with continued stirring for another 0.5 h. A portion (10 mL) of hydrogen peroxide solution (30 w/w %) was added and oxidation continued for another 1 h. The dispersion was allowed to cool to room temperature and precipitated using a 1:5 ratio of the reaction mixture to the ethanol. The product was filtered using Whatman #2 filter paper and washed 5 times with isopropyl alcohol. Finally, the product was dried at 60 °C for 24 h before chemical characterization and dispersion in epoxy resin.

2.3.3. Synthesis of oxystarch–POSS-NH_2 filler

In a 50 mL round-bottom flask, 1 g of dried oxidized starch was dispersed in 20 mL of THF and stirred for 15 min at 60 °C. Next, 2.2 g of POSS-NH_2 was dissolved in 10 mL of THF and added to the reaction mixture. Finally, EDC and DMAP were dissolved in THF and added to the reaction mixture. The reaction was carried out for 24 h. The final product was filtered and washed with 100 mL of acetone. The crude product was purified by Soxhlet extraction for 24 h with tetrahydrofuran (THF) and dried in a vacuum oven at 60 °C for 48 h before the characterization.

2.3.4. Characterization

The NMR spectra were recorded on an Avance 400 MHz spectrometer (Bruker, Ettlingen, Germany). The spectra were recorded at room temperature with DMSO-d_6 solvent.

The thermal stability of the composites was determined using a Model Q50 Thermogravimetric Analyzer (TA Instruments, New Castle, DE, USA). The experiments were conducted in air, using 10 mg of sample and a ramp rate of 20 °C/min.

Attenuated total reflection (ATR)-Fourier transformed infrared (FTIR) spectra were recorded using a Thermo Nicolet i550 spectrometer (Thermo Scientific, Waltham, Massachusetts, USA) equipped with an ATR diamond crystal. The spectra were collected from 500–4500 cm^{-1}, with a spectral resolution of 4 cm^{-1}, 64 scans, and automatic atmospheric suppression.

The X-ray diffraction (XRD) spectra of starch before and after the grafting reaction were collected between $2\theta = 7°$ to $60°$ using a D8 Advance X-ray diffractometer (Bruker, Berlin, Germany) with Cu-Kα radiation at a voltage of 40 kV and current of 40 mA.

The change in the silicon (Si) content of the starch was estimated before and after grafting POSS-NH_2. The calculation assumes that the silicon in the composite is from the POSS-NH_2. The composition of oxystarch–POSS-NH_2 was determined using a Philips PW 1410 X-ray fluorescence (XRF) spectrometer. The calculation is based on the stoichiometry of silicon to POSS-NH_2 is 1:8. The degree of substitution of POSS-NH_2 to the starch can be defined as the mole ratio of POSS-NH_2 to glucose units in the material. The silicon content was used to calculate the number of moles of POSS-NH_2 in the product and degree of substitution (DS) according to the equation used by Kavaliauskaite et al.[18] with a slight modification;

$$\mathrm{DS} = \frac{\mathrm{m_{Si}} \times 162}{22400\text{-}(\mathrm{m_{Si}} \times 874.5)} \qquad (2.1)$$

where Si is the mass of silicon estimated from the XRF analysis. The values 162 and 874.5 are the molecular masses of the glucose unit and the POSS-NH_2, respectively. The assumptions and the derivation of the equation are shown in the Supporting Information.

The oxystarch–POSS-NH_2 was compressed into a pellet, and the water contact angle was measured at ambient temperature using a custom-made contact angle apparatus.[1,19] Briefly, 300 mg of modified starch was compressed into roughly 13 mm diameter pellets using a hydraulic press (Specac, UK) with a force of 67,000 N (15000 lbf) for 10 min. The pellet was dried at 90 °C for 1 h before the measurement. The contact angle instrument had a movable stage; a pellet was placed on the stage, a droplet of distilled water was placed on the pellet, and photographs were taken every minute starting at 1 min until 10 min.

Oxystarch–POSS-NH_2 was master-batched into epoxy resin using a three-roll calendaring mill. The dispersions of 0.1, 0.5, 1, 2, 5, 10, and 15% were obtained by diluting appropriate amounts of the master batch with neat epoxy resin using a speed mixer. Each dispersion was mixed well with a hardener (based on the supplier's recommended amount), degassed using a speed mixer followed by placing under a vacuum chamber, poured into block molds, and cured completely to obtain a resin block of constant thickness. The DMA specimens were tested using a Model Q800 (TA Instruments, New Castle, DE, USA) dynamic mechanical analyzer. The storage modulus, loss modulus, and tan δ of the specimens were obtained between 30 °C and 140 °C in the double cantilever mode using a fixed frequency of 1 Hz and a ramp rate of 5 °C/min. A picture of a dynamic mechanical analyzer loaded with an additive-filled epoxy sample is shown in the Supplementary Information.

2.4. RESULTS AND DISCUSSION

2.4.1. Oxidation of starch

The oxidation of starch was carried out using hydrogen peroxide to convert some of the hydroxyl groups into carboxylic acids and aldehydes. The oxidation was catalyzed using $CuSO_4$ as a catalyst to increase the degree of oxidation.[17] The degree of oxidation was estimated by the acid-base titrimetric method as described in Zhang et al.[17] and calculated as 21% mol oxidized/mol of glucose. The expected chemical changes that occur during the starch oxidation are shown in Figure 2.1.

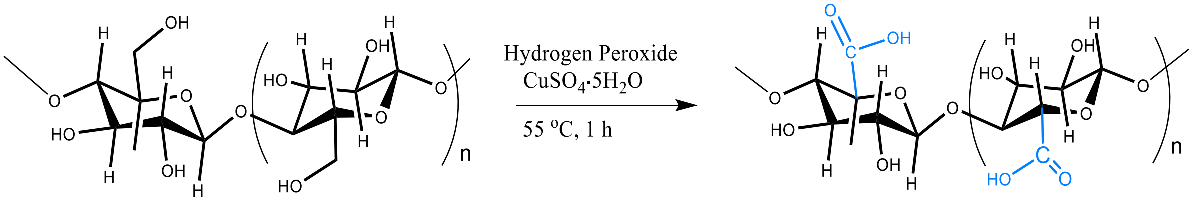

Figure 2.1. Oxidation of corn starch.

The chemical and thermal characterization of the oxidized starch was carried out using FTIR spectroscopy and TGA analysis. The characteristic absorption bands of starch were found at 997, 2931, and 3300 cm^{-1}. The major peaks can be assigned as follows: the absorption band at 997 cm^{-1} is characteristic of the glucose ring (C–O–C) in the structure of starch. The peak appearing at 2931 cm^{-1} is due to the C–H stretching vibration in starch. The peak at 1639 cm^{-1} is from the residual water present even after thorough drying.[20]

In the FTIR spectrum of oxidized starch, the peak at 1730 cm^{-1} was due to the newly formed carboxylic acid groups. The temperature and reaction time are the major factors that increase the degree of oxidation, and consequently, the absorption amount of carbonyl stretching.[17] Presence of the carbonyl stretching vibrations in the oxidized starch spectrum confirms the partial oxidation. Since the hydroxyl groups of the starch absorb water, there is a small peak at 1636 cm^{-1} for the H_2O bending vibrations. The FTIR spectra and TGA thermograms of starch and oxidized starch are shown in Figures 2.2A and 2.2B.

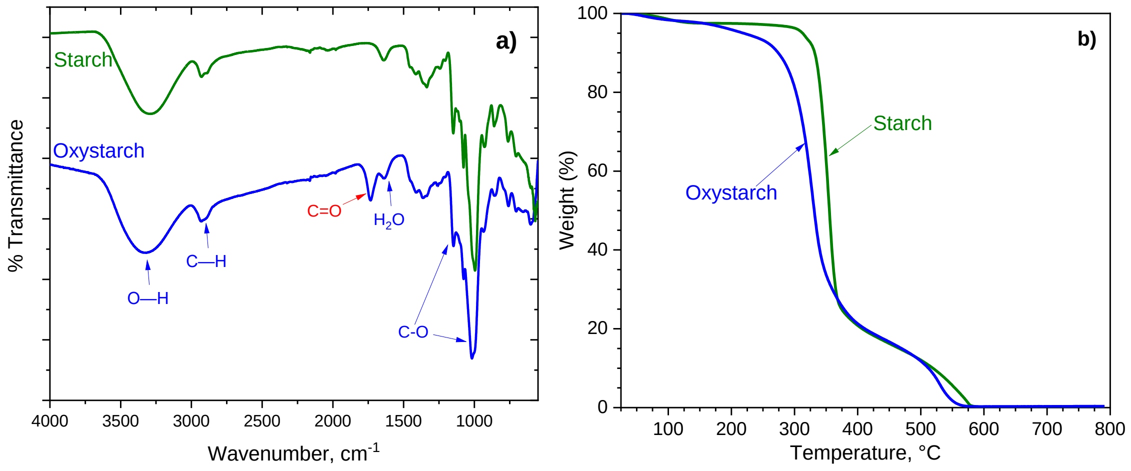

Figure 2.2. The a) FTIR spectra and b) thermogravimetric analysis of starch and oxidized starch.

The thermograms of the starch can be considered in 3 steps, based on the mass losses. (1) The mass loss of the starch that takes place up to 150 °C can be attributed to the removal of absorbed moisture in the starch.[19] (2) The mass loss from 150–380 °C can be assigned to the degradation of amylose molecules in the starch.[21,22] (3) The branched, long-chain amylopectin molecules degrade above 360 °C. These long-chain molecules are crystalline and show larger activation energy compared to amylose regions. These are thermally stable and degrade at elevated temperatures.[21-23] The thermogravimetric analysis of oxidized starch shows a slight decrease in thermal stability due to oxidation compared to the starting material. Interestingly, the thermal stability reduced in the temperature range corresponds to amylose.[23] In addition, the increasing carbonyl content may weaken the inter-and intra-molecular hydrogen bonds of starch that contribute to thermal stability.[24] Moreover, in starch, the thermal degradation below 300 °C is due to the thermal condensation between hydroxyl groups that releases water molecules.[25] The conversion of hydroxyl groups to carbonyl groups affects condensation as well. Additionally, the depolymerization of molecular chains, due to oxidation, leads to a molecular weight decrease, It may also affect the thermal stability of oxidized starch.[17,26]

2.4.2 Synthesis and characterization of oxystarch-POSS-NH_2.

POSS–NH_2 was grafted to oxidized starch via an amide bond that formed between the amine group of POSS and the carboxylic acid group of oxidized starch. Hence, POSS-NH_2 molecules grafted only to the oxidized sites of the starch molecules. Since the oxidation of starch with hydrogen peroxide produces both carbonyl and carboxyl groups, the degree of substitution depends on the number of carboxyl groups present in the oxidized starch. The small degree of oxidation caused a small degree of substitution of POSS-NH_2 onto oxidized starch. High amylose corn starch (amylose content of up to 70%) was selected for this study as it has previously shown good performance in polymer composites.[27] Also the high amylose corn starch is easy to disperse in solvents as well as proven to have large grafted amounts during the amidation reaction.[27] A schematic representation of POSS-NH_2 grafted on oxidized starch is shown in Figure 2.3.

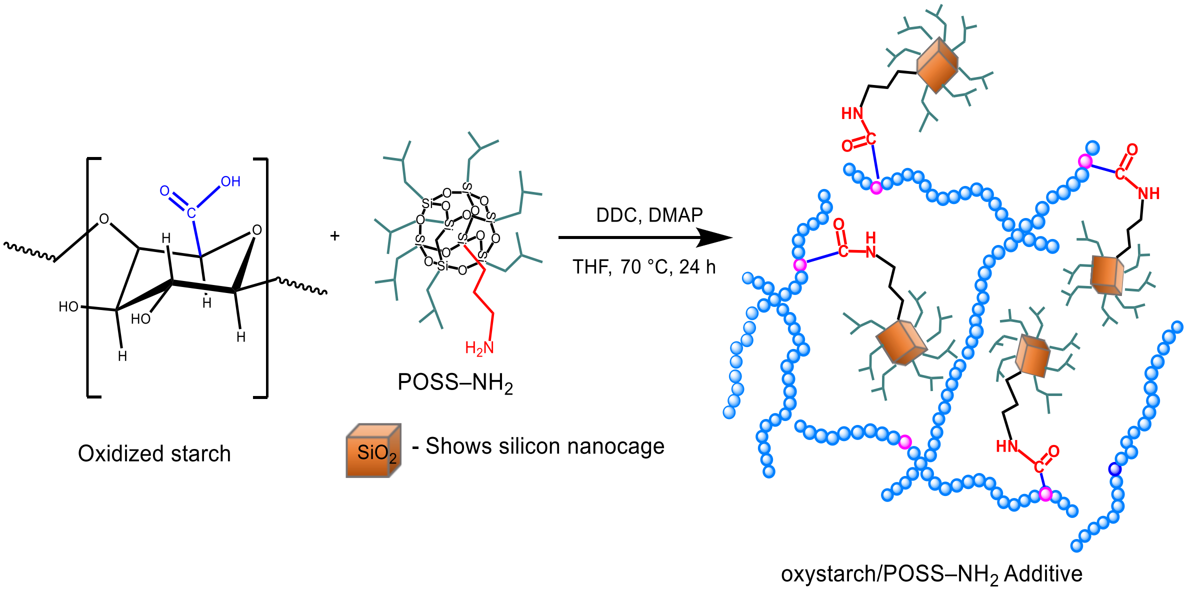

Figure 2.3. The reaction of oxidized starch with POSS-NH_2.

2.4.3. FTIR spectroscopy

The FTIR spectra of oxidized starch, POSS-NH_2, and oxystarch–POSS-NH_2 are shown in Figure 2.4 for the IR region of interest. In the POSS-NH_2 spectrum, the peaks at 1085 and 2869 cm^{-1} can be assigned to the Si–O–Si of the POSS cage and C–H in the organic vertex groups.[28-30] The C–N stretch of the POSS-NH_2 was found at 1228 cm^{-1}.[28,29] The full spectra are shown in the Supporting Information.

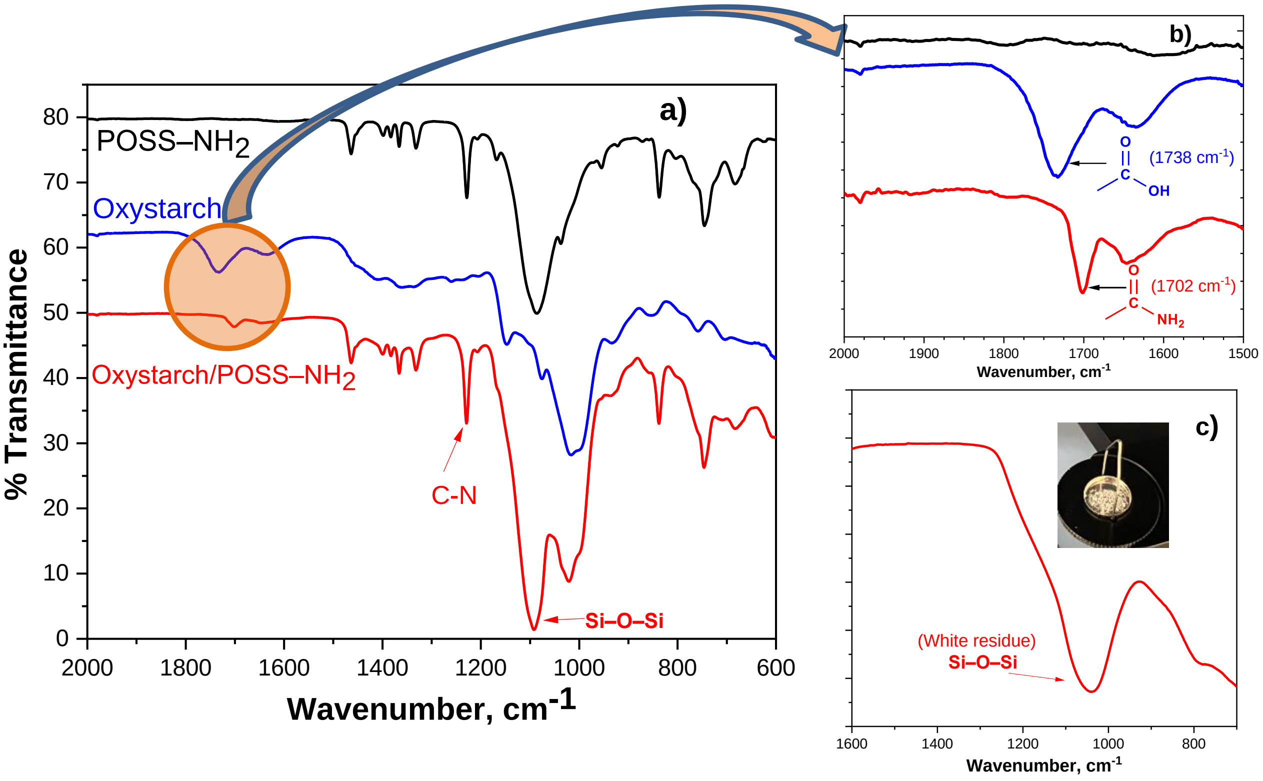

Figure 2.4. a) FTIR spectra of POSS-NH_2 (top, black), oxidized starch (middle, blue), and oxystarch–POSS-NH_2 (bottom. red), b) the expanded regions of 2000 – 1500 cm^{-1}, and c) is the FTIR spectra for the white residue shown in the picture that remained after the TGA analysis to 900 °C of the oxystarch-POSS-NH_2.

In the FTIR spectra of oxystarch–POSS-NH_2 (Figure 2.4a), the presence of C–N stretching vibrations at 1228 cm^{-1} and the new carbonyl stretching vibrations due to amide bonds at 1702 cm^{-1} confirm the successful incorporation of POSS-NH_2 into oxidized starch. The obvious change before and after the grafting is the newly formed amide bond. The decrease of carbonyl frequency from 1738 to 1702 cm^{-1} is consistent with the formation of an amide bond (Figure 2.4b). The presence of silica in oxystarch–POSS-NH_2 was confirmed by taking the FTIR spectrum of the white residue that remained after the thermogravimetry analysis (TGA) is shown in Figure 2.4c. The intense peak at 1162 cm^{-1} can be assigned to the Si–O–Si stretching from silica in the white TGA residue.

2.4.4. ^{1}H NMR spectroscopy

The oxystarch–POSS-NH_2 hybrid material was characterized using ^{1}H NMR spectroscopy, as shown in Figure 2.5. The NMR spectrum of starch and POSS-NH_2 was also taken and is shown to compare with the starch before and after the grafting of POSS-NH_2. The ^{1}H NMR spectrum of oxystarch and oxystarch–POSS-NH_2 was measured in DMSO-d_6; the peak at 2.5 ppm was assigned to the hydrogen atoms of DMSO-d_6 and used as the reference. The spectrum of POSS-NH_2 was recorded in $CDCl_3$.

In the POSS-NH_2 spectrum,[31] the proton attached to most shielded carbon atoms **(c)** and **(d)**, which are next to the silicon cage, can be assigned to the peaks at 0.6 ppm.[32] The signals were split into double doublets that were unexpected observations. The intense peak at 0.9 ppm can be assigned to the protons of carbon **(a)**. The protons in carbon (**e)** can be assigned to the peak at 1.6 ppm that appeared as a pentet due to the splitting from the protons in the (**d)** and (**f)** carbon atoms. The protons attached to the carbon atoms labeled (**b)** can be assigned to the peaks at 1.9 ppm that appeared as a nonet. The most de-shielded protons are those attached to the carbon atom next to the electronegative amine group. Therefore, the peak at 2.7 ppm can be assigned to the protons labelled as carbon atom **(f)**.

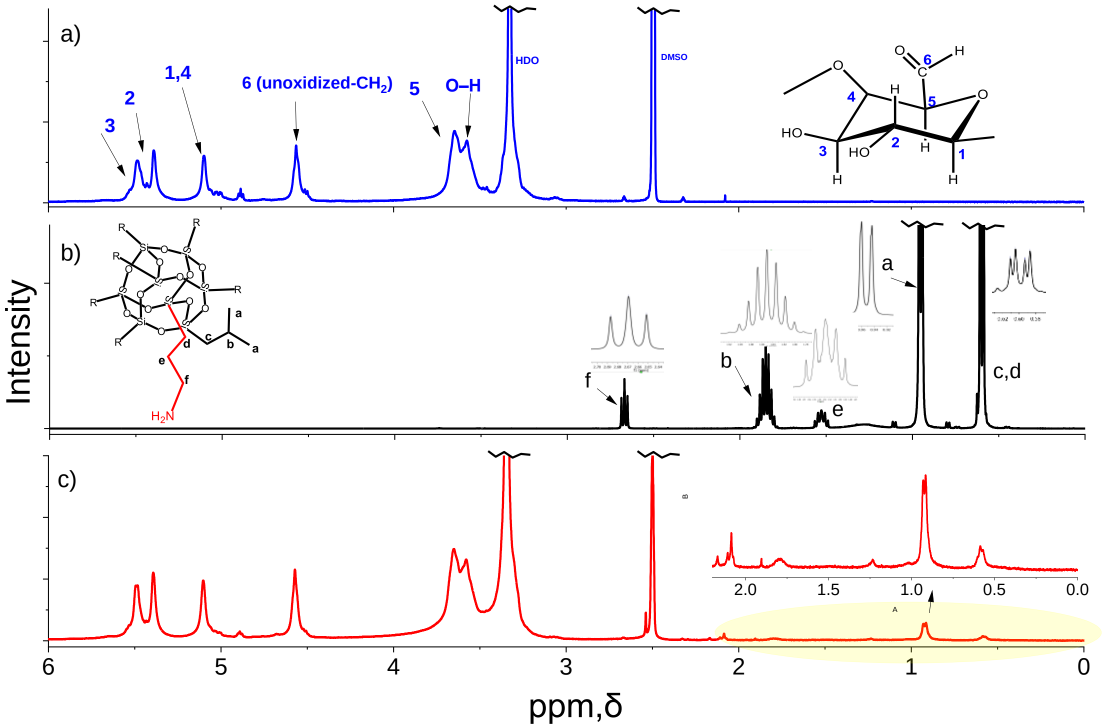

Figure 2.5. The ^{1}H NMR spectra of the a) oxidized starch b) POSS-NH$_2$, and c) oxystarch–POSS-NH$_2$. The multiplicity of POSS-NH$_2$ is shown in the inset close to each peak.

After the amidation of POSS-NH$_2$ with oxidized starch, the proton resonances of the spectrum of the oxystarch–POSS-NH$_2$ showed several differences from the native starch spectrum. The appearance of new peaks at 0.9 and 0.6 ppm in the oxystarch–POSS-NH$_2$ spectrum can be attributed to the protons derived from the POSS-NH$_2$.

2.4.5. Thermogravimetric analysis (TGA)

The thermal stability of oxystarch–POSS-NH$_2$ hybrid material was evaluated with TGA. As shown in Figure 2.6, both corn starch and the oxystarch–POSS-NH$_2$ hybrid material began to lose weight upon heating in air below 100 °C, and this weight loss was due to the evaporation of physically adsorbed water. In the POSS-NH$_2$ thermogram, no weight loss was shown below 100 °C. This is due to the hydrophobic nature of the molecule that results in no absorbed water.

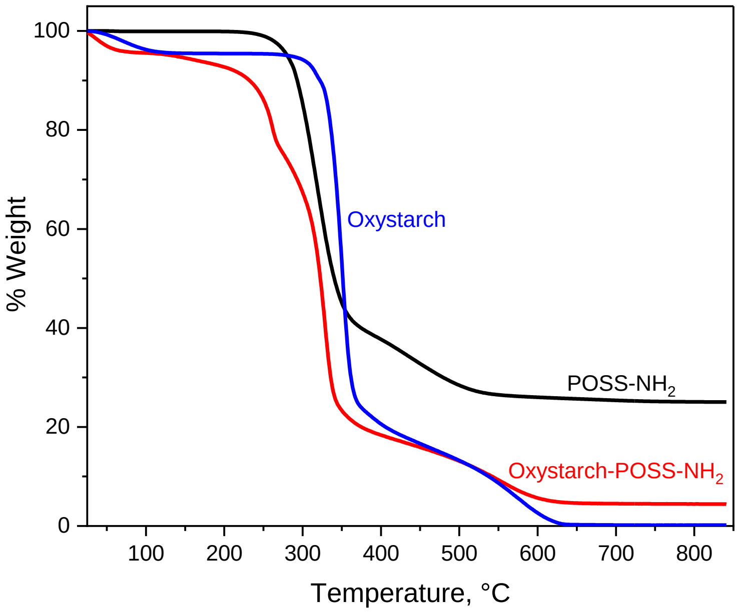

Figure 2.6. Thermograms of oxidized starch, POSS–NH$_2$, and oxystarch–POSS-NH$_2$

In the POSS-NH$_2$ thermogram, approximately 75% of the mass loss up to 600 °C corresponds to the thermal decomposition of organic vertex groups, and 25% of residue beyond 550 °C represents the silicon cage. the mass loss at 600 °C is for the complete degradation of starch and organic vertex groups of POSS-NH$_2$. Since the residue of the starch thermogram is zero, the residue of the oxystarch–POSS-NH$_2$ is likely due to the remnants of the silica cage. Based on the thermogram of oxystarch–POSS-NH$_2$ the mass fraction of silica can be estimated from the TGA as ~4.7% as the final residue is SiO_2. Based on the silica residue, the ratio of SiO_2: POSS-NH$_2$ is equal to 1:3. For the starch–POSS-NH$_2$, Therefore, the mass percentage of POSS-NH$_2$ in the filler can be estimated as approximately 14.1%. This amount is comparable and in good agreement with the results obtained for the amount of silicon content in elemental analysis.

2.4.6. Elemental analysis

Elemental analysis of oxystarch–POSS-NH$_2$ was carried out using XRF spectroscopy, and the results are shown in Table 2.1. The degree of substitution was calculated using the amount of silicon in the product. Based on the silicon percentage of the XRF study, the degree of substitution of POSS-NH_2 in the starch was calculated as 0.02. The number denotes the mole ratio of the grafted molecule to starch in the final product.[2,4,6] The details of the calculation are shown in Supporting Information.

Table 2.1. The XRF results of oxystarch–POSS-NH_2

Atom	Mass (%)
C	45.2
O	39.8
N	9.0
Si	2.7
Na	0.7
Other	~2.5

2.4.7. Dispersion of modified starch in solvents

The dispersion of the oxystarch–POSS-NH_2 was compared with that of oxidized starch. The solvents used for the study were toluene (most hydrophobic), tetrahydrofuran, acetone, 2-propanol, ethanol, and water (most hydrophilic). The photographs were taken following 5 min of ultrasonication of the material in each solvent as shown in Figure 2.7. When compared to oxidized starch, dispersion of the oxystarch–POSS-NH_2 and POSS-NH_2 is better in toluene, which confirms the hydrophobic nature of the oxystarch–POSS-NH_2. The hydrophobic nature of the oxystarch–POSS-NH_2 is further confirmed by the large contact angle that is shown in Figure 2.7d. The time dependence of the contact angle measurements shows that exposure of the modified surface to the water makes the surface more hydrophilic with time.

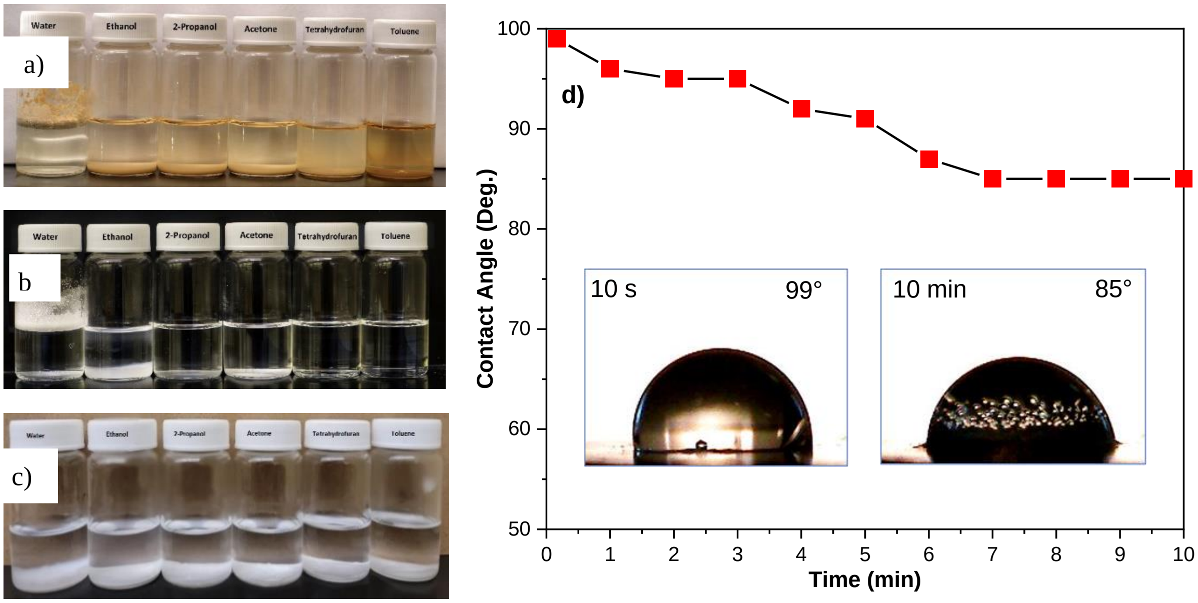

Figure 2.7. Dispersion of a) oxystarch–POSS-NH_2, b) POSS-NH_2, c) oxystarch in different solvents, and d) contact angle of starch–POSS-NH_2 hybrid material, where the two insets show the shape of the water droplet at 10 s (left) and 10 min (right).

The water contact angle on the oxystarch–POSS-NH_2 was measured using the compressed pellet method to confirm the hydrophobic nature of the filler. The compressed pellet method provides accurate data when the water droplets are static on the surface. Measurements were run in triplicate to verify the reproducibility of the estimation. There are several reports on the hydrophobic modification of biomacromolecules using lauryl chloride,[2] plant-based polyphenols,[5] and octyl succinic acid (OSA)[1,10] that have shown 78°, 74°, and 75°, respectively. In this work, the initial contact angle of the water droplet on the oxystarch–POSS–NH_2 was recorded as about 99°, a relatively larger value than reported in previous studies.[2,3,5] However, the contact angle decreased over time probably because the oxystarch–POSS-NH_2 quickly absorbs water and swells when in contact with water.

2.4.8. X-ray diffraction (XRD) analysis

The effect of the oxidation and grafting reaction on the microstructure of starch was studied by XRD analysis. The XRD spectra for the starch, oxystarch, POSS-NH_2, and oxystarch–POSS-NH_2 are shown in Figure 2.8.

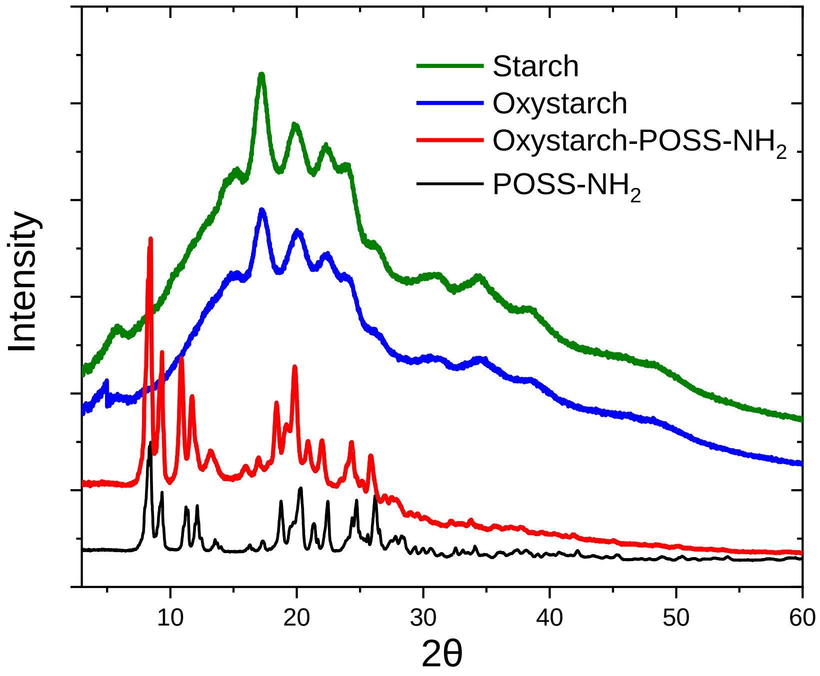

Figure 2.8. The X-ray diffraction patterns of starch, oxystarch, POSS-NH_2, and the oxystarch–POSS-NH_2 hybrid material.

The XRD spectrum of corn starch shows three main peaks superimposed on a broad range at different diffraction angles (2θ), 15°, 17°, and 22°.[33-36] There are other broad peaks as well at larger angles. The oxidized starch shows a similar XRD spectrum to starch that is comparable with the XRD spectra reported by Zhang et al.[17] In the XRD spectrum of oxidized starch, it was observed that the peak intensities were smaller compared to raw starch. This may be due to a slight disturbance to the crystallinity of the starch during the oxidation reaction. This claim can be supported by the specific density difference between the two materials. The specific density of the oxidized starch was smaller compared to raw starch.[34] After the modification reaction, the XRD spectrum of oxystarch-POSS-NH_2 shows highly intense peaks due to the presence of the POSS-NH_2 since the POSS-NH_2 was highly crystalline. After the reaction with oxidized starch, starch–POSS-NH_2 showed peaks corresponding to the POSS-NH_2 crystalline patterns that confirmed the presence of POSS-NH_2 in the product. The presence of the starch was indicated by the broad patterns underneath the intense/sharp POSS-NH_2 peaks.

2.4.9. Thermal stability of epoxy/oxystarch–POSS-NH_2

The derivative thermogravimetric analysis (DTGA) analysis of the filler-loaded epoxy resin was carried out to study the effect of fillers on the thermal stability of the resin. The thermograms in Figure 2.9 show a decrease in the derivative weight as the filler loading percentage increases. This is due to the larger amount of modified starch in the filler–loaded epoxy material. However, there was no significant shift in the curves, which suggests the minimal effect of filler loading on the thermal stability of epoxy resin.

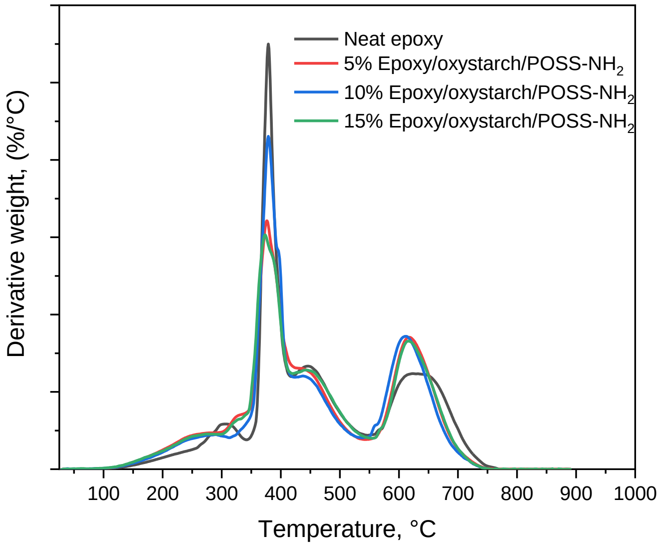

Figure 2.9. Derivative TGA thermograms of various loadings of filler-loaded epoxy resin.

2.4.10. Dynamic mechanical analysis (DMA)

DMA analysis was conducted on modified starch–loaded epoxy to evaluate the effect of fillers on the viscoelastic properties of the epoxies at a fixed frequency of 1 Hz, using flexural mode with temperature scans from room temperature to 130 °C. The DMA data provided much information that was useful in analyzing the viscoelastic properties of the resin and the results are shown in Figure 2.10. The storage modulus (G′) evaluates the material's elastic behavior (energy storage ability), and those curves are shown in Figure 2.10a.

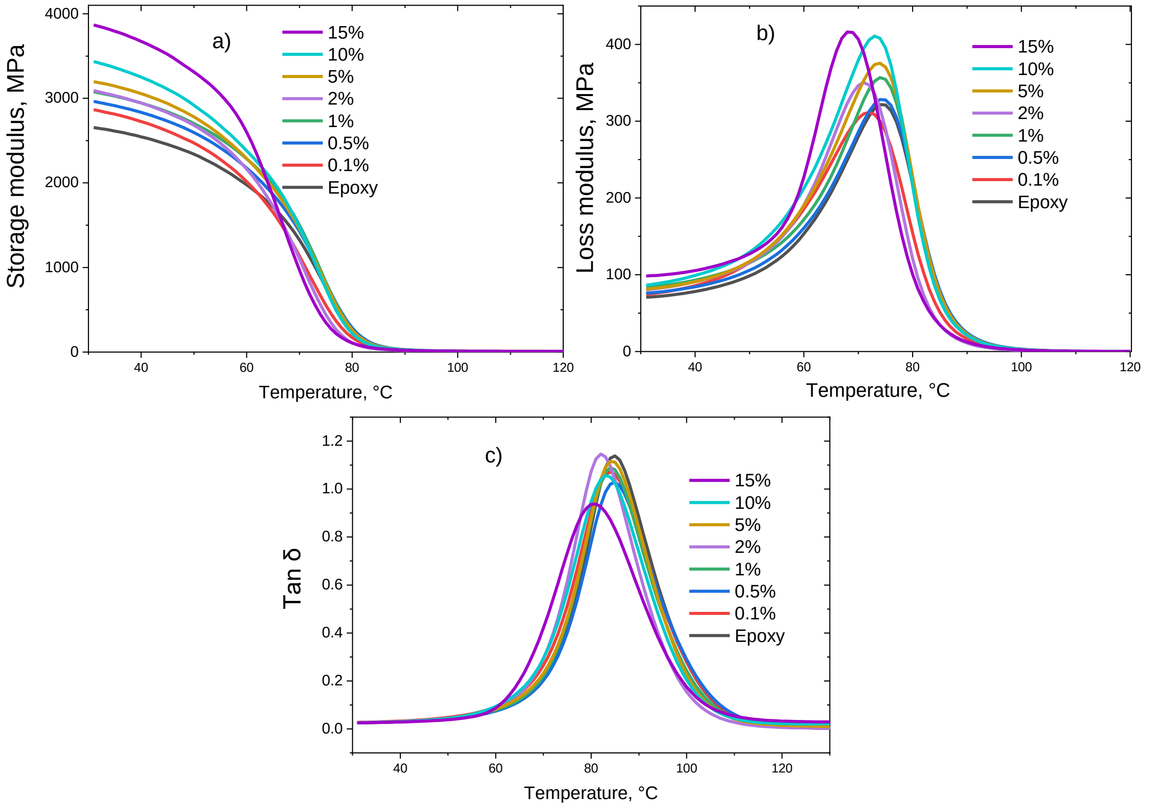

Fig. 2.10. The variation of a) storage modulus (G′), b) loss modulus (G″) c) tan δ of the neat epoxy and epoxy/oxystarch–POSS-NH_2 with 0.1, 0.5, 1, 2, 5, 10, and 15% filler-loaded samples at 1 Hz frequency.

The G′ vs temperature curve can be divided into three regions. They are glassy, glass transition, and rubbery regions of the polymer. The highest G′ of the material is shown at room temperature, and G′ decreases with increasing temperature as the freedom for molecular motion increases. In the glass transition region, G′ decreases drastically due to the change of material from a glassy to a rubbery state. In other words, the elastic properties of the material are reduced, and the resin starts to behave as a rubbery material.

The filler-loaded samples also behaved similarly to the neat epoxy while showing larger G′ values than the neat epoxy. Also, the G′ values increased as the percentage of the modified starch increased, and the 15% filler-loaded sample showed a 45.6% increase in G′. The loss modulus (G") provides information on the material's viscous behavior and ability to lose or dissipate energy.[37] The intensity of the G" transition of the modified starch-loaded epoxy composites (Figure 2.10a) increased with increasing filler loading compared to the neat epoxy resin. The increase of G" may be due to the increase of stiffness as the filler loading increases in the resin. The G" was increased in 0.1, 0.5, 1, 2, 5, 10, and 15% filler-loaded samples by 8, 13, 14, 17, 17, 13, and 40%, respectively. This is a good improvement of modulus compared to neat resin. There was little change in the maximum temperature of G″ with filler content.

The ratio of elastic to the viscous response of the material can be studied using tan δ (Figure 2.10c) curves. These values give information on the energy dissipation mechanism, which is simply the ratio between loss modulus and storage modulus. The neat epoxy sample shows the tallest tan δ peak, representing the most efficient energy dissipation although the area under the curves is fairly constant. In filler-loaded samples, the peak heights are smaller than those in the neat resin, which suggests the restrictions to the segmental movements of the neat epoxy that ultimately result in the low energy dissipation capacity of the material. This observation is consistent with the glass transition temperature (T_g) of the composites. In contrast to the other samples, the 15% filler-loaded sample showed a marked lower maximum tan õ indicative of a slightly lower T_g and broader response than the neat epoxy.

The summary of the DMA findings can be found in Table 2.2. The table tabulated the G′ and G″ at 30 °C and the temperature at maximum tan δ. As seen in the maximum of tan δ curves, the T_g of the modified starch–loaded epoxy remained the same until 5% loading and decreased slightly after that.

Table 2.2. The summary of DMA results for storage modulus, loss modulus, and tan δ.

Sample Name. wt%	Storage modulus, at 30 °C, (G′) (MPa)	Loss modulus, at 30 °C, (G″) (MPa)	Temperature at maximum tan δ (T_g) (°C)
Neat epoxy	2655 ± 41	70 ± 3	85 ± 2
0.1	2866 ± 50	76 ± 5	83 ± 3
0.5	2963 ± 37	79 ± 5	85 ± 2
1	3072 ± 43	80 ± 4	84 ± 3
2	3092 ± 48	82 ± 3	83± 3
5	3185 ± 51	82 ± 2	82± 1
10	3436 ± 43	86 ± 3	81 ± 2
15	3867 ± 55	98 ± 4	79 ± 3

The significant decrease of the T_g after the 5% loading may be due to the reduction of the interaction between modified starch and epoxy resin. The neat epoxy shows the largest T_g compared to filler-loaded samples. In larger filler loadings such as 15%, the epoxy resin's T_g may be affected due to the higher mobility of amylose molecules in the starch. On the other hand, the oxystarch–POSS-NH_2 filler may have restricted the reaction between the curing agent and epoxy resin, which ultimately caused a reduction in the crosslinking density of the resin. Reduced crosslinking density may also be a reason for the observation of lower T_g in larger filler-loaded samples compared to smaller filler-loaded samples. It can be concluded that the filler has increased the epoxy resin's storage and loss modulus with a minimum effect on the tan δ.

2.5. CONCLUSIONS:

In this paper, we reported the successful grafting of POSS-NH_2 into oxidized corn starch to develop a filler for epoxy resins. The covalent bond between POSS-NH_2 and oxidized starch was confirmed by FTIR and ^{1}H NMR spectroscopy. The evidence for the presence of POSS-NH_2 in starch was identified using contact angle measurement and reported as 99°, which is a significantly larger contact angle in similar studies. The water droplets were stable on the surface of the filler for 10 min suggesting the material maintains its hydrophobic characteristics when exposed to moisture although it does absorb some water. Finally, the oxystarch–POSS-NH_2 was dispersed in commercial epoxy resin and tested for thermal stability and modulus using TGA and DMA. The filler did not impart a significant effect on the thermal stability of epoxy resin until higher filler loading of 15%. The DMA analysis showed larger storage and loss modulus as increased filler loading compared to the neat epoxy. The G' and G" of the 15% filler-loaded samples had shown 46% and 40% increases compared to the neat sample. This is a good improvement of modulus compared to neat resin. With all these aspects, we believe, the novel approach to modifying starch using POSS-NH_2 may expand the future usage of starch in filler manufacturing for hydrophobic resins.

2.6. ACKNOWLEDGEMENTS

The authors acknowledge the financial support and testing facility provided by MITO Material Solutions, under the grant of the Center for Advancement of Science & Technology (OCAST) (Award No. AR19-011-2 and Sub award No 7003-AR11-02). The authors also acknowledge the partial funding provided by Oklahoma State University under Robberson Summer Dissertation Fellowship, Research and Creativity Activities Grant. The authors acknowledge the Yolanda Vasquez research group at the Department of Chemistry, at Oklahoma State University for recording XRD spectra for the study.

2.7 REFERENCES:

1. Marefati, A.; Matos, M.; Wiege, B.; Haase, N. U.; Rayner, M., Pickering emulsifiers based on hydrophobically modified small granular starches Part II - Effects of modification on emulsifying capacity. *Carbohydrate Polymers* **2018,** *201,* 416-424.

2. Trinh, B. M.; Mekonnen, T., Hydrophobic esterification of cellulose nanocrystals for epoxy reinforcement. *Polymer* **2018,** *155,* 64-74.

3. Xiong, Z.; Ma, S.; Fan, L.; Tang, Z.; Zhang, R.; Na, H.; Zhu, J., Surface hydrophobic modification of starch with bio-based epoxy resins to fabricate high-performance polylactide composite materials. *Composites Science and Technology* **2014,** *94,* 16-22.

4. Zerroukhi, A.; Jeanmaire, T.; Raveyre, C.; Ainser, A., Synthesis and characterization of hydrophobically modified starch by ring opening polymerization using imidazole as catalyst. *Starch - Stärke* **2012,** *64* (8), 613-620.

5. Hu, Z.; Berry, R. M.; Pelton, R.; Cranston, E. D., One-Pot water-based hydrophobic surface modification of cellulose nanocrystals using plant polyphenols. *ACS Sustainable Chemistry & Engineering* **2017,** *5* (6), 5018-5026.

6. Hui, R.; Qi he, C.; Ming liang, F.; Qiong, X.; Guo qing, H., Preparation and properties of octenyl succinic anhydride modified potato starch. *Food Chemistry* **2009,** *114* (1), 81-86.

7. Peng, S. X.; Chang, H.; Kumar, S.; Moon, R. J.; Youngblood, J. P., A comparative guide to controlled hydrophobization of cellulose nanocrystals via surface esterification. *Cellulose* **2016,** *23* (3), 1825-1846.

8. Habibi, Y., Key advances in the chemical modification of nanocelluloses. *Chemical Society Reviews* **2014,** *43* (5), 1519-42.

9. Ojogbo, E.; Blanchard, R.; Mekonnen, T., Hydrophobic and Melt Processable Starch-Laurate Esters: Synthesis, Structure–Property Correlations. *Journal of Polymer Science Part A: Polymer Chemistry* **2018,** *56* (23), 2611-2622.

10. Marefati, A.; Wiege, B.; Haase, N. U.; Matos, M.; Rayner, M., Pickering emulsifiers based on hydrophobically modified small granular starches – Part I: Manufacturing and physico-chemical characterization. *Carbohydrate Polymers* **2017,** *175*, 473-483.

11. Ghani, K.; Kiomarsipour, N.; Ranjbar, M., New high-efficiency protective coating containing glycidyl-POSS nanocage for improvement of solar cell electrical parameters. *Journal of Nanostructures* **2019,** *9* (1), 103-111.

12. Rahman, M. M.; Filiz, V.; Khan, M. M.; Gacal, B. N.; Abetz, V., Functionalization of POSS nanoparticles and fabrication of block copolymer nanocomposite membranes for CO_2 separation. *Reactive and Functional Polymers* **2015,** *86*, 125-133.

13. Arslan, I.; Tasdelen, M. A., POSS-based hybrid thermosets via photoinduced copper-catalyzed azide–alkyne cycloaddition click chemistry. *Designed Monomers and Polymers* **2016,** *19* (2), 155-160.

14. Jiang, D.; Xing, L.; Liu, L.; Yan, X.; Guo, J.; Zhang, X.; Zhang, Q.; Wu, Z.; Zhao, F.; Huang, Y.; Wei, S.; Guo, Z., Interfacially reinforced unsaturated polyester composites by chemically grafting different functional POSS onto carbon fibers. *Journal of Materials Chemistry A* **2014,** *2* (43), 18293-18303.

15. Zhang, R. L.; Gao, B.; Du, W. T.; Zhang, J.; Cui, H. Z.; Liu, L.; Ma, Q. H.; Wang, C. G.; Li, F. H., Enhanced mechanical properties of multiscale carbon fiber/epoxy composites by fiber surface treatment with graphene oxide/polyhedral oligomeric silsesquioxane. *Composites Part A: Applied Science and Manufacturing* **2016,** *84*, 455-463.

16. Bastola, K., Prasas; Vaidyanathan,Ranji,K; System and method for synthesis of POSS–starch derivatives as effective fillers for developing high performacnce composites. World 2015/143434 Al, 09-24-2015, 2015.

17. Zhang, Y. R.; Wang, X. L.; Zhao, G. M.; Wang, Y. Z., Preparation and properties of oxidized starch with high degree of oxidation. *Carbohydrate Polymers* **2012,** *87* (4), 2554-2562.

18. Kavaliauskaite, R.; Klimaviciute, R.; Zemaitaitis, A., Factors influencing production of cationic starches. *Carbohydrate Polymers* **2008,** *73* (4), 665-75.

19. Sedai, B. R.; Khatiwada, B. K.; Mortazavian, H.; Blum, F. D., Development of superhydrophobicity in fluorosilane-treated diatomaceous earth polymer coatings. *Applied Surface Science* **2016,** *386*, 178-186.

20. Luo, F.; Huang, Q.; Fu, X.; Zhang, L.; Yu, S., Preparation and characterisation of crosslinked waxy potato starch. *Food Chemistry* **2009,** *115* (2), 563-568.

21. Liu, X.; Wang, Y.; Yu, L.; Tong, Z.; Chen, L.; Liu, H.; Li, X., Thermal degradation and stability of starch under different processing conditions. *Starch - Stärke* **2013,** *65* (1-2), 48-60.

22. Stawski, D., New determination method of amylose content in potato starch. *Food Chemistry* **2008,** *110* (3), 777-781.

23. Liu, Y.; Yang, L.; Ma, C.; Zhang, Y., Thermal behavior of sweet potato starch by non-isothermal thermogravimetric analysis. *Materials (Basel, Switzerland)* **2019,** *12* (5), 699.

24. Karić, N.; Grzetic, J.; Đolić, M.; Kovacevic, T.; Pecić, L.; Radovanović, Ž.; Marinkovic, A., Preparation and properties of hydrogen peroxide oxidized starch for industrial use. *Hemijska industrija* **2020,** *74*, 25-36.

25. Rudnik, E.; Matuschek, G.; Milanov, N.; Kettrup, A., Thermalstability and degradation of starch derivatives. *Journal of Thermal Analysis and Calorimetry* **2006,** *85* (2), 267-270.

26. Vanier, N. L.; El Halal, S. L. M.; Dias, A. R. G.; da Rosa Zavareze, E., Molecular structure, functionality and applications of oxidized starches: A review. *Food Chemistry* **2017,** *221*, 1546-1559.

27. Zhang, Z.; Macquarrie, D. J.; Clark, J. H.; Matharu, A. S., Chemical modification of starch and the application of expanded starch and its esters in hot melt adhesive. *RSC Advances* **2014,** *4* (79), 41947-41955.

28. Lu, Y.; Zhang, S.; Geng, Z.; Zhu, K.; Zhang, M.; Na, R.; Wang, G., Hybrid formation of graphene oxide–POSS and their effect on the dielectric properties of poly(aryl ether ketone) composites. *New Journal of Chemistry* **2017,** *41* (8), 3089-3096.

29. Divakaran, N.; Kale, M. B.; Senthil, T.; Mubarak, S.; Dhamodharan, D.; Wu, L.; Wang, J., Novel unsaturated polyester nanocomposites via Hybrid 3D POSS-modified graphene oxide reinforcement: electro-technical application perspective. *Nanomaterials (Basel)* **2020,** *10* (2).

30. Sirin, H.; Turan, D.; Ozkoc, G.; Gurdag, S., POSS reinforced PET based composite fibers: "Effect of POSS type and loading level". *Composites Part B: Engineering* **2013,** *53*, 395-403.

31. Song, J.; Zhao, J.; Ding, Y.; Chen, G.; Sun, X.; Sun, D.; Li, Q., Effect of polyhedral oligomeric silsesquioxane on water sorption and surface property of Bis-GMA/TEGDMa composites. *Journal of Applied Polymer Science* **2012,** *124* (4), 3334-3340.

32. Hirohara, T.; Kai, T.; Ohshita, J.; Kaneko, Y., Preparation of protic ionic liquids containing cyclic oligosiloxane frameworks. *RSC Advances* **2017,** *7* (17), 10575-10582.

33. Ramírez, M. G. L.; Muniz, G. I. B. d.; Satyanarayana, K. G.; Tanobe, V.; Iwakiri, S., Preparation and characterization of biodegradable composites based on Brazilian cassava starch, corn starch and green coconut fibers. *Matéria (Rio de Janeiro)* **2010,** *15* (2), 330-337.

34. Marinich, J. A.; Ferrero, C.; Jiménez-Castellanos, M. R., Graft copolymers of ethyl methacrylate on waxy maize starch derivatives as novel excipients for matrix tablets: Physicochemical and technological characterisation. *European Journal of Pharmaceutics and Biopharmaceutics* **2009,** *72* (1), 138-147.

35. Kumar; Ganure, A.; Subudhi, b. b.; Shukla, S., Synthesis and characterization of pH sensitive ampiphillic new copolymer of methyl methacrylate grafted on modified starch: Influences of reaction variables on grafting parameters. *International Journal of Pharmacy and Pharmaceutical Sciences* **2014,** *6*, 868-880.

36. Dome, K.; Podgorbunskikh, E.; Bychkov, A.; Lomovsky, O., Changes in the crystallinity degree of starch having different types of crystal structure after mechanical pretreatment. *Polymers (Basel)* **2020,** *12* (3).

37. Aradhana, R.; Mohanty, S.; Nayak, S. K., Comparison of mechanical, electrical and thermal properties in graphene oxide and reduced graphene oxide filled epoxy nanocomposite adhesives. *Polymer* **2018,** *141*, 109-123.

2.8. SUPPORTING INFORMATION

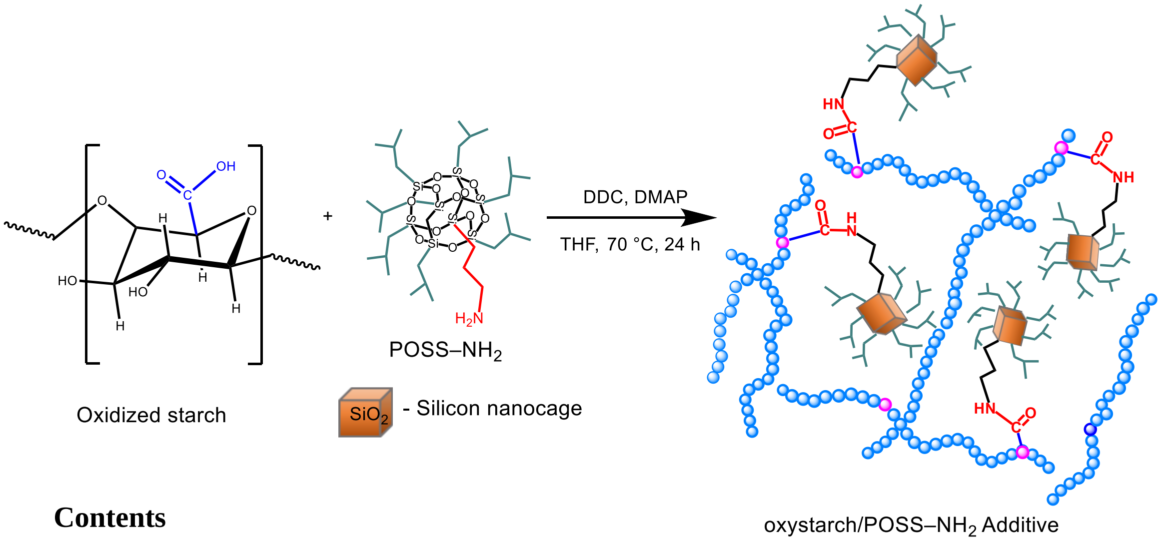

Contents

2.S1. Water droplets on the hydrophobically modified oxystarch surface

2.S1. WATER DROPLETS ON THE HYDROPHOBICALLY MODIFIED OXYSTARCH SURFACE

The contact angle measurements were carried out to study the hydrophobic properties of the modified oxystarch surface. When the water droplet was in contact with the oxystarch surface, it was observed that the shape was distorted due to the absorption of water to the surface. The pictures were taken at 10 S and 5 min and are shown in Figure 2.S1.

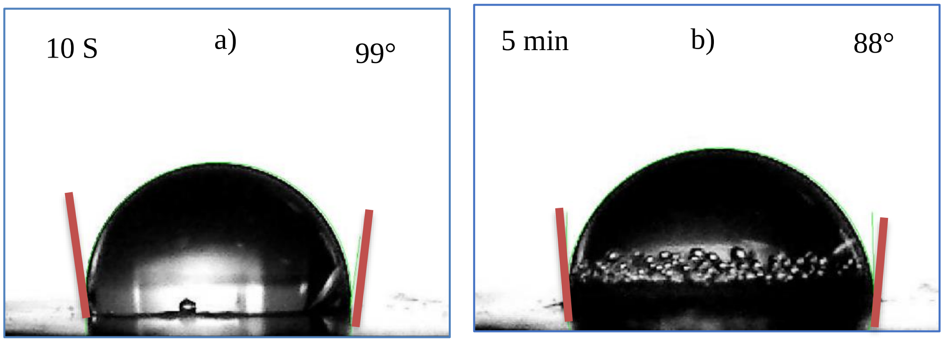

Figure 2.S1. The picture of water droplets a) after 10 S and b) after 5 min on the modified starch surface.

2.S2. THE DEFINITION AND DERIVATION OF DERIVATION OF DEGREE OF SUBSTITUTION (DS) EQUATION

The derivation of the equation used to calculate the degree of substitution of POSS-NH_2 to the starch is based on:

$$\mathrm{DS} = \frac{\text{Number of moles of POSS-NH}_2\text{ moieties}}{\text{Number of moles of glucose units}} \tag{2.S1}$$

The number of moles of silicon atoms in the product can be calculated as:

$$\text{Number of moles of Si atoms} = \frac{m_{Si}}{M_{Si}} \tag{2.S2}$$

where M_{Si} is the atomic mass of silicon which is 28.09 g/mol and the m_{Si} is the mass of silicon atoms in the sample. According to the stoichiometry of Si: POSS-NH_2 is 8:1. Therefore, the number of moles of POSS-NH2 can be calculated as:

$$\text{\# moles of POSS-NH}_2 = \frac{\mathrm{m_{Si}}}{\mathrm{M_{Si}}} \times \frac{1}{8} = \frac{\mathrm{m_{Si}}}{224.7} \tag{2.S3}$$

where $\mathrm{m_{Si}}$ was estimated from the XRF analysis and 224.7 is the total mass of silicon atoms in the POSS cage. The number of moles of POSS-NH_2 can be converted to the mass of POSS-NH_2 as:

$$\text{Mass of POSS-NH}_2 = \frac{\mathrm{m_{Si}}}{224.7} \times 874.5 \tag{2.S4}$$

$$\text{Mass of glucose} = 100 - \mathrm{m_{POSS\text{-}NH2}} = 100 - \frac{\mathrm{m_{Si}}}{224.7} \times 874.5 \tag{2.S5}$$

$$\text{Number of moles of glucose} = \frac{100 - \frac{\mathrm{m_{Si}}}{224.7} \times 874.5}{162.14} \tag{2.S6}$$

where 162 is the molecular mass of glucose monomer in the starch and 874.5 is the molecular mass of POSS-NH_2. According to the definition of DS can be calculated as:

$$\mathrm{DS}=\frac{\frac{\mathrm{m}_{\mathrm{Si}}}{224}}{\frac{100-\frac{\mathrm{m}_{\mathrm{Si}}}{224}\times 874.5}{162.14}}=\frac{\text{Number of moles of POSS}-\mathrm{NH}_2}{\text{Number of moles of starch}} \qquad (2.\mathrm{S7})$$

Can be rearranged and rewritten as:

$$\mathrm{DS}=\frac{\mathrm{m}_{\mathrm{Si}}\times 162}{22470-(\mathrm{m}_{\mathrm{Si}}\times 874.5)} \qquad (2.\mathrm{S8})$$

2.S3. DYNAMIC MECHANICAL ANALYZER AND THE ADDITIVE-LOADED EPOXY SAMPLE

The mechanical analysis of the neat epoxy and the additive-loaded epoxy samples was carried out by DMA analysis. A picture of the DMA (TA Instruments, Q800) analyzer and the additive-filled epoxy sample loaded to the flex clamp is shown in Figure 2.S2.

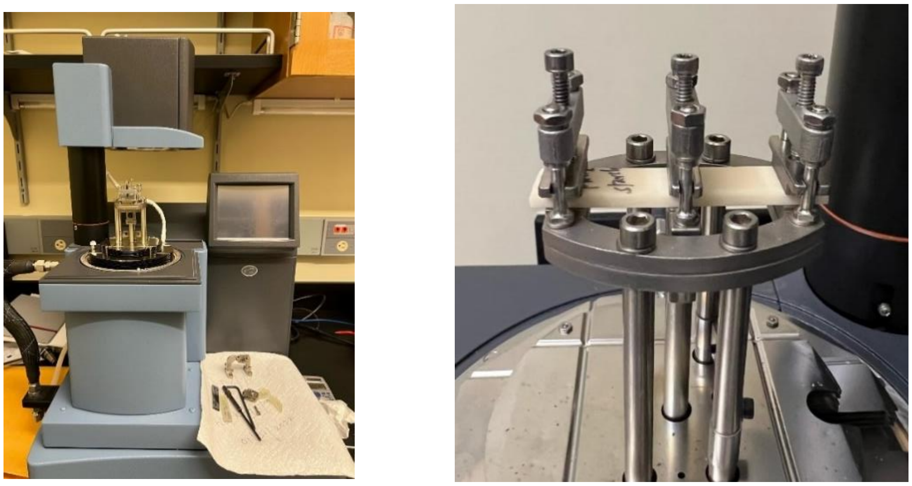

Figure 2.S2. Picture of DMA analyzer and additive loaded epoxy sample attached to the flex clamp.

2.S4. THE FTIR SPECTRA OF OXYSTARCH, POSS-NH_2, AND OXYSTARCH-POSS-NH_2

The partial FTIR spectra of oxystarch, POSS-NH_2, and oxystarch-POSS-NH_2 were shown in the text to produce an expanded view of the carbonyl region which was most important. The full FTIR spectra are shown in Figure 2.S3. The presence of O–H and C–H are noted in Figure 2.S3.

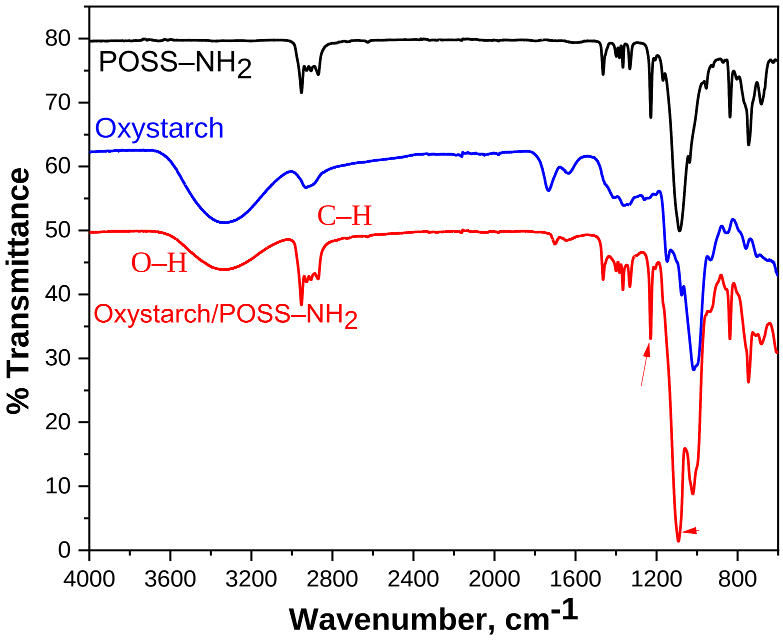

Figure 2.S3. The full spectra of oxystarch, POSS-NH$_2$, and oxystarch-POSS-NH$_2$

2.S5. CHEMICAL SHIFT OF POSS-NH$_2$ ^{1}H NMR SPECTRUM

The multiplicity and chemical shift of each peak in POSS-NH$_2$ ^{1}H NMR spectrum are shown in Table 2.S1. The chemical structure of the POSS-NH$_2$ molecule is shown in Figure 2.S4.

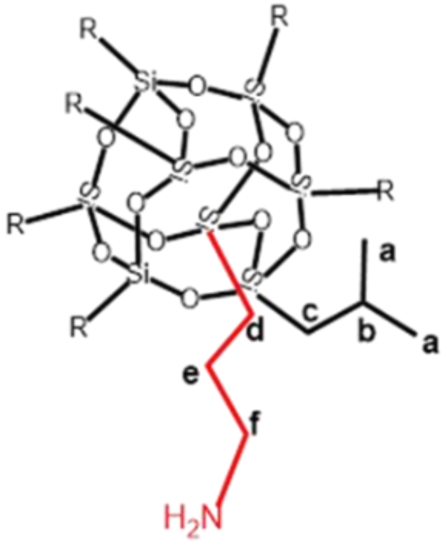

Figure 2.S4. The chemical structure of the POSS-NH$_2$ molecule.

Table 2.S1. The observed, expected and estimated integral of each ^1H NMR peak of POSS-NH_2

Label	Chemical shift	Observed Multiplicity	Expected multiplicity	Estimated Integral	Expected number of protons
d	0.58	doublets	triplet	15.8	2
c	0.63	singlet	doublet		14
a	0.9	doublet	doublet	41.7	42
e	1.52	Pentet	Pentet	2	2
b	1.85	Nonet	Nonet	7	7
f	2.66	triplet	triplet	1.93	2

CHAPTER III

INTRODUCTION, BACKGROUND, AND METHODS FOR GRAPHENE OXIDE (GO) DERIVATIVES

Graphene is a two-dimensional (2D) nanomaterial consisting of a single layer of sp^2-hybridized carbon atoms. Graphene was isolated from natural graphite by Andre Geim and Konstantin Novoselov, which resulted in the Nobel Prize for Physics in 2010 for their work. Graphene can be synthesized by chemical vapor deposition (CVD), and mechanical or electrochemical exfoliation methods. However, the industrial-scale applications of graphene are still limited due to constraints in synthesis, dispersion barriers, and large surface area requirements. As a result, graphene-based derivatives, such as multilayer graphene (MLG) and graphene oxide (GO), are more commonly studied for industrial applications.

GO has been studied over the past few decades as an additive for polymers and fiber-reinforced composites. The surface of GO, hosts oxygen-containing functional groups, such as hydroxyls, ketone, epoxides, and carboxylic acids. The inherent nature of these functional groups imparts hydrophilic characteristics to GO. Therefore, the performance of GO-based additives in hydrophobic polymers is limited due to their poor dispersion, low reactivity, or weak interface interactions.

Recently, the hydrophobic modification of GO with long-chain organic molecules has been used as an effective method to increase the compatibility of the hydrophilic GO surface with hydrophobic polymer composites. However, the major drawback of modified GO derivatives is the lower thermal stability and reduced crosslink density in the resin.[1-5]

Two projects that were carried out to investigate the effect of grafting two different types of polyhedral oligomeric silsesquioxane (POSS) molecules to the GO are reported in Chapters 5 and 6 of this dissertation. One project reports the study of polyvinyl pyrrolidone (PVP) on GO surface using temperature-modulated differential scanning calorimetry (TMDSC). The introduction to GO and its additives, their application in different polymer composites, and the background of the reaction conditions adopted throughout this dissertation will be discussed briefly in the following sections.

3.1. SYNTHESIS AND MODELS FOR GO STRUCTURE

For the first time, Brodie[6] synthesized graphene oxide from graphite using sodium chlorate and nitric acid as oxidizing agents.[7] Later, a more efficient and scalable method for producing GO was introduced by Hummers and Offeman.[8,9] The GO used in the work reported in Chapter 5 of this dissertation was produced in-house using the modified Hummers method while Chapters 4 and 6 used commercially available GO. A representative chemical structure of GO is shown in Figure 3.1.

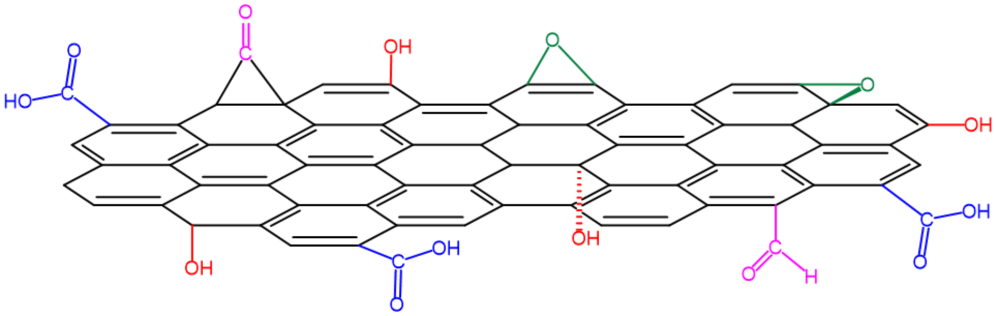

Figure 3.1. Schematic representation of GO.

Different types of functional groups that may be present on a GO surface are shown in Figure 3.1. However, the exact stoichiometry of the functional groups is not definitive and varies depending on the oxidation and processing conditions. The precise chemical structure has not been successfully estimated for several reasons, including a lack of existing analytical methods, the complexity of the system, and amorphous and non-stoichiometric characteristics.

Several models have been put forward to characterize the structure of GO.[10] The Hofmann–Rudolf model[11] was proposed in 1936 by assuming the distribution of epoxide groups on the basal plane of GO with the molecular formula of C_2O was random. The Ruess model,[12] that was introduced in 1946 considered the hydroxyl groups instead of the epoxide groups in the Hofmann–Rudolf model. Scholz and Boehm[13] have proposed a newer model by considering the rippled structure of GO and the presence of hydroxy, carbonyl, and alkene functional groups, and the absence of epoxide groups. The Nakajima and Matsuo model contains a stage 2 graphene-intercalated compound (GIC). In stage 2, there is no guest molecule present between the two graphene sheets. This model was based on the XRD data of graphite fluoride, $(C_2F)_n$. Leaf and Klinowski have introduced the L–K model,[14] based on ^{1}H NMR and ^{13}C NMR spectroscopy. The main assumptions of the model are the nearly flat surface of the carbon skeleton, random distributions of aromatic and aliphatic regions, and the distortion of the carbon atoms attached to the hydroxyl groups that results in a slightly rippled structure.

Szabó and coworkers[15] have introduced a modified version of the Scholz–Boehm model with a GO surface free of carboxylic acid groups. The characterization of the GO surface has been carried out by several analytical techniques, such as elemental analysis, transmission electron microscopy (TEM), XRD, and ^{13}C magic-angle spinning NMR spectroscopy.[15] The model proposed the existence of several types of functional groups such as tertiary OH, 1,3-ether, ketone, quinone, and phenol (aromatic diol) assuming the absence of carboxylic acid groups.

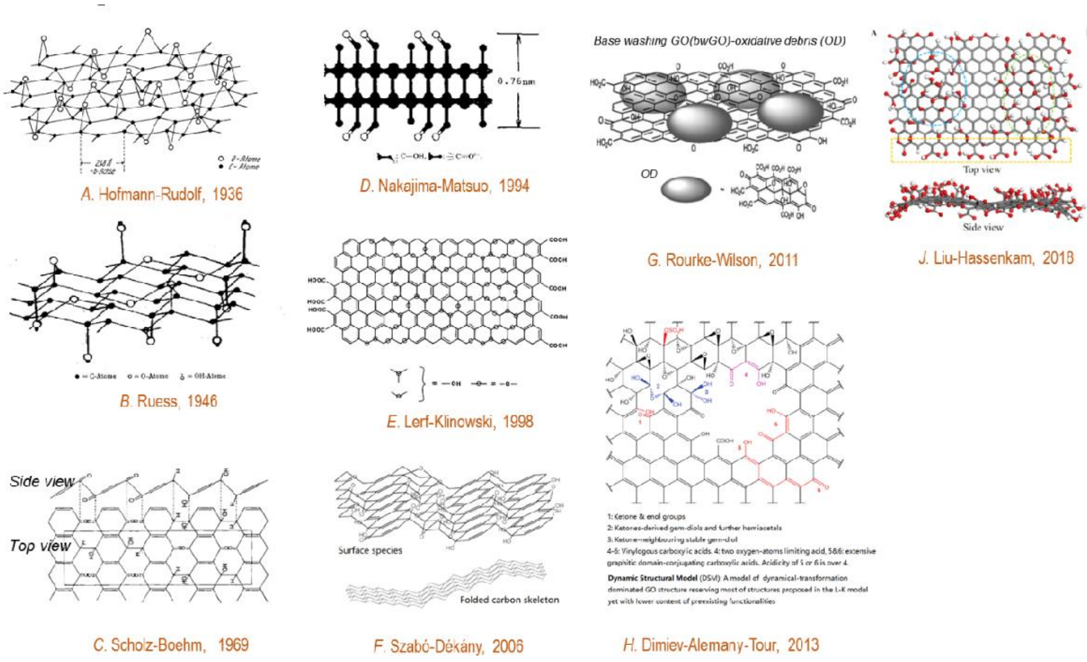

Figure 3.2. The different models of GO structure. (Reproduced from Sun Ling[16])

The non-covalently bound oxidative residues on the GO surface can act as surfactants to promote the exfoliation of sheets and ultimately efficient dispersion of GO sheets in suspensions.[17] Since this oxidative debris is non-covalently attached to the GO surface. It can be removed by washing with a base. Another report proposed a model to explain the acidity of GO in aqueous solutions.[18] That work suggested a dynamic structural model (DSM) for GO, in which the surface interacts with water and changes its structure. Several analytical techniques have been adopted to show that the GO surface does not contain many functional groups initially, but gradually generate new functional groups, on the surface through interactions with water.

The structure of GO can be characterized using several analytical methods, including XRD analysis.[19] The introduction of functional groups causes an increase in the interlayer distance of the graphene sheets. As a result, the crystal plane (001) distance varies from ∼3 to 8 Å from graphite to

GO. However, if the GO undergoes thermal treatment, the interlayer distance changes to about 7 Å in the resulting reduced GO (rGO).

3.2. SYNTHESIS AND APPLICATIONS OF GRAPHENE OXIDE (GO) DERIVATIVES

The use of GO as an additive for synthetic polymers provides an opportunity to tune the mechanical properties of polymers and resins. This dissertation focuses on methods to increase dispersion, reactivity, and hydrophobic characteristics of GO by grafting various types of POSS molecules, The thermal behavior of polyvinylpyrrolidone on reduced graphene oxide was studied using temperature-modulated differential scanning calorimetry.

3.2.1. Synthesis of amine-functionalized GO derivatives

Amine-functionalized GO derivatives are widely used as additives for polymers and resins. During the synthesis, the primary amine reacts with carboxylic acid groups of GO efficiently in the presence of N, N′–dicyclohexylcarbodiimide (DCC) and 4–dimethylaminopyridine (DMAP) as catalyst systems.[20] The reaction mechanism for a typical reaction is shown in Figure 3.3.

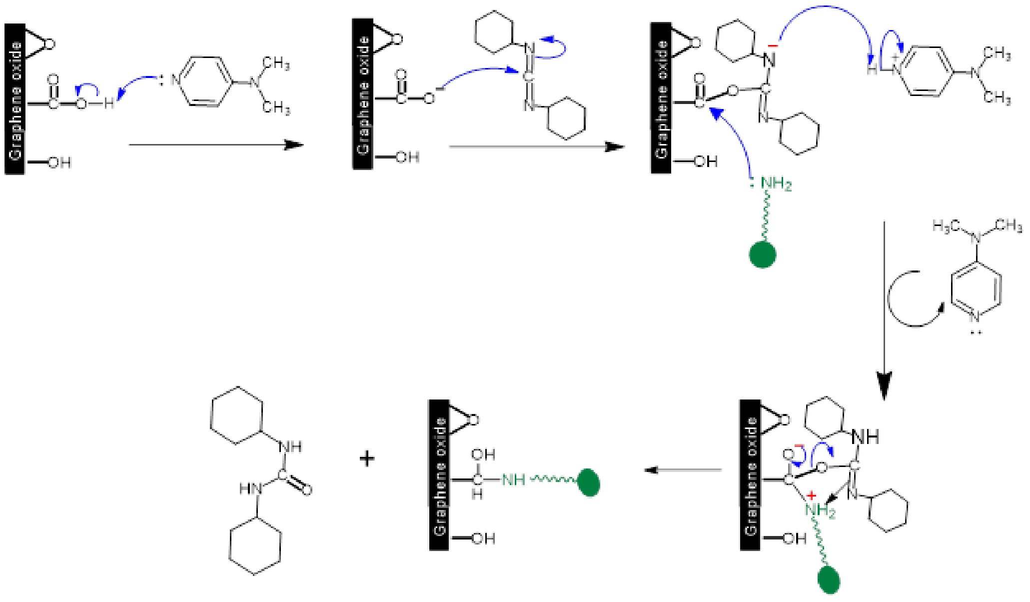

Figure 3.3. The reaction of GO with a primary amine in the presence of DDC and DMAP.

The amide formation between carboxylic acids with an amine in the presence of DMAP and DDC represents a Steglich–type reaction mechanism.[21] In a typical reaction, the role of DMAP is the deprotonation of acid groups on the GO. The lone pair of the nitrogen in the pyridine ring extracts the proton of the carboxylic acid group. The resultant oxide nucleophile reacts with the DDC coupling agent to make the intermediate. Finally, the amine nucleophile displaces the DCC coupling agent to form the amide bond between GO and POSS molecules.

3.2.2. GO and POSS-based additives for polymer composites

The use of graphene as an additive for polymer composites has been studied extensively in the past two decades due to its excellent electrical, optical, thermal, and mechanical properties. However, the performance of graphene in hydrophobic polymers and resins is limited by its poor dispersion. As water-dispersible GO has been developed from graphene, it has opened opportunities for derivatizing graphene sheets with different organic hydrophobic molecules that increase its dispersion in organic media. This dissertation reports efforts made to increase the dispersion of GO in polymers by increasing their hydrophobic characteristics. The scope of this dissertation is limited to the modification of GO using octaammonium polyhedral oligomeric silsesquioxane (OamPOSS) and aminopropyl isobutyl polyhedral oligomeric silsesquioxane (POSS–NH_2).

Several attempts have been made to evaluate the potential of GO-POSS-NH_2 as an additive for various resins. GO/POSS-NH_2 has been synthesized and tested as an additive for multifunctional applications.[5] The main goal of that study was to increase the compatibility of GO with organic solvents and resins. Therefore, after modification, the dispersion behavior of synthesized material in tetrahydrofuran were tested in various solvents such as (THF), hexane, chloroform, acetone, toluene, and pentane. The efficient dispersion of GO in organic solvents compared to pristine GO clearly shows the hydrophobic modification of the GO and the sessile drop contact angle was reported as 157°. The reaction was carried out in the presence of DDC as a catalyst in the THF for 48 h. The major drawbacks of this study are the large mass ratio (1:20) of GO to POSS–NH_2 and the long reaction time of 48 h.

Zhang et al.[4] have synthesized an additive by grafting POSS–NH_2 on GO using 1-ethyl-3-(3-dimethyl aminopropyl) carbodiimide (EDC) as a catalyst. After the modification reaction, the resulting additive had a sessile drop water contact angle of 152°. This additive increased the corrosion resistance of anticorrosive marine coatings. Furthermore, incorporating POSS–NH_2 resulted in long-lasting corrosion inhibition compared to the pristine GO. GO/POSS–NH_2 (0.1 wt%) have used nanocomposites[22] within unsaturated polyesters to increase stress load transfer towards the polymer matrix. This additive has shown increased thermal stability (69.8 °C), tensile strength (61.9%), and thermal conductivity (by 10^8 S m^{-1}) compared to bulk PU. Also, several other promising improvements include increased hydrophobicity, coefficient of friction, and other mechanical properties. The major drawback of this work is the large GO: POSS mass ratio. The commercialization of this product is challenging due to its high price. Therefore, Chapter 6 of this dissertation provides an alternative approach to achieving the hydrophobic properties of graphene oxide.

One-pot synthesis of OamPOSS–grafted GO has been carried out using a DCC catalyst as an additive for waterborne polyurethane (WPU) resins.[23] The product has been characterized using TEM, high-resolution transmission electron microscopy (HRTEM), scanning electron microscopy (SEM), XRD, and several analytical tools. Grafting with OamPOSS imparts hydrophobic characteristics to the surface of the GO. After the grafting reaction, the GO sheets were exfoliated and characterized using XRD. As a result of modification with OamPOSS, the GO sheets had excellent dispersion in resins and organic media. The mechanical properties of the WPU resin increased in the presence of the GO–OamPOSS additive (0.2 wt%). The tensile strength of the pristine WPU was 10 MPa and increased up to 25.5 MPa with the addition of GO–OamPOSS, that is, a 152% increase compared to pristine WPU.

Yu et al.[24] have synthesized the OamPOSS–GO and tested it as a potential additive for epoxy resin for corrosion inhibition. Their study found that grafting OamPOSS to GO increased the solubility of the GO in organic solvents and its dispersion in epoxy resins. In the small load of additive, e.g., 0.2 wt%, reduced the dielectric constant and dielectric loss of epoxy resins. This additive has been tested as an interfacial modifier for carbon fiber–reinforced epoxy composites.[2] The FTIR spectrum of the product showed a peak at 1530 cm^{-1} that can be assigned to the newly formed amide bond between POSS and GO. Further, XRD spectra of the products showed increased d-spacing of the graphene sheets due to the intercalation of POSS molecules. The carbon fiber surface was treated with OamPOSS–GO before the composite panels were prepared. As a result, the surface energy and wettability of the carbon fiber increased, and ultimately, the resulting carbon fiber composites had an increased interfacial strength 53% greater than GO-functionalized carbon fiber. OamPOSS functionalized GO, has been tested to use as an additive for the corrosion protection of hot-dip–galvanized steel. The efficient dispersion of OamPOSS–GO hybrid materials in THF has been achieved compared to the dispersion of pristine GO. Further, the additive has shown efficient dispersion in waterborne acrylic acid (WAA). The grafting of POSS to GO has shown increased anti-corrosion properties in WAA resin.

3.3. ADSORPTION OF POLYMERS TO SOLID SURFACES

Polyvinyl pyrrolidone (PVP) is a water-soluble polymer that has been used in a large number of applications such as binders, polymer films, solar cells, thickening agents, and healthcare products.[25] The properties of bulk PVP can be exploited by using additives and fillers. PVP has often been used with silica and GO-based additives in composites.[26,27] When PVP mixes with additives, the properties of the polymer in the composites differ from their bulk properties due to the interaction of the polymers with the corresponding solid surfaces.

The amount of polymer adsorbed on surfaces causes different behaviors, including thermal activity, than those found in bulk polymers. It is useful to accurately estimate the composition of the composite to understand these properties. The mass fraction of each material in the composite can be estimated using thermogravimetric analysis ($_{TG}$A). The amount of polymer on the composite can be expressed as adsorbed amount (AA) or wt%. AA is the mass of polymer, in this case, PVP (in mg) per surface area of the substrate (in m^2). In this dissertation, the amount of PVP on the GO surface is expressed as AA which can be defined using the equation:

$$AA=\frac{m_{PVP}}{m_{GO}\times SSA} \tag{3.1}$$

where m_{PVP} , m_{GO}, and SSA are the mass of PVP, the mass of GO, and the specific surface area of GO, respectively. The AA is used as a convenient way to characterize such small amounts of polymer on solid surfaces. In these systems, some understanding of the behavior of polymers on solid surfaces can be achieved using a Loop–Train–Tail model.[28,29]

3.3.1. Loop–Train–Tail model

The structure of the polymer on a surface and interface interactions are important in the overall properties of the composite. A possible rearrangement of the polymer on the GO surface can be interpreted using a Loop–Train–Tail model, A schematic representation of the model is shown in Figure 3.4.

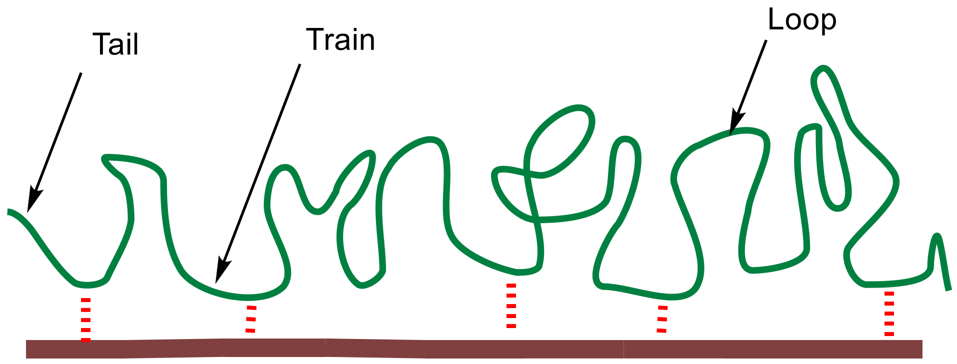

Figure 3.4. Polymer on the GO surface

According to the model, the segmental structure of the polymer on the surface can be divided into three different types; They are (1) The polymer molecules closer to the surface are called trains. These segments make the strongest interactions with the surface due to proximity and make the largest contribution to altering the thermal signature of the bulk polymer. (2) The loops connected to the trains, and the ones that reside away from the surface and have a thermal properties approach those of the bulk polymer. (3) The polymer segments at the end of the chains are called tails and have a similar thermal signature that depend on their interactions with the surface. When the tails are towards the surface, they show thermal signature similar to trains. Chapter 6 of this dissertation reports the work done to investigate the thermal behavior of polyvinyl pyrrolidone on a GO surface using temperature-modulated differential scanning calorimetry. The loop–train–tail model was used as a foundation and developed a new model to estimate the bound fraction of PVP on the GO surface.

3.4. MOTIVATION

GO has huge potential as an additive and interfacial modifier for polymers and composites. However, GO has several drawbacks, including incompatibility with hydrophobic polymers, low reactivity, dispersion problems, and moisture absorption. In contrast, POSS-based compounds have shown the potential to increase the compatibility of starch and GO with polymers once grafted. In this dissertation, different types of polyhedral oligomeric silsesquioxane grafted on starch and GO were tested as additives for epoxy resins.

3.5. METHODS

3.5.1. Differential scanning calorimetry

Differential scanning calorimetry (DSC) is a major method to characterize polymers and polymer composites. The characterization includes the glass transition temperature, rate of crosslinking, heat capacity, melting, and crystallization temperatures. The working principle of the instrument is the measurement of the difference in heat flows between the sample pan and the reference pan as a function of temperature. The sample pan contains the sample, whereas the reference pan is usually empty. Temperature-modulated DSC (TMDSC) is a more sensitive form of DSC introduced in 1993.[30] The working principle and theory behind TMDSC will be discussed in the following paragraph.

In TMDSC data analysis, the total heat flow of the sample is divided into two components: reversing and non-reversing heat flow.[30,31] TMDSC uses two simultaneous heating rates, the linear heating rate, and the modulated or sinusoidal heating rate. The heat flow signal of an MDSC experiment can be shown as:

$$\frac{\mathrm{dH}}{\mathrm{dt}} = \mathrm{C_p}\frac{\mathrm{dT}}{\mathrm{dt}} + f(\mathrm{T},\mathrm{t}) \qquad 3.2$$

where $\frac{\mathbf{dH}}{\mathbf{dt}}$ is the total heat flow equivalent to a standard DSC experiment, $\mathbf{C_p}\frac{\mathbf{dT}}{\mathbf{dt}}$ is the reversing heat flow component of the total heat flow, and C_p and f(T,t) are the heat capacity and kinetic component of the total heat flow, respectively.

3.5.1.1. Data processing of TMDSC

The data processing of TMDSC thermograms for polymer composites provides critically useful information. The scope of this dissertation is limited to estimating the change in the specific heat capacity of the polymer in PVP-GO composites. For that purpose, the area under each thermal transition, change of specific heat capacity of composite (ΔC_{sample}), were estimated as a Gaussian peak fitting using Origin software. The TMDSC thermograms of each sample were analyzed, and the areas under the bulk-like transitions were estimated. The resultant ΔC_{sample} was normalized based on the mass of PVP. The detailed estimation and modeling are discussed in Chapter 6.

3.6. REFERENCES:

1. Zhang, M.; Yan, H.; Yuan, L.; Liu, C., Effect of functionalized graphene oxide with hyperbranched POSS polymer on mechanical and dielectric properties of cyanate ester composites. *Royal Society of Chemistry Advances* **2016,** *6* (45), 38887-38896.

2. Zhang, R. L.; Gao, B.; Du, W. T.; Zhang, J.; Cui, H. Z.; Liu, L.; Ma, Q. H.; Wang, C. G.; Li, F. H., Enhanced mechanical properties of multiscale carbon fiber/epoxy composites by fiber surface treatment with graphene oxide/polyhedral oligomeric silsesquioxane. *Composites Part A: Applied Science and Manufacturing* **2016,** *84*, 455-463.

3. Tang, C.; Yan, H.; Li, S.; Li, M.; Chen, Z., Novel phosphorus-containing polyhedral oligomeric silsesquioxane functionalized Graphene oxide: preparation and its performance on the mechanical and flame-retardant properties of bismaleimide composite. *Journal of Polymer Research* **2017,** *24* (10).

4. Ye, Y.; Zhang, D.; Liu, T.; Liu, Z.; Liu, W.; Pu, J.; Chen, H.; Zhao, H.; Li, X., Improvement of anticorrosion ability of epoxy matrix in simulate marine environment by filled with superhydrophobic POSS-GO nanosheets. *Journal Hazard Materials* **2019,** *364*, 244-255.

5. Xue, Y.; Liu, Y.; Lu, F.; Qu, J.; Chen, H.; Dai, L., Functionalization of graphene oxide with polyhedral oligomeric silsesquioxane (POSS) for multifunctional applications. *Journal of Physical Chemistry Letters* **2012,** *3* (12), 1607-12.

6. Brodie, B. C., XIII. On the atomic weight of graphite. *Philosophical Transactions of the Royal Society of London* **1859,** *149*, 249-259.

7. Feicht, P.; Biskupek, J.; Gorelik, T. E.; Renner, J.; Halbig, C. E.; Maranska, M.; Puchtler, F.; Kaiser, U.; Eigler, S., Brodie's or Hummers' Method: Oxidation conditions determine the structure of graphene oxide. *Chemistry* **2019,** *25* (38), 8955-8959.

8. Hummers, W. S.; Offeman, R. E., Preparation of graphitic oxide. *Journal of the American Chemical Society* **1958,** *80* (6), 1339-1339.

9. Justh, N.; Berke, B.; László, K.; Szilágyi, I. M., Thermal analysis of the improved Hummers' synthesis of graphene oxide. *Journal of Thermal Analysis and Calorimetry* **2017,** *131* (3), 2267-2272.

10. Dreyer, D. R.; Park, S.; Bielawski, C. W.; Ruoff, R. S., The chemistry of graphene oxide. *Chemical Society Reviews* **2010,** *39* (1), 228-40.

11. Hofmann, U.; Holst, R., Über die Säurenatur und die Methylierung von Graphitoxyd. *Berichte der deutschen chemischen Gesellschaft (A and B Series)* **1939,** *72* (4), 754-771.

12. Ruess, G.; Vogt, F., Höchstlamellarer Kohlenstoff aus Graphitoxyhydroxyd. *Monatshefte für Chemie und verwandte Teile anderer Wissenschaften* **1948,** *78* (3), 222-242.

13. Scholz, W.; Boehm, H. P., Untersuchungen am graphitoxid. VI. betrachtungen zur struktur des graphitoxids. *Zeitschrift für anorganische und allgemeine Chemie* **1969,** *369* (3-6), 327-340.

14. Lerf, A.; He, H.; Forster, M.; Klinowski, J., Structure of graphite oxide revisited. *The Journal of Physical Chemistry B* **1998,** *102* (23), 4477-4482.

15. Szabó, T.; Berkesi, O.; Forgó, P.; Josepovits, K.; Sanakis, Y.; Petridis, D.; Dékány, I., Evolution of surface functional groups in a series of progressively oxidized graphite oxides. *Chemistry of Materials* **2006,** *18* (11), 2740-2749.

16. Sun, L., Structure and synthesis of graphene oxide. *Chinese Journal of Chemical Engineering* **2019,** *27* (10), 2251-2260.

17. Rourke, J. P.; Pandey, P. A.; Moore, J. J.; Bates, M.; Kinloch, I. A.; Young, R. J.; Wilson, N. R., The real graphene oxide revealed: stripping the oxidative debris from the graphene-like sheets. *Angewandte Chemie International Edition English* **2011,** *50* (14), 3173-7.

18. Dimiev, A. M.; Alemany, L. B.; Tour, J. M., Graphene Oxide. Origin of acidity, its instability in water, and a new dynamic structural model. *ACS Nano* **2013,** *7* (1), 576-588.

19. Johra, F. T.; Lee, J.-W.; Jung, W.-G., Facile and safe graphene preparation on solution based platform. *Journal of Industrial and Engineering Chemistry* **2014,** *20* (5), 2883-2887.

20. Sheehan, J. C.; Hess, G. P., A New method of forming peptide bonds. *Journal of the American Chemical Society* **1955,** *77* (4), 1067-1068.

21. Lutjen, A. B.; Quirk, M. A.; Barbera, A. M.; Kolonko, E. M., Synthesis of (E)-cinnamyl ester derivatives via a greener Steglich esterification. *Bioorganic & Medicinal Chemistry* **2018,** *26* (19), 5291-5298.

22. Divakaran, N.; Kale, M. B.; Senthil, T.; Mubarak, S.; Dhamodharan, D.; Wu, L.; Wang, J., Novel unsaturated polyester nanocomposites via Hybrid 3D POSS-modified graphene oxide reinforcement: electro-technical application perspective. *Nanomaterials (Basel)* **2020,** *10* (2).

23. Hu, L.; Jiang, P.; Bian, G.; Huang, M.; Haryono, A.; Zhang, P.; Bao, Y.; Xia, J., Effect of octa(aminopropyl) polyhedral oligomeric silsesquioxane (OapPOSS) functionalized graphene oxide on the mechanical, thermal, and hydrophobic properties of waterborne polyurethane composites. *Journal of Applied Polymer Science* **2017,** *134* (6), 1-11.

24. Yu, W.; Fu, J.; Dong, X.; Chen, L.; Shi, L., A graphene hybrid material functionalized with POSS: synthesis and applications in low-dielectric epoxy composites. *Composites Science and Technology* **2014,** *92*, 112-119.

25. Kurakula, M.; Rao, G. S. N. K., Pharmaceutical assessment of polyvinylpyrrolidone (PVP): As excipient from conventional to controlled delivery systems with a spotlight on COVID-19 inhibition. *J Drug Deliv Sci Technol* **2020,** *60*, 102046-102046.

26. Chen, S.; Cheng, B.; Ding, C., Synthesis and characterization of Poly(vinyl pyrrolidone)/Reduced graphene oxide nanocomposite. *Journal of Macromolecular Science, Part B* **2015,** *54* (4), 481-491.

27. Zou, R.; Su, L.; Zhang, L.; Hu, N.; Yue, D., Polyvinyl pyrrolidone grafted silica reinforced hydrogenated carboxylated nitrile latex film with improved mechanical properties. *Composites Communications* **2017,** *6*, 25-28.

28. Blum, F. D.; Young, E. N.; Smith, G.; Sitton, O. C., Thermal analysis of adsorbed poly(methyl methacrylate) on silica. *Langmuir* **2006,** *22* (10), 4741-4744.

29. Khatiwada, B. K.; Blum, F. D., Tightly bound PMMA on silica has reduced heat capacities. *Langmuir* **2019,** *35* (35), 11482-11490.

30. Simon, S. L., Temperature-modulated differential scanning calorimetry: theory and application. *Thermochimica Acta* **2001,** *374* (1), 55-71.

31. Thomas, L. C., Modulated DSC® Basics; Calculation and calibration of MDSC® signals. *TA instruments*.

CHAPTER IV

OCTA-AMMONIUM POSS (OamPOSS) GRAFTED GRAPHENE OXIDE (GO) AS AN ADDITIVE FOR EPOXY RESIN

Ishan N. Jayalath[a], Sedhuraman J. Mathiravedu[b], Pralhad Lamichhane[c], Bhishma Sedai[b], Ranji Vaidyanathan[c], Frank D. Blum[a]*

[a] Department of Chemistry, Oklahoma State University, Stillwater, OK.

[b] MITO Material Solutions, Inc., Indianapolis, IN.

[c] School of Materials Science and Engineering, Oklahoma State University, Tulsa, OK.

4.1. ABSTRACT

Octa-ammonium polyhedral oligomeric silsesquioxane (OamPOSS)-grafted graphene oxide (GO) was synthesized and used as an additive to improve the mechanical properties of systems using epoxy resins. The chemical, thermal, and physical characterization of the OamPOSS–GO additive was conducted with FTIR, X-ray fluorescence spectroscopy (XRF), differential scanning calorimetry (DSC), and thermogravimetric analysis (TGA) analyses.

The additive was dispersed in epoxy resin using a three-roll mill followed by a speed mixer. The effect of various additive loadings on the mechanical properties of epoxy was studied using dynamic mechanical analysis (DMA), and the results were compared with neat epoxy. Incorporating the OamPOSS–GO additive significantly increased storage and loss moduli compared to neat epoxy. The loss moduli of the 1% and 2% additive-loaded samples were increased by 60%, and the storage modulus increased by 39% compared to the neat epoxy sample at 30 °C. The OamPOSS–GO materials have good potential as additives for moderately hydrophobic resins, such as epoxies.

4.2. INTRODUCTION

The revolutionary discovery of graphene-based materials by Geim and Novolselov resulted in the Nobel Prize for Physics in 2010. Since then, graphene, graphene oxide (GO), and reduced graphene oxide (rGO) based products have been developed for numerous applications.[1-4] GO-based additives have often been used compared to pristine graphene due to their higher solubility in solvents, ease of synthesis, and the possibility of surface functionalization.[5] The sp^2-hybridized carbon surface of GO hosts oxygen-containing functional groups, such as hydroxyls, ketones, epoxides, and carboxylic acids. The hydrophilic nature of these functional groups can be detrimental to the performance of GO-based additives in moderately hydrophobic resins, such as epoxies.[6] This reduction may be due to poor dispersion, low reactivity, and weak interfacial interactions with many polymers.[7-9] Recently, hydrophobic modifications of GO with long-chain organic molecules were used to increase the compatibility between the hydrophilic graphene oxide surfaces and the hydrophobic polymer matrix.[4,10] However, due to the poor thermal stability of the organic moieties grafted onto the GO surfaces, the modified additives compromised the thermal stability of the composites and reduced the crosslinking density of the resin during the curing of the composite.[2,11-14]

Octaammonium polyhedral oligomeric silsesquioxane (OamPOSS) is a hybrid inorganic-organic nanomaterial comprised of a nanoscale silica cage surrounded by amine-functionalized organic vertex groups.[15-17] The silica core of POSS has a cage shape with a side length of 0.53 nm.[4] The product of grafting OamPOSS to GO (OamPOSS–GO) could replace pristine GO and be a much more efficient nanofiller in multiple ways. (1) The organic functional groups of POSS can facilitate efficient dispersion of GO in the nonpolar media. Combining the oxygenated (hydrophilic) functional groups on the GO surface with the hydrophobic functional groups of OamPOSS can ultimately lead to a product with amphiphilic characteristics. (2) The grafting of POSS molecules to GO exfoliates the graphene sheets, which also increases the dispersion of the additive in the organic solvents and polymers. (3) The amine functional groups of POSS can be involved in crosslinking reactions, resulting in a chemical bond between the graphene sheets and the resin. As a result of the strong interaction of the polymer with the additive and proper dispersion, the mechanical properties of the composites, including strength, modulus, and toughness, can increase.[8,12] (4) The silica cage can act as a heat sink that reduces thermal conduction in the composites and ultimately increases their thermal stability. Only a few studies have been performed to evaluate the effect of OamPOSS–GO on the mechanical properties of composites.

In this study, OmPOSS was covalently grafted to GO via the amine groups of OamPOSS and the carboxylic acid groups of GO. The OamPOSS-grafted GO hybrid material was characterized using Fourier transform infrared (FTIR) spectroscopy, thermogravimetry, X-ray fluorescence (XRF) spectroscopy, dispersion analysis, and mechanical testing. The OamPOSS–GO was added to masterbatch epoxy resin (4%) using a three-roll mill and diluted to obtain a series of dispersions (0.1%, 0.5%, 1.0%, and 2.0%). The main objective of this study was to evaluate the effect of OamPOSS–GO hybrid materials on the thermal and mechanical properties of filled epoxy resin. The thermal and mechanical properties of additive-filled resins were evaluated by thermogravimetric analysis (TGA), temperature-modulated differential scanning calorimetry (TMDSC), and dynamic mechanical analysis (DMA).

4.3. MATERIALS AND METHODS

4.3.1. Materials

The GO dispersion (2.5 wt%) was purchased from Sigma Aldrich (St. Louis, MO, USA) and OamPOSS from Hybrid Plastics (Hattiesburg, MS, USA). Analytical grade 4-dimethyl aminopyridine (DMAP) and 1-ethyl-3-(3-dimethyl aminopropyl)-carbodiimide (EDC) were purchased from Spectrum Chemicals (New Brunswick, NJ, USA). These materials were used directly without further purification, modification, or other treatments.

The Hexion-EPON 828 epoxy resin (Skygreek Inc, LaGrangeville, NY, USA) was used for this study because it is used in a wide variety of applications. The viscosity, epoxy equivalent weight, and color of the resin were reported as 11,000–15,000 cP, 185–192 g/mol, and light yellow, respectively. Epicure 3370 (Skygreek Inc, LaGrangeville, NY, USA) was used as a curing agent, of which, the viscosity and amine values are reported as 8500–14500 cP, and 384–407 mg/g, respectively. The mixing ratio of EPON 862 to hardener was 100:44 by weight. The mixing ratio of epoxy to amine was 100:44 by mass.

4.3.2. Synthesis of OamPOSS–GO

Aqueous GO (1.5 g) was dispersed in 300 mL of deionized (DI) water in a 500-mL round-bottom flask and sonicated for 1 h to obtain a uniform dispersion. In a separate container, 1.5 g of OamPOSS and 500 mg of NaOH were dissolved in 25 mL of DI water. The two solutions were mixed and stirred at room temperature for 15 min. Next, 25 mg of EDC and 15 mg of DMAP were added to the mixture, and the reaction was allowed to proceed for 8 h at 75 °C. The product was then filtered using Whatman #2 filter paper and washed two times with 500 mL of DI water and four times with 250 mL of acetone. The crude product was collected and dried in a vacuum oven overnight at 60 °C before chemical characterization and dispersion in epoxy resin.

4.3.3 Characterization

Attenuated total reflection (ATR)-Fourier transformed infrared (FTIR) spectroscopy was used to characterize the OamPOSS–GO additive. The spectra were recorded with a Nicolet i550 spectrometer (Thermo Scientific, Waltham, Massachusetts, USA) equipped with a diamond crystal operating from 500 to 4500 cm^{-1}, a spectral resolution of 4 cm^{-1}, 64 scans, and automatic atmospheric suppression.

The elemental composition of the OamPOSS–GO was determined by XRF analysis. The change in the Si and N contents of the starch were estimated before and after grafting using a Philips PW 1410 XRF spectrometer.

The thermal identity of the OamPOSS–GO additive, epoxy resin, and additive-filled epoxy resin was tested using a Model Q50 Thermogravimetric Analyzer (TA Instruments, New Castle, DE, USA). The experiments were done in the air, using approximately 10 mg of sample and a 20 °C/min ramp rate.

The glass transition region of neat epoxy and additive-loaded samples were studied using TMDSC analysis. The total heat flow measurements were made with a Model Q2000 Differential Scanning Calorimeter (DSC) (TA Instruments). Tzero pans (TA Instruments) were used as both sample and reference pans, and the DSC cell was purged with nitrogen gas at a flow rate of 50 ml/min. The samples were equilibrated at 30 °C for 1 min and heated to 120 °C at a heating rate of 3 °C/min with a modulation amplitude of ± 1 °C with a period of 60 s.

The OamPOSS–GO additive was master-batched into the epoxy component of the resin (common name: PART A) using a three-roll calendaring mill. Dispersions of 0.1%, 0.5%, 1%, and 2% were obtained by diluting corresponding amounts of the masterbatch with PART A. Each dispersion was mixed well in a speed mixer for 2.5 min at 2500 rpm with the recommended amount of hardener from the supplier, degassed in a vacuum chamber for 2 min, and poured into rectangular molds. Then, the samples were allowed to cure at room temperature for 24 h and finally underwent post-curing at 80 °C for 6 h to obtain the test specimens.

The thermo-mechanical properties (e.g., flexural modulus) of the neat epoxy and additive-loaded epoxy samples were characterized using a Model Q800 Dynamic Mechanical Analyzer (DMA) (TA Instruments, New Castle, DE, USA). The specimens were polished using different grades of sandpaper to make similar widths and thicknesses for the tests. The storage modulus (G'), loss modulus (G''), and tan δ of the specimens were tested between 30 to 150 °C using the double cantilever mode under a fixed frequency of 1 Hz and a temperature ramp rate of 3 °C/min. The approximate size of the specimens was 35 mm × 12 mm × 3 mm (length × width × height).

4.4. RESULTS AND DISCUSSION

OamPOSS has eight organic vertex groups with terminal $-NH_3^+$ functional groups. We chose to use OamPOSS due to the greater abundance of $-NH_3^+$ groups compared to other similar amine-functionalized POSS molecules with monofunctional amine groups. However, according to the reaction mechanism (Steglich amidation), the nitrogen atom should have a lone pair of electrons to attack the carbonyl groups of EDC during the reaction. Hence, the cationic form of OamPOSS was not deemed useful ($-NH_3^+$) with the EDC/DMAP catalyst system due to its non-nucleophilic nature. Therefore, a strong base (NaOH) was used to convert the ammonium functional groups to amine groups before the reaction. The amidation reaction was carried out between the amine groups of OamPOSS and GO, as illustrated in Figure 4.1.

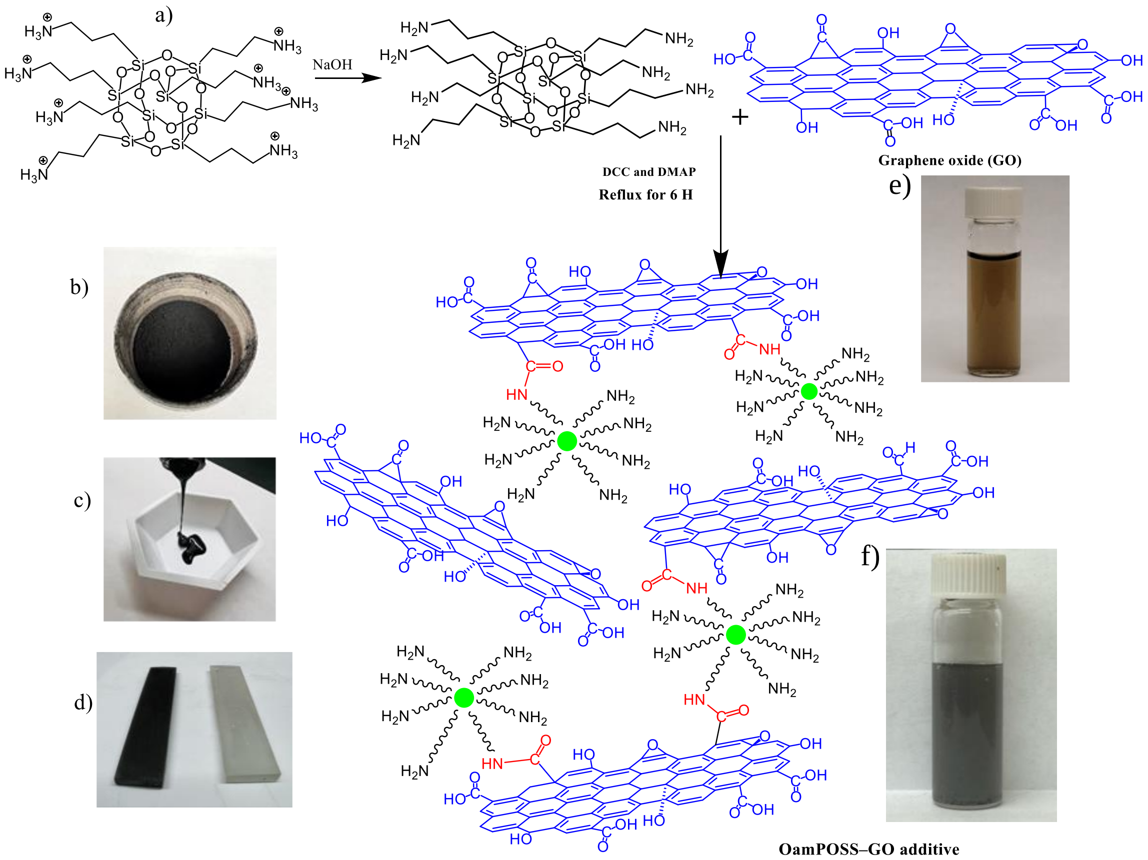

Figure 4.1. Scheme for grafting OamPOSS onto a GO surface, photographs of b) dried OamPOSS–GO additive, c) OamPOSS–GO/epoxy dispersion, d) specimens prepared for mechanical tests (yellowish opaque sample is the neat resin, and the black sample is the OamPOSS–GO-loaded epoxy), e) the picture of pristine graphene dispersion in water and f) picture of OamPOSS-GO dispersion in water.

4.4.1. OamPOSS–GO dispersion in solvents

The OamPOSS–GO dispersions were studied and compared with pure GO to investigate the effect of their reaction. The solvents used in the study were pentane (most hydrophobic), toluene, tetrahydrofuran, 2-propanol, and water (most hydrophilic). The resulting dispersions, or non-dispersions, are shown in Figure 4.2. Mixtures of GO with the clear solvents toluene and pentane show no dispersion of the GO, which settled on the bottom of the vial. The other solvents appeared to disperse the GO. In contrast, the OamPOSS–GO material showed efficient dispersion in all the s

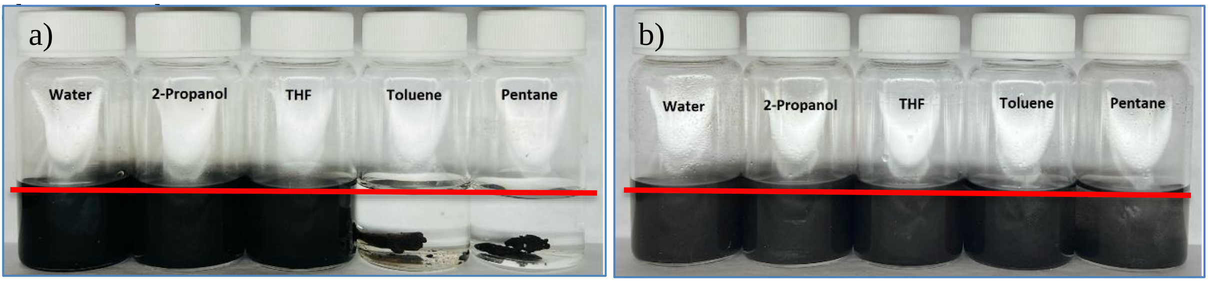

Figure 4.2. Dispersion of GO and OamPOSS–GO hybrid material in different solvents. Each solvent contains 5 mg/ml of material, and the photograph was taken after 5 min of ultrasonication for (a) GO and (b) OamPOSS–GO hybrid material. The red line drawn in the figure represents the top of the liquid (dispersion) level.

The hydroxyl and other functional groups on the GO surface impart a hydrophilic nature of GO that ultimately facilitates its stable dispersion in water, 2-propanol, and tetrahydrofuran (THF). It did not disperse in toluene or pentane. The OamPOSS–GO additive showed good dispersibility in all solvents, including water and pentane. These dispersions were stable 24 h after the sonication except for toluene. The dispersion of these materials may be understood based on the polar and nonpolar characteristics of the functional groups present in the GO and OamPOSS molecules. The dispersibility of OamPOSS–GO in toluene and pentane was significantly improved compared to that of GO due to the propyl groups of the silicon cage of OamPOSS.[18] The increased dispersion of OamPOSS–GO in toluene and pentane was achieved due to the reaction of the acid groups with the amine groups of OamPOSS. However, OamPOSS–GO showed less dispersion stability in pentane: it began to settle in the bottom of the vial a few minutes after being removed from the sonicator. The poor dispersion of GO in toluene and pentane is shown for comparison with OamPOSS–GO. Based on the dispersion study, modification with OamPOSS made the GO more amphiphilic, which suggested compatibility with both hydrophilic and hydrophobic polymer systems.

4.4.2. Fourier transform infrared (FTIR) spectroscopy

FTIR spectroscopy was used to identify the amide linkages in the OamPOSS–GO that provide evidence for covalent bonding between the amine groups of OamPOSS and the carboxylic acid groups of GO. A partial FTIR spectrum of the OamPOSS–GO hybrid material is shown in Figure 4.3. The FTIR spectra of POSS and GO are also shown for comparison. The spectra are shifted vertically, and the intensity of the pure OamPOSS spectrum is reduced for a better view of the low-intensity peaks in the OamPOSS–GO spectrum. The full spectrum is in shown Figure 4.S1 in the Supporting Information.

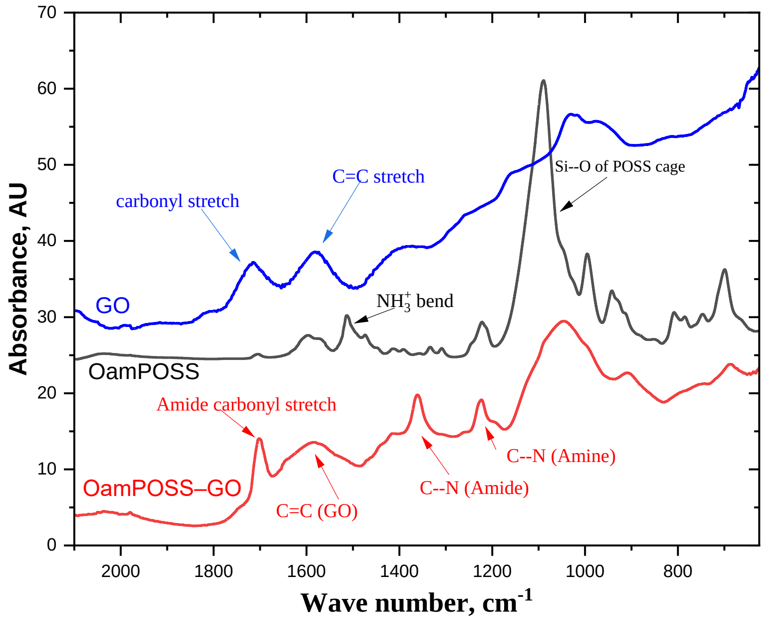

Figure 4.3. FTIR spectra of OamPOSS, OamPOSS–GO hybrid material, and GO. Some important peak assignments are labeled in the figure.[4,19-21]

In the FTIR spectrum of OamPOSS, the peak at 1089 cm^{-1} is assigned to the Si-O-Si in the POSS cage. The peaks at 1221 and 1596 cm^{-1} are assigned to the C-N stretching and NH_3^+ bending vibrations, respectively.[19] The highest intensity FTIR peaks of GO correspond to the oxygen functional groups. The carbonyl groups (C=O) and double bonds (C=C) of GO are identified by peaks at 1715 and 1550 cm^{-1}, respectively.[20]

In the FTIR spectrum of OamPOSS–GO, the carboxylic peak of GO shifts to a lower frequency, from 1715 to 1700 cm^{-1}. This shift may be due to the donation of electron pairs by the amine groups of OamPOSS to the carbonyl groups on the GO surface.[21] The key peak that confirms the chemical reaction between the amine and acid group is the amide carbonyl peak. The sharp, low-intensity peak at 1650 cm^{-1} indicates the presence of an amide bond. The characteristic peak for the C—O bond of the amide also appeared at 1361 cm^{-1}, further confirming the chemical grafting of OamPOSS to the GO.[4]

A white residue remained after the TGA analysis of the OamPOSS–GO additive. The FTIR spectrum of this residue had an intense peak near 1162 cm^{-1}, consistent with the Si-O-Si stretching vibrations of the silicon cage (vide infra). Thus, the residue is likely from the silica of the POSS. The FTIR spectrum of silica residue is shown in Figure 4.S2 in the Supporting Information.

4.4.3 Thermogravimetric analysis (TGA)

The thermal stability of the OamPOSS–GO was studied using TGA; the thermograms are shown in Figure 4.4. Approximately 60% mass loss of OamPOSS at up to 700 °C corresponds to the thermal decomposition of the organic vertex groups. The remaining 40% of the residue represents the silicon cage.[22] There are three noticeable mass losses in the GO thermogram in the ranges 150–250 °C, 250–450 °C, and 450–650 °C. These mass losses can be assigned to the degradation of functional groups, disordered and amorphous carbon atoms, and the graphite skeleton of GO, respectively. The

2.5% TGA residue of GO can be assigned to the combined residual iron and manganese in the sample probably left over from the oxidation of the graphene.

The OamPOSS–GO thermogram shows a superposition of GO and OamPOSS thermograms. In OamPOSS–GO, the mass loss up to 600 °C can be assigned to the complete degradation of the GO and the organic groups of OamPOSS. The thermal stability of the graphite skeleton increased compared to that of the pure GO. The residue above 700 °C corresponds to the silica cage in POSS. According to the molecular formula of OamPOSS, $(C_3H_9N)_8\ (SiO_{1.5})_8$, (MW= 888 g/mol), the estimated mass fraction of silica ($SiO_{1.5}$) in pure OamPOSS is equal to 34.6%. However, the silica is likely in the form of SiO_2 after reacting with oxygen in the air during the TGA. Therefore, the mass fraction of silica (SiO_2) can be estimated as ~40%, which is in good agreement with the measured value from the TGA residue.

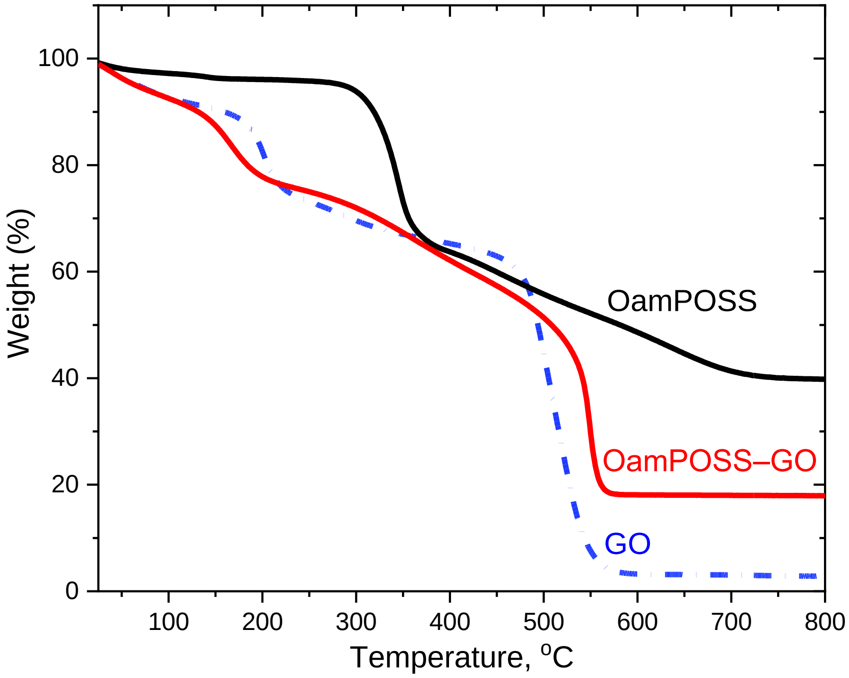

Figure 4.4. The TGA thermograms of the OamPOSS, OamPOSS–GO hybrid material, and GO.

The wt% of OamPOSS in the OamPOSS–GO was estimated using TGA. The mass fraction of silica was estimated from TGA as ~14.2%. After correcting for residual metals from GO (iron and manganese), the %mass of silicon residue (SiO_2) can be estimated as approximately 11.8%. Therefore, the mass percentage of OamPOSS grafted onto the GO in the composite can be calculated as approximately 29.5%.

4.4.4. Elemental analysis

The elemental composition of the OamPOSS–GO material was determined by XRF analysis. The mass percentages of the most abundant atoms are given in Table 4.1. Based on the elemental analysis, the silicon and nitrogen contents of the product were 7.56 and 4.02 wt%, respectively.

Table 4.1. Elemental analysis of OamPOSS–GO additive

Atom	Mass (%)
C	48.4
O	36.7
N	4.02
Si	7.56
Fe	1.52
Mn	0.84

The silicon content determined from the XRF analysis was used as a secondary source to calculate the mass percentage of OamPOSS in the product. Based on the elemental analysis, the %wt of the OamPOSS in the GO was estimated as 30 wt%, in good agreement with the TGA results.

4.4.5. Dispersion analysis in epoxy resin

The study of the dispersion of the additive was performed using a three-roll mill and a speed mixer that were similar to those used in large-scale applications. The dispersion characteristics of the OamPOSS–GO additive in epoxy resin were studied using an optical microscope, and the images are shown in Figure 4.5. GO tends to agglomerate in composites due to the interactions between the graphene sheets. The modification reaction with OamPOSS was expected to reduce the interactions between the GO sheets due to exfoliation and ultimately increase the dispersion in resin. Based on the microscopy, excellent dispersion of 0.1% OamPOSS–GO compared to the other systems with much smaller additive loadings was achieved in the resin without visually recognizable agglomerates.[23,24] However, when the additive loading increased from 0.5% to 1%, the particle attractions dominated and resulted in agglomeration. In Figure 4.5, the two orange circles in the 0.5% and 1% samples are air bubbles trapped after the additive was mixed into the resin. Therefore, the additive-dispersed resins were thoroughly degassed in a speed mixer before they were molded into DMA specimens. In Figure 4.5, the GO agglomerates are responsible for the black dots.

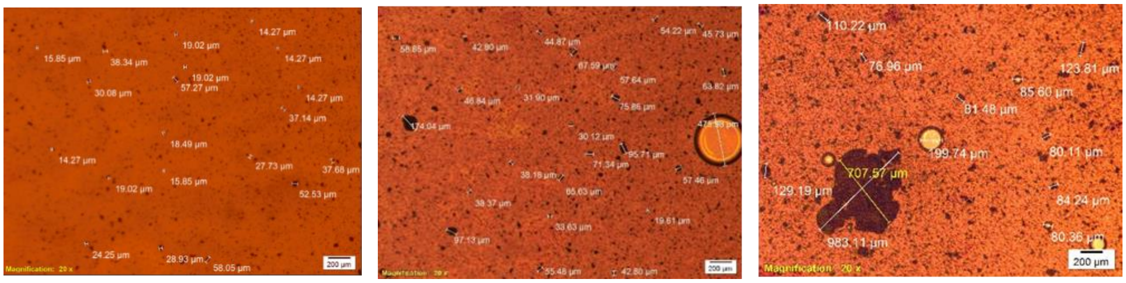

Figure 4.5. Optical microscopy images of a) 0.1%, b) 0.5%, and c) 1% additive dispersed in epoxy resin. The sizes of some of the GO agglomerates are shown in the figures. The scale bars are 200 µm in each image.

The effect of additives on the curing profile and glass transition temperatures of the epoxy resin was studied with DSC. The DSC thermograms of room-temperature cured samples at various post-curing times are shown in Figure 4.6 where the curves are shifted vertically to more easily distinguish the thermal transitions in different samples.

The neat epoxy sample shows a glass transition temperature (T_g) centered at 65 °C. The 1% OamPOSS–GO additive-loaded sample showed a 4 °C decrease, appearing at 62 °C. This decrease likely indicates the reduced crosslinking density of the additive-loaded sample compared to the neat resin. During this study, 80 °C was selected as the post-curing temperature based on the specification provided by the manufacturer. The differences in T_g s between the neat and additive-loaded samples can be seen after up to 1 h of post-curing, where the difference of the T_g of the OamPOSS–GO sample was approximately 4 °C below that of the neat resin. However, after post-curing treatment at 80 °C, the T_g of the neat and composite samples were similar. This suggests that the post-curing treatment has efficiently crosslinked and cured both neat and additive-loaded samples. The changes in T_g with different post-curing times were used as a reference point for the optimum time for the post-curing process and the time in which the maximum T_g was achieved. Based on the results shown in Figure 4.6, the sample specimens were post-cured at 80 °C for 6 h before the DMA tests.

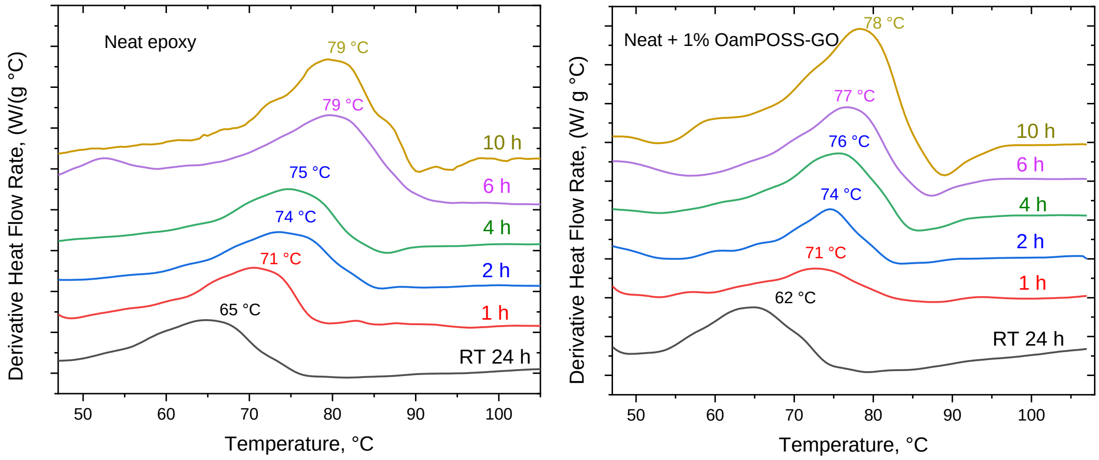

Figure 4.6. The TMDSC thermograms of a) neat EP 828 and b) 1% OamPOSS–GO composite at 80 °C with variable times. The temperatures listed are the maxima of the T_g peaks

The data is reported above 45 °C because there was a thermal signal around 40 °C due to instrumental startup transient response. The full thermograms are shown in Figure 4.S3 in the Supporting Information.

4.4.7. Dynamic mechanical analysis (DMA)

The effect of adding OamPOSS–GO on the viscoelastic properties of epoxy resin was evaluated by DMA. The variation in the storage modulus (G'), loss modulus(G"), and tan δ of the epoxy resin with and without the OamPOSS–GO additive is shown in Figure 4.7. G' provides information on the elastic behavior of the material, which represents the ability to store and return the energy. Plotting G' vs. temperature shows three different regions (glassy, glass transition, and rubbery) for the epoxy resins.

Starting from room temperature, G' decreased with increasing temperature due to the increasing motion of the polymer molecules. The additive-loaded samples showed significantly larger G' at room temperature than the neat epoxy and increased with additive loading. A small loading of OamPOSS–GO as 0.1% increased the G' by approximately 6.5%. With larger additive loadings of 0.5, 1, and 2, the samples showed 14, 21, and 39% increased G' compared to the neat epoxy. During the DMA experiments, the specimens were heated to 150 °C at a frequency of 1 Hz. The neat epoxy specimens failed by the end of the experiment, while the additive-loaded samples remained intact after the experiment was completed. This result suggests the additive imparted larger flexibility and strength to the resin. In addition, the curves were broader in the OamPOSS–GO-loaded samples, suggesting that they have a larger crosslinking density than the neat epoxy.

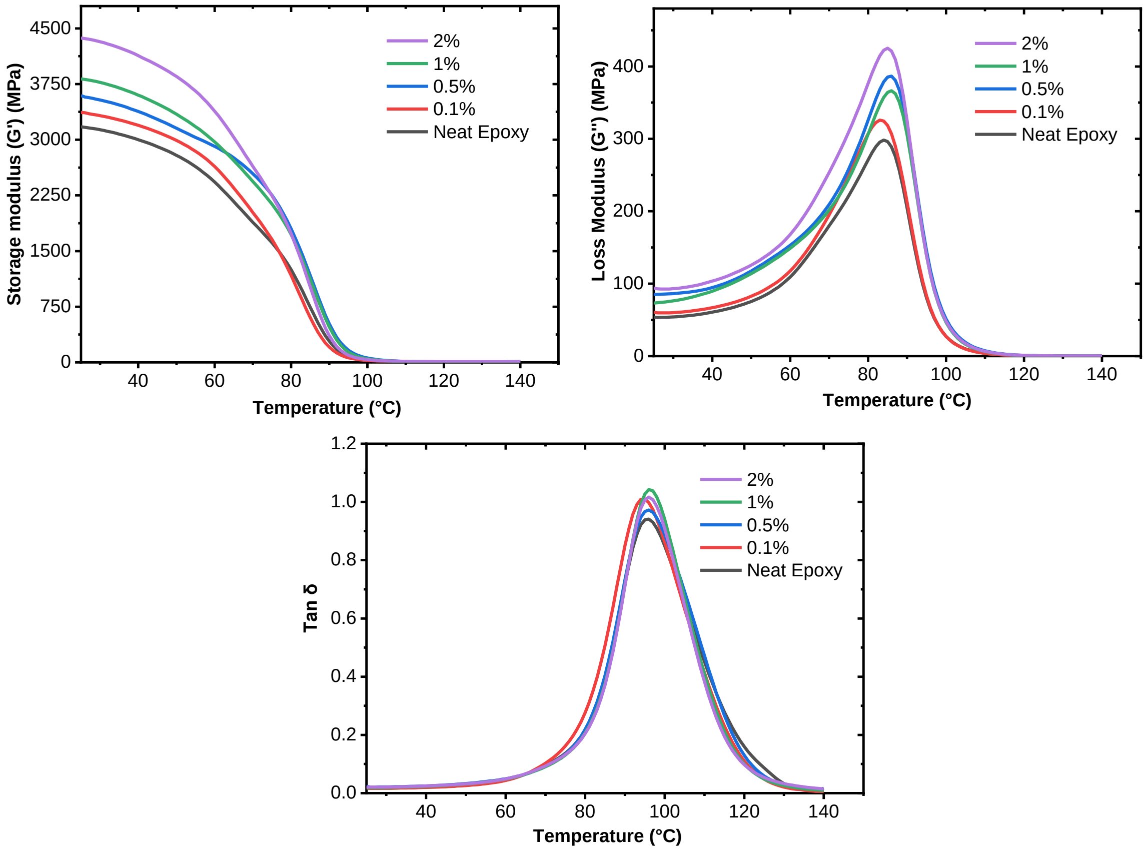

Figure 4.7. The variation in a) storage modulus, G', b) loss modulus, G", and c) tan δ of neat epoxy and OamPOSS–GO/epoxy with 0.1%, 0.5%, 1%, and 2% additive loading at 30 °C at 1 Hz.

The loss modulus (G") provides information on viscous behavior and the material's ability to lose or dissipate energy.[25] The G" of the neat epoxy was 84 MPa, and that of the OamPOSS–GO composites increased with increased additive loading. In the OamPOSS–GO composites, the 0.1, 0.5, 1, and 2% samples show G" increasing by 13, 37, 60, and 60%, respectively.

The peak of the tan δ curve may be used as the mechanical (1 Hz) glass transition temperature (T_g) of the sample, which is useful for comparison with the neat sample. The slight increase of T_g compared to that of the neat epoxy sample suggests an interaction between the additive and the resin. Selected mechanical results are shown in Figure 4.1. The G and G values are listed for 30 °C, which is typical operating temperature for many composites.

Table 4.1. DMA results obtained for neat and OamPOSS–GO epoxy systems

Additive amount	Storage modulus (G') at 30 °C, (MPa)	Loss modulus (G") at 30 °C, (MPa)	Temperature at maximum tan δ *(T_g.°C)*
Neat epoxy	3150 ± 45	53 ± 3	94 ± 1
0.1%	3366 ± 60	60 ± 5	94 ± 1
0.5%	3594 ± 40	73 ± 2	95 ± 2
1%	3819 ± 70	85 ± 6	97 ± 1
2%	4369 ± 47	84 ± 4	97 ± 2

The mechanical properties of monolayers of GO are well established.[5] For example, the impact strength of monolayer GO is reported as 42 Nm^{-1}, Young's modulus as 1 TPa, and intrinsic tensile strength as 130 GPa.[5] GO has also been tested as an additive and filler for polymers without modifications with organic molecules.[25] The dynamic mechanical properties of GO-loaded epoxy resins showed scattered data for the moduli. Compared with neat epoxy, a similar storage modulus (at 30 °C) was obtained for small additive loadings, such as 0.1%. However, a detrimental effect on the mechanical properties was observed when the additive loading was increased beyond 0.5%. This decrease may be due to the poorer dispersion of GO sheets in the epoxy medium.

The dispersion of GO in epoxy resin is one of the most important factors that ultimately determine the mechanical properties of the resin.[3,25] The powdered form of GO is a hard rock-type material that requires mechanical grinding, strong ultrasonication, or dispersion in solvents before the dispersion in resin. The ultrasonication of additive-loaded epoxy resin has several drawbacks. (1) The heat generated during the sonication can degrade the epoxy resin. (2) The heat also promotes the ring opening of epoxides that reduce the crosslinking density during the curing step. As a result, both the thermal and mechanical properties of the resin can be compromised. In an alternative method, the dried GO power can be dispersed in solvents such as tetrahydrofuran and acetone. Then the dispersion is mixed with epoxy resin using a shear mixer and thoroughly degassed to remove the solvent. The disadvantages of applying this method to large-scale applications are: 1) the use of a large amount of solvent 2) the use of sonication 3) freeze drying, and 4) constraints in degassing and evaporating the solvent after dispersion.[7,18,25,26] The thermal degradation of functional groups of GO is also a major barrier when using GO for high-temperature applications. In general, the functional groups of GO degrade in the temperature range of 150–220 °C. Therefore, the applications of GO-filled resins should be limited to low-temperature applications.

The modification of GO using OamPOSS has been carried out to improve the dispersion, thermal stability, and mechanical properties of the polymers. In a similar work to this report, the OamPOSS–GO has been tested as an additive for polyurethane and epoxy-thin films.[27] In polyurethane, even small loadings of additive, such as 0.2 wt%, have been shown to increase the tensile strength[27] by as much as 152%. The grafting of OamPOSS to GO resulted in the exfoliation of graphene sheets from 1 to 8 nm thick, which contributed to the extraordinary performance of the additive in the resin. The OamPOSS–GO hybrid material has also been tested as a potential additive to promote the corrosion resistance of epoxy thin films.[27] Those results suggested that the grafting reaction increased GO dispersion in organic solvents and reduced the dielectric constant and dielectric loss of the epoxy resin.[4] The OamPOSS–GO hybrid material has been tested as a potential interfacial modifier for epoxy matrix and carbon fibers.[18] The interfacial strength of carbon fiber composites increased by 53% compared to the GO-functionalized carbon fibers. In this report, the OamPOSS-GO material has a fluffy appearance that showed efficient dispersion in epoxy resin without solvents. The OamPOSS-GO additive synthesized in this method requires only a three-roll mill to disperse the additive and make a master batch. The masterbatch can be diluted with appropriate amounts of resin to get dispersions (0.1, 0.5, 1, and 2%). With the results reported here, the OamPOSS–GO material has shown efficient dispersion in epoxy resin and has the potential to be used as an additive for the epoxy resin to increase mechanical properties with small additive loadings.

4.5. CONCLUSIONS

This report describes the work done on chemical synthesis, characterization, and evaluation of mechanical properties of OamPOSS-modified GO to epoxy resins. The grafting of OamPOSS to GO was performed in an aqueous medium using an economical method that can be scaled to industrial requirements. FTIR spectroscopy was used to characterize the amide bond formed between the OamPOSS and the GO after the grafting reaction, and the mass percentage of OamPOSS in the composite was estimated as approximately 34 wt%, based on elemental analysis. The thermal characterization of the OamPOSS-GO and the composites was conducted with TGA and DSC. The DSC results showed that the additive affected the glass transition behavior of epoxy curing at room temperature; however, there was no significant effect on the glass transition of additive-loaded samples after the post-curing at 80 °C. TGA analysis showed that the incorporation of additives maintained the thermal stability of epoxy resin which is a promising observation. The dispersion characteristics of OamPOSS-GO were evaluated by using a series of solvents such as water, ethanol, tetrahydrofuran, pentane, etc. It was observed that the OamPOSS-GO showed increased dispersion in hydrophobic solutions, such as toluene and pentane compared to GO. Therefore, this additive is expected to show efficient dispersion and improve the mechanical properties of hydrophobic and moderately hydrophobic resins such as epoxies. The mechanical properties of the OamPOSS-GO-filled EPON 862 epoxy resin were evaluated by DMA analysis. The flexural moduli of the neat epoxy and the additive-loaded epoxy were measured with different additive loadings such as 0.1, 0.5, 1, and 2%. It was observed that the OamPOSS–GO additive increased the storage modulus and loss modulus significantly compared to those of neat epoxy. The loss modulus of the 1% and 2% additive-loaded samples increased by 60%, and the storage modulus increased by 39% compared to the neat epoxy sample at 30 °C. The OamPOSS–GO materials are a strong candidate for new multifunctional applications.

4.6. ACKNOWLEDGEMENTS

The authors acknowledge the financial support and testing facility provided by MITO Materials Solutions under grants from the Center for the Advancement of Science & Technology (OCAST) (Award No. AR19-011-2 and sub-award No 7003-AR11-02). Frank D. Blum acknowledges the financial support of the H.I. Bartlett Endowment.

4.7. REFERENCES

1. Gill, F. S.; Uniyal, D.; Prasad, B.; Saluja, S.; Mishra, A.; Bachheti, R. K.; Juyal, S., Investigation of increased electrical conductivity by rGO in rGO/PVDF/PMMA/PTFE nanocomposites. *Journal of Molecular Structure* **2022,** *1267*, 133541.

2. Xue, Y.; Liu, Y.; Lu, F.; Qu, J.; Chen, H.; Dai, L., Functionalization of graphene oxide with polyhedral oligomeric silsesquioxane (POSS) for multifunctional applications. *Journal of Physical Chemistry Letters* **2012,** *3* (12), 1607-12.

3. Tang, J.; Zhou, H.; Liang, Y.; Shi, X.; Yang, X.; Zhang, J., Properties of graphene oxide/epoxy resin composites. *Journal of Nanomaterials* **2014,** *2014*, 1-5.

4. Yu, W.; Fu, J.; Dong, X.; Chen, L.; Shi, L., A graphene hybrid material functionalized with POSS: synthesis and applications in low-dielectric epoxy composites. *Composites Science and Technology* **2014,** *92*, 112-119.

5. Smith, A. T.; LaChance, A. M.; Zeng, S.; Liu, B.; Sun, L., Synthesis, properties, and applications of graphene oxide/reduced graphene oxide and their nanocomposites. *Nano Materials Science* **2019,** *1* (1), 31-47.

6. Shi, Y.; Yu, B.; Zheng, Y.; Yang, J.; Duan, Z.; Hu, Y., Design of reduced graphene oxide decorated with DOPO-phosphanomidate for enhanced fire safety of epoxy resin. *Journal of Colloid and Interface Science* **2018,** *521*, 160-171.

7. Li, W.; Huang, W.; Kang, Y.; Gong, Y.; Ying, Y.; Yu, J.; Zheng, J.; Qiao, L.; Che, S., Fabrication and investigations of G-POSS/cyanate ester resin composites reinforced by silane-treated silica fibers. *Composites Science and Technology* **2019,** *173*, 7-14.

8. Jiang, D.; Xing, L.; Liu, L.; Yan, X.; Guo, J.; Zhang, X.; Zhang, Q.; Wu, Z.; Zhao, F.; Huang, Y.; Wei, S.; Guo, Z., Interfacially reinforced unsaturated polyester composites by chemically grafting different functional POSS onto carbon fibers. *Journal of Materials Chemistry A* **2014,** *2* (43), 18293-18303.

9. Raimondo, M.; Guadagno, L.; Speranza, V.; Bonnaud, L.; Dubois, P.; Lafdi, K., Multifunctional graphene/POSS epoxy resin tailored for aircraft lightning strike protection. *Composites Part B: Engineering* **2018,** *140*, 44-56.

10. Yadav, S. K.; Mahapatra, S. S.; Yoo, H. J.; Cho, J. W., Synthesis of multi-walled carbon nanotube/polyhedral oligomeric silsesquioxane nanohybrid by utilizing click chemistry. *Nanoscale Research Letters* **2011,** *6* (1), 122.

11. Zhang, M.; Yan, H.; Yuan, L.; Liu, C., Effect of functionalized graphene oxide with hyperbranched POSS polymer on mechanical and dielectric properties of cyanate ester composites. *Royal Society of Chemistry Advances* **2016,** *6* (45), 38887-38896.

12. Zhang, R. L.; Gao, B.; Du, W. T.; Zhang, J.; Cui, H. Z.; Liu, L.; Ma, Q. H.; Wang, C. G.; Li, F. H., Enhanced mechanical properties of multiscale carbon fiber/epoxy composites by fiber surface treatment with graphene oxide/polyhedral oligomeric silsesquioxane. *Composites Part A: Applied Science and Manufacturing* **2016,** *84*, 455-463.

13. Tang, C.; Yan, H.; Li, S.; Li, M.; Chen, Z., Novel phosphorus-containing polyhedral oligomeric silsesquioxane functionalized Graphene oxide: preparation and its performance on the mechanical and flame-retardant properties of bismaleimide composite. *Journal of Polymer Research* **2017,** *24* (10).

14. Ye, Y.; Zhang, D.; Liu, T.; Liu, Z.; Liu, W.; Pu, J.; Chen, H.; Zhao, H.; Li, X., Improvement of anticorrosion ability of epoxy matrix in simulate marine environment by filled with superhydrophobic POSS-GO nanosheets. *Journal Hazard Materials* **2019,** *364*, 244-255.

15. Ghani, K.; Kiomarsipour, N.; Ranjbar, M., New high-efficiency protective coating containing glycidyl-POSS nanocage for improvement of solar cell electrical parameters. *Journal of Nanostructures* **2019,** *9* (1), 103-111.

16. Rahman, M. M.; Filiz, V.; Khan, M. M.; Gacal, B. N.; Abetz, V., Functionalization of POSS nanoparticles and fabrication of block copolymer nanocomposite membranes for CO_2 separation. *Reactive and Functional Polymers* **2015,** *86*, 125-133.

17. Arslan, I.; Tasdelen, M. A., POSS-based hybrid thermosets via photoinduced copper-catalyzed azide–alkyne cycloaddition click chemistry. *Designed Monomers and Polymers* **2016,** *19* (2), 155-160.

18. Zhang, X.; Ma, R.; Du, A.; Liu, Q.; Fan, Y.; Zhao, X.; Wu, J.; Cao, X., Corrosion resistance of organic coating based on polyhedral oligomeric silsesquioxane-functionalized graphene oxide. *Applied Surface Science* **2019,** *484*, 814-824.

19. Vijayakumar, V.; Son, T. Y.; Kim, H. J.; Nam, S. Y., A facile approach to fabricate poly(2,6-dimethyl-1,4-phenylene oxide) based anion exchange membranes with extended alkaline stability and ion conductivity for fuel cell applications. *Journal of Membrane Science* **2019,** *591*, 1-11.

20. Rattana; Chaiyakun, S.; Witit-anun, N.; Nuntawong, N.; Chindaudom, P.; Oaew, S.; Kedkeaw, C.; Limsuwan, P., Preparation and characterization of graphene oxide nanosheets. *Procedia Engineering* **2012,** *32*, 759-764.

21. Chen, S.; Cheng, B.; Ding, C., Synthesis and characterization of Poly(vinyl pyrrolidone)/Reduced graphene oxide nanocomposite. *Journal of Macromolecular Science, Part B* **2015,** *54* (4), 481-491.

22. Liao, W. H.; Yang, S. Y.; Hsiao, S. T.; Wang, Y. S.; Li, S. M.; Ma, C. C.; Tien, H. W.; Zeng, S. J., Effect of octa(aminophenyl) polyhedral oligomeric silsesquioxane functionalized graphene oxide on the mechanical and dielectric properties of polyimide composites. *ACS Applied Material Interfaces* **2014,** *6* (18), 15802-12.

23. Kranauskaitė, I.; Macutkevič, J.; Borisova, A.; Martone, A.; Zarrelli, M.; Selskis, A.; Aniskevich, A.; Banys, J., Enhancing electrical conductivity of multiwalled carbon nanotube/epoxy composites by graphene nanoplatelets. *Lithuanian Journal of Physics* **2018,** *57* (4), 232-242.

24. Force Tefo, T.; Moloto, M. J.; Nyangiwe, N.; Khenfouch, M.; Maaza, M.; Kotsedi, L.; Dikio, E., Synthesis and Characterization of Graphene Thin Films via Hummer's Method. 2012.

25. Aradhana, R.; Mohanty, S.; Nayak, S. K., Comparison of mechanical, electrical and thermal properties in graphene oxide and reduced graphene oxide filled epoxy nanocomposite adhesives. *Polymer* **2018,** *141*, 109-123.

26. Xue, G.; Zhang, B.; Xing, J.; Sun, M.; Zhang, X.; Li, J.; Wang, L.; Liu, C., A facile approach to synthesize in situ functionalized graphene oxide/epoxy resin nanocomposites: mechanical and thermal properties. *Journal of Materials Science* **2019,** *54* (22), 13973-13989.

27. Hu, L.; Jiang, P.; Bian, G.; Huang, M.; Haryono, A.; Zhang, P.; Bao, Y.; Xia, J., Effect of octa(aminopropyl) polyhedral oligomeric silsesquioxane (OapPOSS) functionalized graphene oxide on the mechanical, thermal, and hydrophobic properties of waterborne polyurethane composites. *Journal of Applied Polymer Science* **2017,** *134* (6), 1-11.

4.8. SUPPORTING INFORMATION

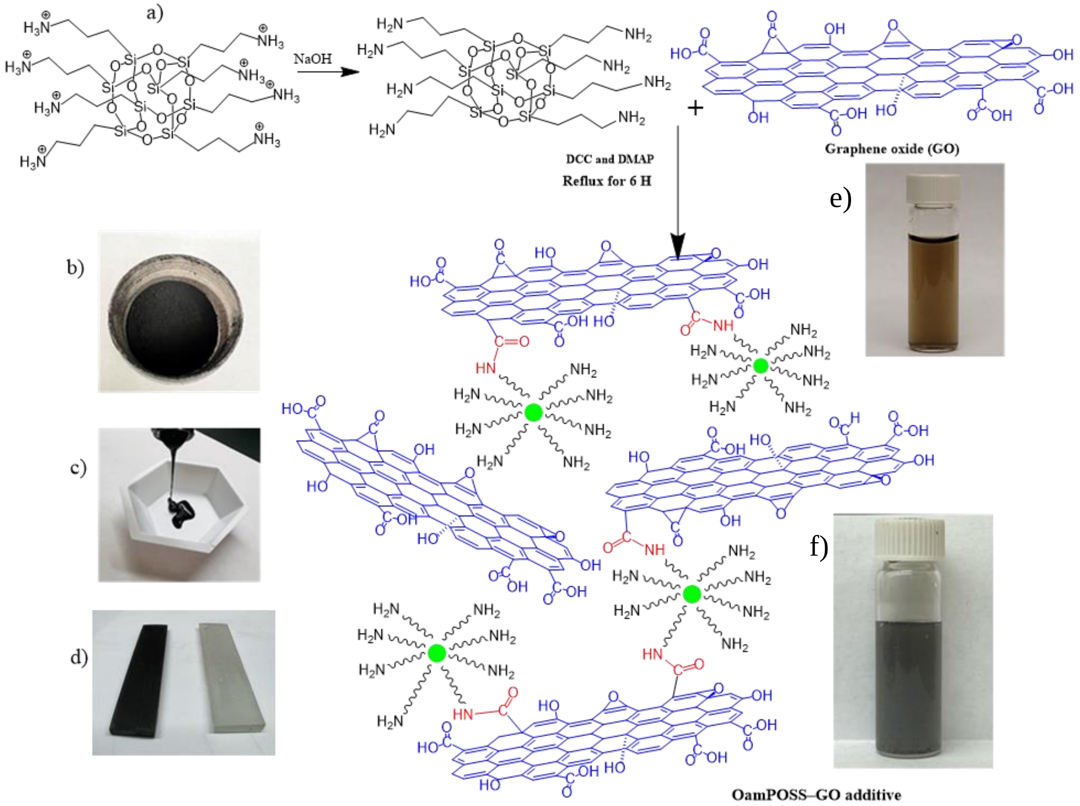

CONTENTS

4.S1. Full FTIR spectra of GO, OamPOSS, and OamPOSS-GO.

4.S2. FTIR spectrum of TGA residue obtained after the TGA experiment.

4.S3. X-Ray Fluorescence data was obtained for the OamPOSS-GO.

4.S1. FULL FTIR SPECTRA OF GO, OAMPOSS AND OAMPOSS-GO

FTIR spectra of GO, OamPOSS, and OamPOSS-GO were collected in the range of 500-4000 cm^{-1}. The most important FTIR peaks of each material were found in the range of 1000-2000 cm^{-1}. Therefore, partial FTIR spectra of each material were shown in the paper and the full spectra are shown in Figure S1. The broad peak in the range of 3600 to 3000 cm^{-1} in GO and OamPOSS was due to O–H stretching and the broad peak at 2800 cm^{-1} is due to the C–H bonds.

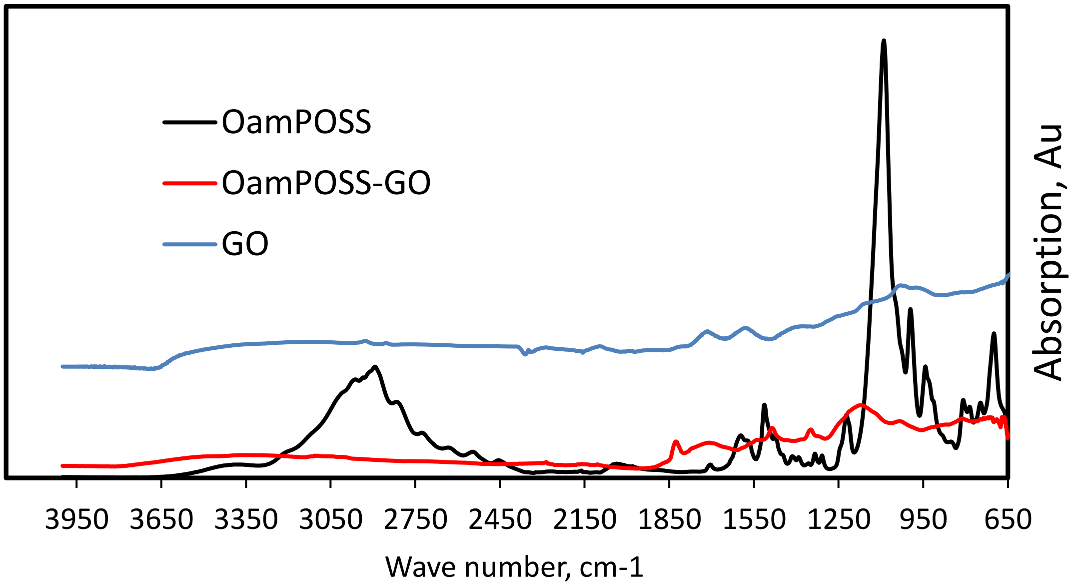

Figure 4.S1. Full FTIR spectra of OamPOSS, OamPOSS-GO and GO.

4.S2. FTIR SPECTRUM OF TGA RESIDUE OBTAINED AFTER THE TGA EXPERIMENT

An important observation of OamPOSS is the higher stability of silica residue at temperatures as high as 850 °C. After heating the material to 850 °C, a white residue was observed in the TGA pan expected to be in the form of silica from the OamPOSS cage. The FTIR spectrum of the white residue was carried out to identify the chemical identity of the material as shown in Figure 4.S2. The peak at 1088 cm^{-1} and the broad peak centered at 3300 cm^{-1} is due to the Si–O stretching of the silica residue and silanol groups, respectively.

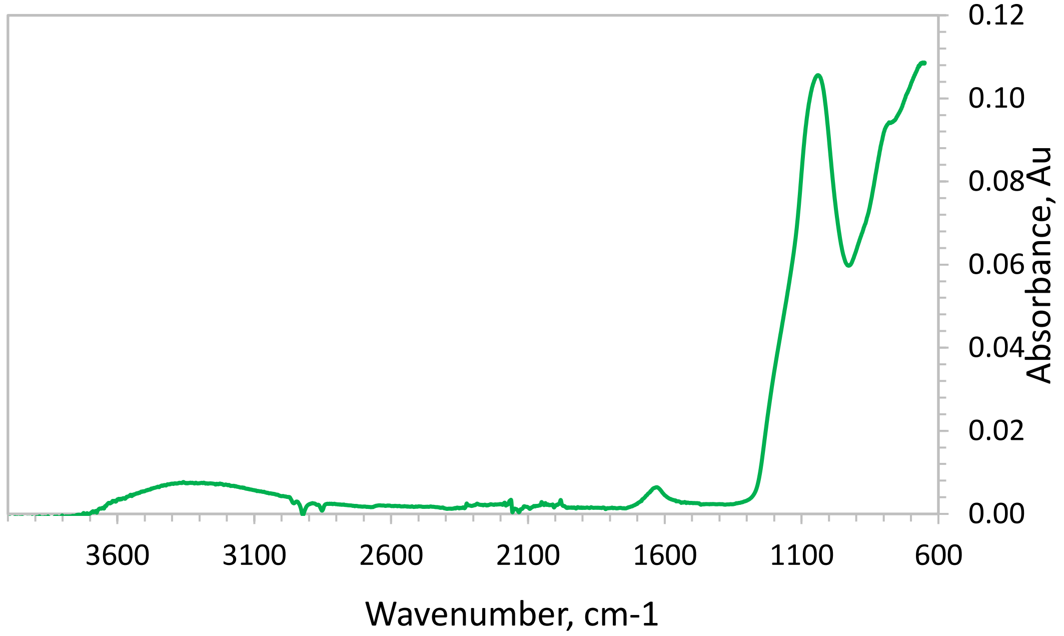

Figure 4.S2. FTIR spectrum of TGA residue for the OamPOSS-GO additive.

4.S3. X-Ray Fluorescence data obtained for the OamPOSS-GO

The chemical composition of synthesized OamPOSS-GO was carried out by XRF analysis. The full results are shown in Table 4.S3.

Table 4.S3. The tabulation of the elemental composition of OamPOSS-GO

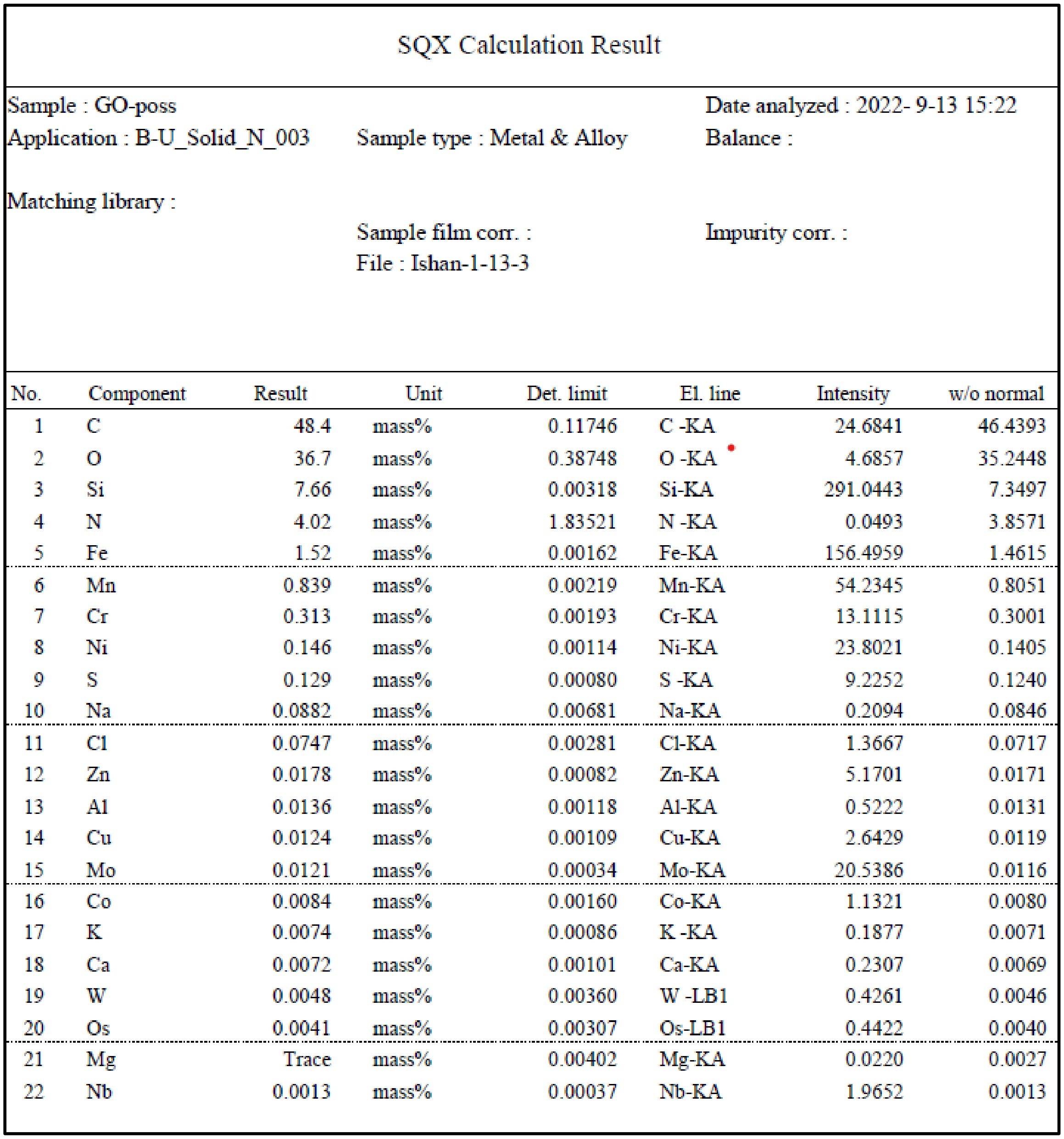

SQX Calculation Result

Sample : GO-poss
Date analyzed : 2022- 9-13 15:22
Application : B-U_Solid_N_003
Sample type : Metal & Alloy
Balance :

Matching library :
Sample film corr. :
Impurity corr. :
File : Ishan-1-13-3

No.	Component	Result	Unit	Det. limit	El. line	Intensity	w/o normal
1	C	48.4	mass%	0.11746	C -KA	24.6841	46.4393
2	O	36.7	mass%	0.38748	O -KA	4.6857	35.2448
3	Si	7.66	mass%	0.00318	Si-KA	291.0443	7.3497
4	N	4.02	mass%	1.83521	N -KA	0.0493	3.8571
5	Fe	1.52	mass%	0.00162	Fe-KA	156.4959	1.4615
6	Mn	0.839	mass%	0.00219	Mn-KA	54.2345	0.8051
7	Cr	0.313	mass%	0.00193	Cr-KA	13.1115	0.3001
8	Ni	0.146	mass%	0.00114	Ni-KA	23.8021	0.1405
9	S	0.129	mass%	0.00080	S -KA	9.2252	0.1240
10	Na	0.0882	mass%	0.00681	Na-KA	0.2094	0.0846
11	Cl	0.0747	mass%	0.00281	Cl-KA	1.3667	0.0717
12	Zn	0.0178	mass%	0.00082	Zn-KA	5.1701	0.0171
13	Al	0.0136	mass%	0.00118	Al-KA	0.5222	0.0131
14	Cu	0.0124	mass%	0.00109	Cu-KA	2.6429	0.0119
15	Mo	0.0121	mass%	0.00034	Mo-KA	20.5386	0.0116
16	Co	0.0084	mass%	0.00160	Co-KA	1.1321	0.0080
17	K	0.0074	mass%	0.00086	K -KA	0.1877	0.0071
18	Ca	0.0072	mass%	0.00101	Ca-KA	0.2307	0.0069
19	W	0.0048	mass%	0.00360	W -LB1	0.4261	0.0046
20	Os	0.0041	mass%	0.00307	Os-LB1	0.4422	0.0040
21	Mg	Trace	mass%	0.00402	Mg-KA	0.0220	0.0027
22	Nb	0.0013	mass%	0.00037	Nb-KA	1.9652	0.0013

CHAPTER V

THERMAL BEHAVIOR OF POLYVINYLPYRROLIDONE ON REDUCED GRAPHENE OXIDE

Ishan N. Jayalath,[a] Ranji Vaidyanathan,[b] Frank D. Blum[a] *

[a] Department of Chemistry, Oklahoma State University, Stillwater, OK 74078 USA

[b] School of Materials Science and Engineering, Oklahoma State University, Tulsa, OK 74106 USA

.

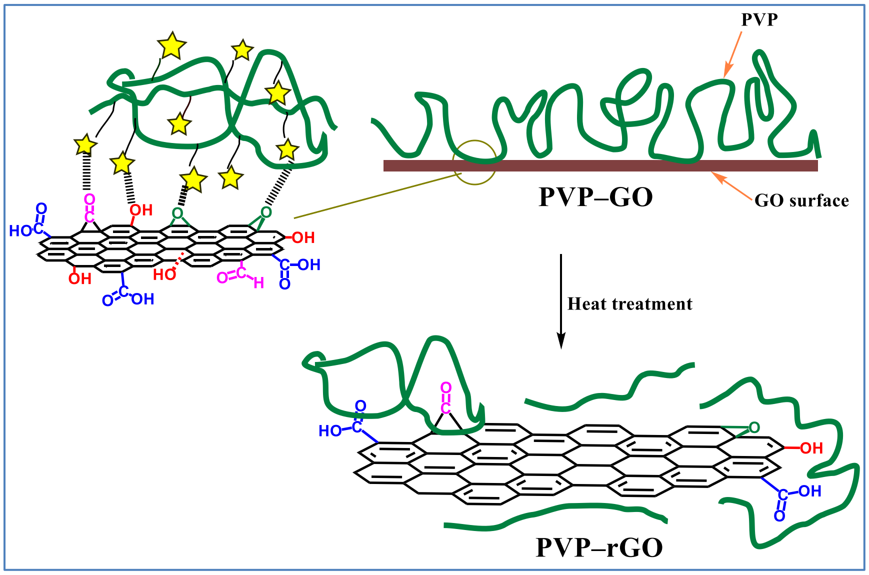

5.1. ABSTRACT

Temperature-modulated differential scanning calorimetry (TMDSC) and Fourier transform infrared (FTIR) spectroscopy were used to study the interfacial behavior of polyvinyl pyrrolidone (PVP) on reduced graphene oxide (rGO). In this study, rGO was selected as the substrate due to its good thermal stability around the glass transition temperature of bulk PVP (176 °C). Based on FTIR, it was found that PVP molecules cover some of the residual functional groups of the rGO surface and hydrogen bonding occurs. The hydrogen bonding interaction produces *tightly-bound* PVP on the rGO surface. The thermal signature of the *tightly–bound* segments of PVP on the rGO was not directly apparent in the TMDSC thermograms of the composite samples. Therefore, an analysis was carried out to indirectly estimate the amount of *tightly-bound* PVP on the rGO from the "missing" PVP signal. The linear regression of the data fitted to the model provided an estimate of the amount of *tightly–bound* PVP on the rGO surface as 0.84 ± 0.03 (SD) mg/m^2. Above this *tightly–bound* amount, the bound fractions decreased with increased adsorbed amounts, consistent with the model. This result was also consistent with the previously reported hydrogen–bonded systems where the signature of a tightly-bound polymer was observed, and the tightly-bound amount was on the 1 nm length scale.

5.2. INTRODUCTION

Polymer composites have attracted the attention of scientists and engineers due to their unique characteristics.[1,2] In many composites, inorganic additives provide a solid surface that facilitates interactions such as dipole-dipole, H–bonding, or ionic interactions with the polymer molecules. As a result of these interactions, the thermal behavior of polymer segments near a solid surface can change significantly compared to its bulk state.[3,4] This effect can be highly dramatic when using nanoscale additives such as graphene oxide (GO), which has a large surface area.[5-7] GO suffers from thermal degradation of the oxygenated functional groups below 200 °C, which is a major obstacle when making GO–based composites for high–temperature applications. To overcome the potential problems with GO degradation, GO can be treated at elevated temperatures to produce reduced graphene oxide (rGO), which is a more thermally stable alternative for GO. rGO has been used in different applications such as conductive materials,[8] coatings,[9] and fiber–reinforced composites.[10]

Polyvinyl pyrrolidone (PVP) can be used in composites with rGO resulting in improved mechanical, thermal, and electrical properties compared to bulk PVP.[11-13] In composites, the properties of PVP show different chemical and thermal characteristics due to the interaction of functional groups of PVP with the solid surface of the nanofiller. The carbonyl groups of PVP play a role in determining the strength and the type of interaction with the nanofiller.[5,14] As a result of restrictions of the PVP segments on the surface, the glass transition temperature (T_g) of some parts of the polymer in the composites may be elevated compared to bulk PVP.[13] The effect of the polymer–surface interactions can be probed using the thermal activity of the polymer in the glass transition region. However, to the best of our knowledge, not much attention has been given to the characterization of the interphase of PVP and rGO in its composites (PVP–rGO).

The understanding of the interface between the polymer and rGO is crucial when designing high-performance composites where additives behave as interfacial modifiers. Different arrangements and types of interactions that take place between the polymer and the rGO are important and determine the overall properties of the composite. The polymer molecules on the rGO surface can be interpreted using the loop–train–tail model and based on this can be divided into three different types of segments.[15,16] The polymer segments closest to the surface are called trains and have direct interactions with the surface. When the interactions are attractive with the solid surface, these segments show reduced mobility and may have different thermal signatures compared to the bulk polymer. The polymer segments away from the surface are called loops; these are connected to the trains. However, they reside further away from the surface. The polymer segments that are near the chain ends are called tails, which can behave differently depending on the nature of the chain ends. Alternatively, the behavior of polymer on the rGO surface can be further simplified using a two-state model in which, the polymer adsorbed on rGO may be considered as a combination of two different types based on polymer mobility as inferred from the position of the glass transition. If a significant interaction between filler/substrate and polymer takes place, such as hydrogen bonding, in which the glass transition is elevated from the bulk value. These segments that are closer to the solid surface may be considered "*tightly-bound*". The polymer segments further away from the solid surface can be considered as "*loosely bound*" often similar to the bulk polymer,[17] in which the glass transition is similar to that of the bulk polymer. Based on the two-state model, the bound fraction of polymer on the host surface, in some cases, can be estimated using the area under the heat flow curves of the *tightly–bound* fraction in the TMDSC thermograms if both fractions show distinct transitions.

In conventional composites, it is challenging to study the interface between the polymer and the reinforcement, where additive loadings can be significantly less than the amount of polymer. For example, if the weight ratio of GO to polymer was 1:99, in such extremely small amounts of additive, the TMDSC signal is indicative of the properties of the bulk polymer. This effect would likely conceal possible transitions of the polymer segments closer to the solid surface. To highlight this behavior of the adsorbed polymer, composites were made with an extremely small amount of polymer, in which the polymer makes an equivalent thin layer (on the range of nanometers) on the rGO surface. The amounts of polymer in the samples are expressed as the mass of polymer per surface of rGO surface (mg of PVP per m^2 of rGO). This is referred to as the adsorbed amount (AA). Assuming the density of the polymer was approximately 1 g/cm^3, a 1 mg/m^2 adsorbed amount sample represents a 1 nm thickness of polymer on the rGO surface, to put a rough distance scale on it.

In this study, we have used FTIR spectroscopy to verify the hydrogen bonding and TMDSC to estimate the *tightly–bound* fraction of PVP on the rGO surface. The aim was to characterize the amount of tightly bound polymer based on a two-state model using TMDSC data without the benefit of a separate peak for the tightly bound polymer. A model was developed to estimate the amount of tightly bound PVP on the rGO surface by estimating the *missing amount* of polymer using a change in the specific heat capacity of PVP in the composite based on the heat capacity of the adsorbed polymer.

5.3. MATERIALS AND METHODS

5.3.1. Materials

The materials used in this experiment were: commercial PVP (K30), M_w approximately 40,000 Da reported by the manufacturer, GAF Material Corporation. (Parsippany-Troy Hills, NJ, USA). The graphite powder was purchased from Sigma Aldrich. Sodium nitrate ($NaNO_3$, 99%), potassium permanganate ($KMnO_4$), hydrogen peroxide (H_2O_2, 30%), and sulfuric acid (H_2SO_4, 98%) were purchased from Thermo-Fisher Scientific (Waltham, Massachusetts, USA). These materials were used directly without any further purification, modification, or other treatments.

5.3.2. Synthesis of GO

Graphene oxide was synthesized by the modified Hummers method.[5] Briefly, graphene powder (2.0 g) and sodium nitrate (2.0 g) were mixed with 50 mL of sulfuric acid in a 500 mL round-bottom flask. Then 6.0 g of $KMnO_4$ was added to the mixture while the temperature was maintained between 0 and 10 °C. The mixture was stirred overnight, and then 300 mL of distilled water was added. Finally, the mixture was treated with 10 mL of H_2O_2, washed twice with 10% HCl, and five times with distilled water.

5.3.3. Preparation of the PVP/GO composites

Different amounts of PVP were dissolved in 95% ethanol in different test tubes. Then 5 mL of graphene oxide (5 mg/mL) dispersed in 95% ethanol was added to each test tube. Adsorption of the polymer on the GO surface was carried out by shaking the test tubes in a mechanical shaker for 48 h. The resulting samples were dried by bubbling air through them overnight. Finally, the samples were dried in a vacuum oven at 80 °C for two days before carrying out the heat treatment, FTIR spectroscopy, thermogravimetric analysis (TGA), and TMDSC.

5.3.4. Preparation of PVP–rGO composites

The dried PVP–GO composites were thermally treated to make PVP–rGO composites.[18] Briefly, a furnace was preheated to 300 °C, and PVP–GO composites were placed in the furnace for 15 min to obtain PVP–rGO samples. Then PVP–rGO composites were stored in a desiccator before carrying out FTIR, TGA, and TMDSC analyses.

5.3.5. Thermal analyses

The compositions of PVP in the PVP–rGO were measured using a Model 2950 Thermogravimetric Analyzer (TA Instruments). Briefly, a portion (approximately 10 mg) of the composite was heated from 25 to 900 °C at a rate of 20 °C/min in air. Heat capacity and heat flow measurements were made using Model Q 2000 Differential Scanning Calorimeter (TA Instruments). Tzero pans (TA Instruments) were used as both sample and reference pans, and the DSC cell was purged with nitrogen gas at a flow rate of 50 mL/min. The sample was equilibrated at 80 °C for 60 min, heated up to 270 °C at a 3 °C/min heating rate with a modulation amplitude of ± 1 °C and a period of 60 s, held for 2 min, cooled to 25 °C at the same rate, and finally held at 25 °C for 2 min.

5.3.6 FTIR spectroscopy

Attenuated total reflection (ATR)–Fourier transformed infrared (FTIR) spectra were recorded using a Nicolet i550 spectrometer (Thermo-Scientific, Waltham, Massachusetts, USA) equipped with an ATR crystal. The spectra were collected from 500–4500 cm^{-1}, with a spectral resolution of 4 cm^{-1}, 64 scans, and automatic atmospheric suppression.

5.4. RESULTS AND DISCUSSION

The partial FTIR spectra (1300–1900 cm^{-1}) of PVP–GO and PVP–rGO composites are shown in Figure 5.1. The spectra of bulk PVP, GO, and rGO is also shown for comparison. The FTIR spectrum of GO in Figure 5.1A shows two characteristic peaks in 1715 and 1581 cm^{-1} that can be attributed to the stretching vibrations of C=O and C=C.[19-24] The full spectra are given in Supporting Information.

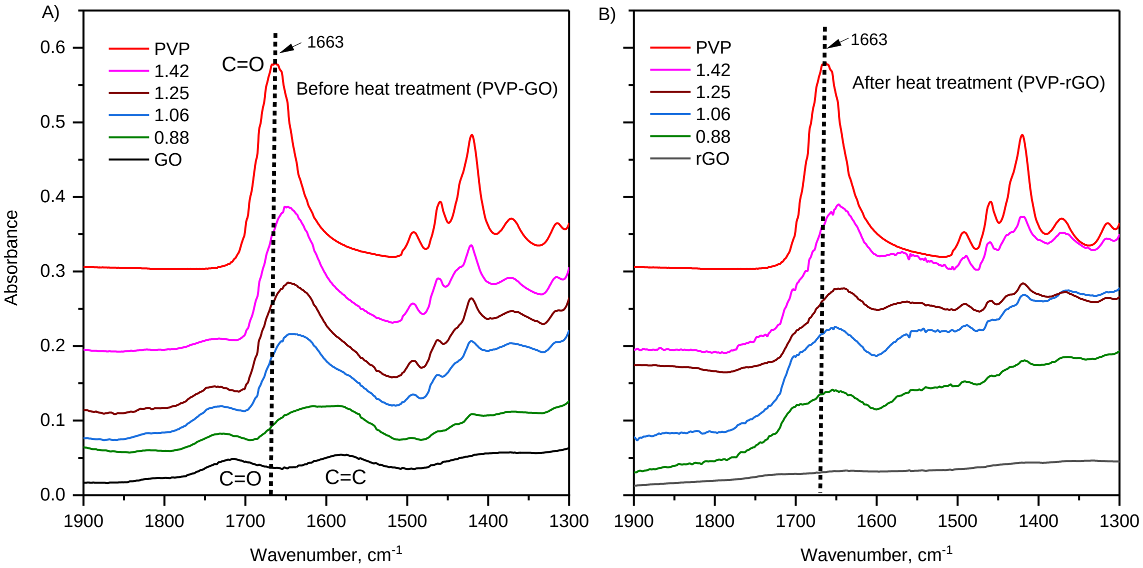

Figure 5.1. Partial FTIR spectra of nanocomposites A) before thermal treatment (PVP–GO) and B) after thermal treatment (PVP–rGO). The spectra are shifted vertically, and the intensity of the bulk PVP peak was reduced for comparison with the composites. The amount of PVP on the GO surface for each sample is expressed as mg of PVP per m^2 of GO.

FTIR spectroscopy was used to identify the presence of H–bonding between PVP and GO in PVP–GO composites and several other important observations.[2,4,25] Two types of hydrogen bonds (nitrogen atom and carbonyl group) of PVP[26,27] are possible with GO and rGO surfaces. However, due to steric limitations, nitrogen atoms tend to make weaker H-bonds, while the carbonyl group has stronger ones.[5] The carbonyl peak of bulk PVP appeared at 1663 cm^{-1} and shifted to a lower frequency (about 25 cm^{-1}) in the composites. The carbonyl peak of PVP in the composites appeared as a broad peak around 1638 cm^{-1} as shown in Figures 5.1A and 5.1B. This shift and broadening were consistent with the interaction between PVP and GO surface likely due to the donation of electrons from the hydroxyl groups of GO to the antibonding orbitals of carbonyl groups of PVP. [2,5] Second, the carbonyl peak of GO at 1715 cm^{-1} was shifted to a higher frequency (1730 cm^{-1}). Based on these observations, and previously reported work,[5] the direct interaction of PVP molecules with the GO surface via H-bonding was confirmed using FTIR spectroscopy.[1,13] The FTIR spectra of rGO and PVP–rGO composites are shown in Figure 5.1B. After the thermal treatment, the FTIR spectrum of rGO was relatively flat in the carbonyl and alkene regions. This spectrum was consistent with the elimination of many carbonyl and alkene groups on the GO due to the thermal treatment as per the previously reported work.[18] The carbonyl peak of PVP in the PVP–rGO composites also shifted to lower frequencies in the adsorbed polymer and appeared around 1638 cm^{-1}. This suggested that interactions existed between the PVP carbonyl groups and the undegraded carbonyl and alkene functional groups of GO even after the heat treatment.

FTIR spectroscopy has been used in past to characterize the behavior of polymer on a solid surface. Fontana and Thomas[2] estimated the fractions of bound carbonyls of alkyl methacrylate polymers adsorbed on solid surfaces in the presence of solvents as early as 1969. In more recent work, bound fractions of carbonyls in silica have been estimated for poly(methyl methacrylate) (PMMA)[28] and poly(ethylene-stat-vinyl acetate)[4] on silica surfaces.[3,17,25,29] The application of this technique to PVP–rGO composites is challenging due to the presence of additional functional groups on the GO surface such as carbonyl and alkene groups and the difference in the absorption coefficients of bound and free carbonyls.[28] These peaks are in proximity to the carbonyl group peak of PVP. Nevertheless, the FTIR can still identify the H–bonding of carbonyl groups in the PVP–rGO system.[4]

5.4.1. Thermogravimetric analysis

The thermal stability of the nanocomposites was evaluated using TGA, and the thermograms of GO, PVP, PVP–GO, and PVP–rGO composites are shown in Figure 5.2. The mass losses of GO and PVP–GO composites are shown in Figure 5.2A. In the GO thermogram, the mass losses over the ranges of 150–250, 250–450, and 450–650 °C are related to the degradation of functional groups, amorphous carbon atoms, and the graphite skeleton of GO, respectively.[5,6,30,31]

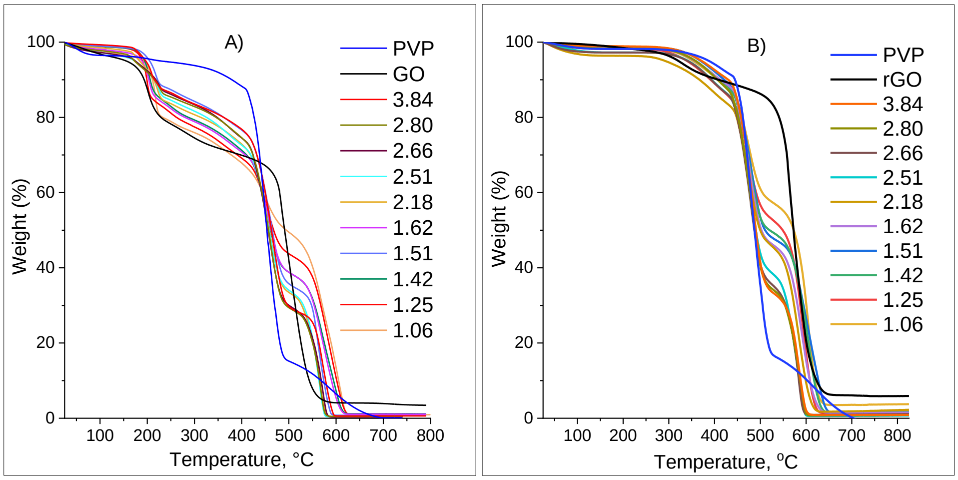

Figure 5.2. TGA thermograms of A) bulk PVP, GO, and PVP–GO before and B) after heat treatment along with PVP, rGO, and PVP–rGO composites. The amount of PVP adsorbed for each sample on the GO or rGO is expressed as mg of PVP per m^2 of GO or rGO.

The TGA thermogram of bulk PVP shows three major mass losses that can be assigned as follows. The first mass loss in the range of 25–150 °C can be attributed to the removal of adsorbed moisture, which was roughly 2%. The second and third mass losses in the range of 350–700 °C are related to the degradation of the polymer molecules.[30] The PVP–GO composites degrade in three steps that are a superposition of the individual thermograms of GO and PVP.

The TGA thermograms of rGO and PVP–rGO composites are shown in Figure 5.2B. The mass loss of PVP–rGO composites in the temperature range of 150–250 °C was negligible after heat treatment which confirmed the successful removal of most of the functional groups on the GO surface. The mass losses from 280–510 and 510–650 °C can be assigned to the degradation of PVP and degradation of graphene skeleton in the PVP–rGO composites. The mass losses in the polymer and rGO in PVP–rGO thermograms were used to calculate the composition of the composites.

The peak degradation temperatures of the composites have been identified using derivative TGA (DTGA) plots. Examples of DTGA thermograms for smaller and larger polymer-loaded samples are shown in Figures 5.3. The derivative mode makes it easier to see more of the details of the mass loss events. In addition, it shows more clearly how the relative intensities of the different degradations vary with the adsorbed amount.

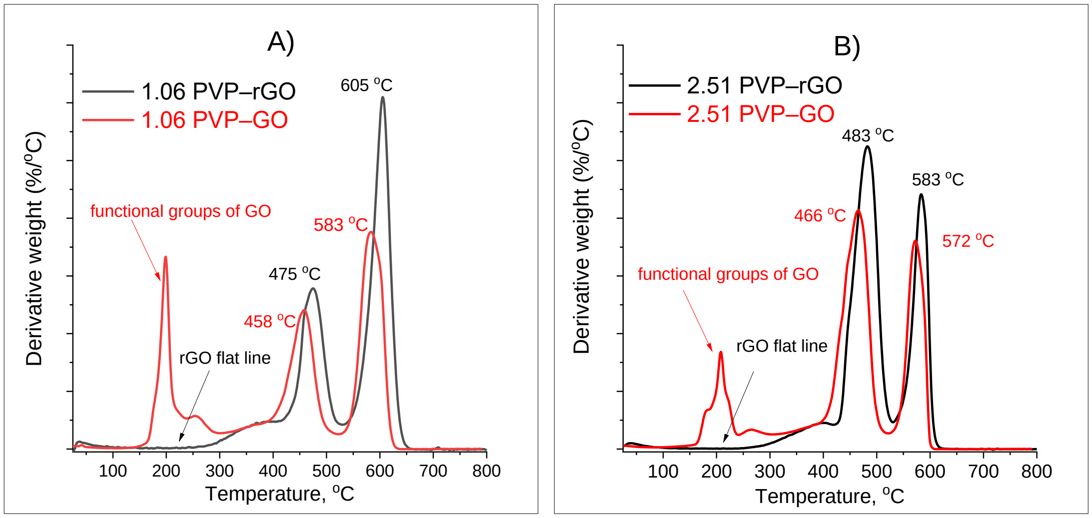

Figure 5.3. DTGA thermograms of A) 1.06 PVP–GO and PVP–rGO B) 2.51 PVP–GO and PVP–

rGO composites. The samples are labeled by the amount of PVP on the GO and rGO surfaces (mg of PVP per m^2 of GO).

The thermal stability of the PVP in the composites was increased significantly compared to bulk PVP (449 °C). In 1.06 and 2.51 mg/m^2 PVP–GO samples, the peak degradation temperature of PVP appeared at 458 and 466 °C, which is roughly a 9 and 17 °C increase compared to bulk PVP. In 1.06 and 2.51 mg/m^2 PVP–rGO composites, the peak degradation temperature of PVP was located at 475 and 483 °C, which is a 26 and 34 °C increase compared to the bulk PVP. The ripple structure of the graphene oxide sheets may have enhanced the thermal stabilities and also may have restricted the escape of some products from the adsorbed layers of graphene oxide.[5] We also believe that the GO surface restricted the mobility of the polymer chains in the composites and may have increased the overall thermal stability. Once the functional groups were removed, the increased thermal stability caused a shift in degradation temperature to a higher temperature than GO.[5,32,33]

5.4.2. Temperature-modulated differential scanning calorimetry

The TMDSC thermograms recorded for the PVP–rGO composites are shown in Figure 5.4. Since the intensity of the thermogram of the bulk polymer was large compared to those of the composites, the bulk PVP signal intensity was reduced in the figure to roughly match the size of the 1.06 mg/m2 PVP–rGO sample. In addition, the thermograms after 1.42 mg/m^2 were shifted on the vertical axis for clarity. The T_g of the bulk polymer and each composite was estimated as the maximum of the derivative of the reversing heat capacity vs. temperature curve.[28,34,35] Since TMDSC was used, we chose to report the *derivative reversing specific heat capacity* in Figure 5.4. The derivative is a useful way to observe the behavior of broad peaks more easily and makes subsequent processing easier (*vide infra*). In this case, the specific heat capacity reported was scaled with the *total mass* of the sample.

Several observations can be made from the thermograms in Figure 5.4. The T_g of the bulk PVP was 176 °C, which was consistent with the previously reported data.[36,37] The major component of the PVP–rGO thermograms was one large broad peak which was shifted to a higher temperature than that for the bulk polymer. This thermal transition in the composites in the 170–195 °C temperature range grew with adsorbed amounts into a slightly narrower peak, which moved towards the bulk transition, as expected. The shift of these peaks, which correlate with the bulk glass transition, towards T_g to higher temperatures has been observed in other systems.[17,34] This peak is referred to as a *loosely-bound* or *bulk-like* polymer that likely results from the changes in interfacial interactions between PVP segments with the residual functional groups of the rGO that influence the mobility at a distance.

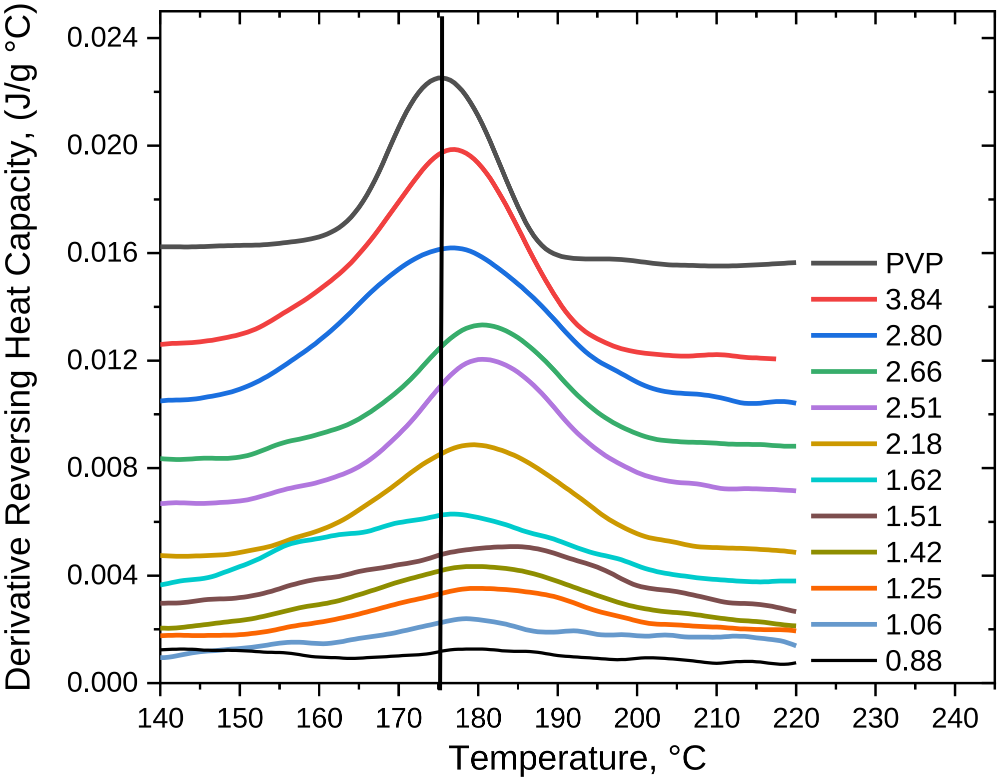

Figure 5.4. TMDSC thermograms (derivative reversing heat capacity) of PVP–rGO (ΔC_{sample}) normalized to the mass of the sample. The legend labels correspond to the amount of PVP

adsorbed per m^2 rGO surface in each sample. The intensity of the bulk PVP peak was adjusted to match the lower-intensity composite peaks. The composite curves were shifted vertically to visualize the thermal transitions and a vertical line has been drawn for reference at 175 °C.

In the thermograms, the smallest adsorbed amount sample (0.88 mg/m^2) showed limited thermal activity that was difficult to quantify, possibly due to the very small amount of polymer on the surface. As a result, that sample showed smaller heat capacity and more broadening of the transition for the adsorbed polymer.[35] It is believed that the glass transition of this sample may be somewhat buried within the baseline of the thermogram. However, when the polymer adsorbed amount increased to 1.06 mg/m^2, two small broad peaks were observed around 178 and 193 °C. The intensities in these regions increase with increasing adsorbed amount. These peaks may be assigned as *loosely* and *tightly-bound*, respectively. Although it is still difficult to estimate the amount of *tightly bound* components due to the shape/intensity of the peak, the thermal activity was eventually dominated by the *loosely-bound* (*bulk–like)* peak. It should also be noted that, when compared with bulk polymer, for the adsorbed samples, there is still a noticeable intense peak above the bulk T_g. In other words, this is a small, broad peak that is difficult to characterize.

In this system, the absence of a distinct peak for the tightly-bound polymer makes it impossible to use that peak for a detailed analysis of the *tightly-bound* polymer directly, as in our earlier work.[28,29] Therefore, we propose an alternative data analysis based on the *absence* of a *tightly-bound* polymer peak and its implications in the *loosely–bound* (*bulk–like*) peak. The model assumes that the glass transition of the *tightly-bound* polymer is not observed as a discernable peak and its thermal signature does *not* contribute to the *loosely–bound* peak. Nevertheless, its absence is indicated by the reduction in the intensity of the *loosely–bound* peak. This may be because the peak for the *tightly–bound* polymer is quite broad, has a small intensity, or both. Using a similar concept, Sargsyan et al.[38] suggested that an adsorbed polymer might exist as a “rigid amorphous fraction” which might not be observed. For some other adsorbed systems, including PMMA/silica, it has been shown that the *tightly–bound* polymer is not rigid and has a thermal signature for tightly adsorbed polymer.[3,28,38,39] We base the model on the assumptions that 1) the loosely-bound polymer has bulk–like properties and 2) the reduction of the intensity of the *loosely-bound* peak, compared to that expected if all the adsorbed polymers were *bulk–like*. This amount accounts for the "*missing*" or in other words *tightly-bound* polymer in the composite. Similar to the methodology of Sargasan et al.[38] we use this missing intensity to quantify the amount of *tightly bound* polymer. However, this is done with a recognition that the adsorbed material is "not rigid". It is observed that this material at least in part, has a thermal signature, which was not possible for us to quantify, but it has mobility and glass transition behavior.

For the glass transition of a bulk polymer, the change in heat capacity is related to the mass of the polymer times the *specific heat capacity change* (ΔC, J/g °C) over that region. When the heat capacity is plotted, the data shows a familiar sigmoidal polymer glass transition curve, with the change in heat capacities being the difference between the heat capacities of the rubbery and glassy polymer over the glass transition. With TMDSC, it is straightforward to plot the derivative of the *reversing* heat capacity,[3,28,35] as in Figure 5.4. Since there is little change in thermal activity for the rGO in the polymer glass transition range, the peaks shown in Figure 5.4. are essentially due to the activity of the polymer alone. Thus, given the appropriate choice of the baseline for the polymer, the ΔC for the loosely-bound polymer is simply the integral of the *loosely-bound* peak in the PVP-rGO derivative thermograms. This integral is over the glass transition range and uses the baseline along the curves from before and after the transition. The areas under each thermal transition were estimated using Gaussian peak fitting with Origin software. Examples of a few of these integrals are shown in the Supporting Information.

Both heat flow and heat capacity curves for a polymer sample in the glass transition region provide similar information. For simplicity, we will restrict the discussion to specific heat capacity curves, with the term *specific* referring to the mass of the *polymer alone*. The difference in the specific heat capacity curves for the glassy and rubbery polymer is proportional to the change in specific heat capacity, ΔC_{PVP} (J/g °C). Here PVP subscript implies that the heat capacity is normalized to the mass of PVP in the sample. In Figure 5.4, the reversing specific heat capacities shown were normalized to the total mass of the sample. The values of $\Delta C_{\mathrm{sample}}$ need to be converted to the change of the specific heat capacity of PVP since we are interested in the specific heat capacity relative to the mass of the polymer. For PVP, ΔC_{PVP} can be calculated through the mass ratio, or

$$\Delta \mathrm{C}_{PVP} = \frac{\Delta C_{sample} \times m_{sample}}{m_{PVP}} \tag{5.1}$$

As mentioned above, the TMDSC curves of Figure 5.4 were integrated to yield $\Delta C_{\mathrm{sample}}$ and then for change in specific heat capacity for adsorbed PVP, ΔC_{PVP}.

In principle, the value of $\Delta \mathrm{C}_{\mathrm{PVP}}$ includes the changes in heat capacity for both *loosely* and *tightly-bound* polymers. However, since the *tightly-bound* PVP does not seem to have a measurable thermal signature, the measured $\Delta \mathrm{C}_{\mathrm{PVP}}$ value is taken to be an estimate of the specific heat capacity for the amount of *loosely–bound* polymer in each sample. Then the value of ΔS_{PVP} calculated for each sample was compared with ΔC_{PVP}^{Bulk} to yield an estimate of the fraction of *tightly-bound* polymer, f_{B} as:

$$f_B = 1 - \frac{\Delta C_{PVP}}{\Delta C_{PVP}^{Bulk}} \tag{5.2}$$

The values of ΔC_{PVP} and the resulting *tightly-bound* PVP fractions, f_{B} as a function of adsorbed amount are shown in Table 5.1. As expected, the f_{B} decreased with an increased adsorbed amount. In addition, it is possible to predict how the *tightly-bound* fraction, f_{B} should depend on the adsorbed amount, AA (mg polymer/m^2 rGO), The adsorbed amounts are based on a specific surface area of GO to be 0.722 m^2/mg.[40] For a simple two–state model, as the polymer is added to the surface, it first goes on as *tightly–bound* polymer until an amount, m'_B is obtained. This m'_B is the amount of polymer that makes complete layer of *tightly-bound* polymer. Below m'_B, $f_B = 1$. Above that amount, it is given by

$$f_B = 1 - \frac{m'_B}{AA} \tag{5.3}$$

Table 5.1. Thermal properties of bulk–like transitions of the composite materials. The fractions of tightly bound polymer, f_B were calculated from Equation 5.3 based on ΔC_{PVP}^{Bulk} = 0.204 (J/g °C).

Adsorbed amount, AA (mg/m^2)	ΔC_{PVP} (J/g °C)	f_B	T_g, center (°C)
0.88	~0.00	1	-
1.06	0.008	0.908	188
1.25	0.026	0.726	183
1.42	0.047	0.536	184
1.51	0.058	0.445	181
1.62	0.058	0.468	177
2.18	0.079	0.354	178
2.51	0.081	0.364	180
2.66	0.094	0.285	181
2.80	0.095	0.290	177
3.84	0.110	0.252	176
Bulk	0.204	0	176

As identified in Equation 5.3, f_B should be proportional to *1/AA*. A plot of the values of f_B as a function of *1/AA* is shown in Figure 5.5 and the data show a good linear fit. This plot was a force fit with zero intercept. The least-squares fit of the data with Gaussian peak fitting yields a slope of 0.84 ± 0.03 (SD). This suggests that the amount of *tightly-bound* PVP on the rGO surface is m'_B = 0.84 ± 0.03 (SD) mg/m^2. If the intercept was left as a parameter, the fits yield similar results, and this fit is shown in the Supporting Information.

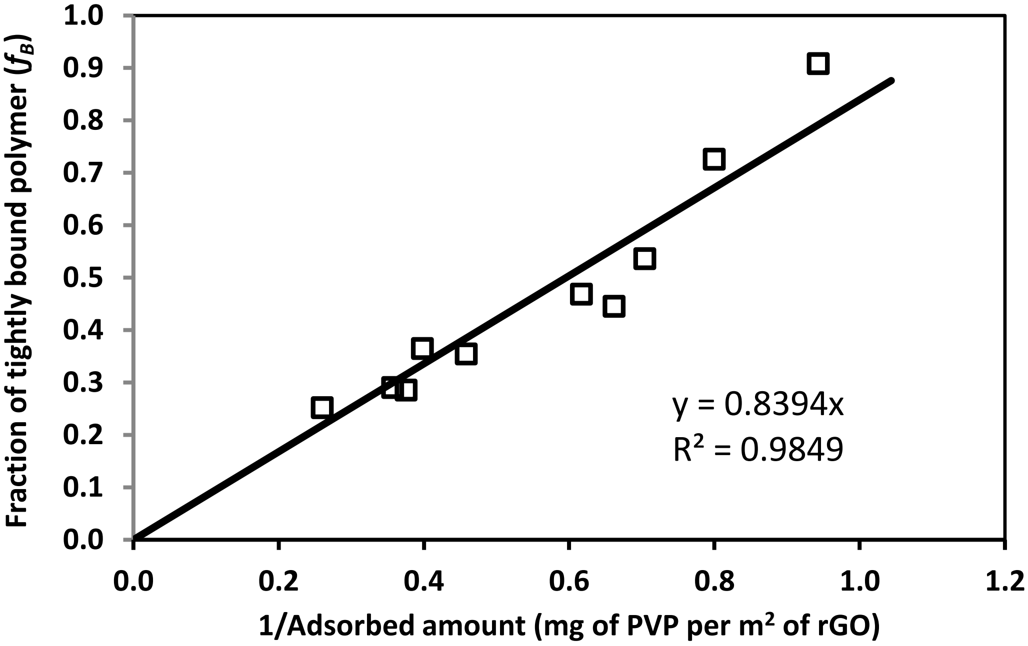

Figure 5.5. The linear regression data of the area under the peak of *loosely bound* PVP in TMDSC thermograms fitted to the model.

It is interesting to compare the value of m'_B with previously determined values from other polymers on silica. The amounts of tightly bound polymers on different systems are tabulated in Table 5.2. Two of these tightly bound amounts are shown for both poly(methyl methacrylate) (PMMA) and poly(vinyl acetate). It is important to note that with this rather different system, PVP-rGO, the values of all systems are fairly similar. At least where similar techniques have been used on these systems, the approximate scale of 1 mg/m^2 seems to be common for the amount of *tightly-bound* polymer.[4,25,28,29,35]

Table 5.2. Amount of adsorbed polymer on various systems from TMDSC measurements based on a simple two-state model.

Polymer system	Amount of tightly bound polymer, m'_B (mg/m^2)	Heat capacity of bulk polymer, at 300 K, J/g °C	Reference
Silica–PMMA	1.21 ± 0.21	1.37*	Khatiwada and Blum[3]
Silica–PVAc	0.78 ± 0.03	1.12*	Mortazavian et al.[34]
PVP–rGO	0.84 ± 0.3	1.25[41]	This work

*heat capacity data from polymer handbook.[42]

In the silica–PMMA system, the tightly bound polymer showed clear thermal activity. The *tightly-bound* polymer peak was observable at elevated temperatures compared to the bulk polymer.[28,34,35] The *tightly-bound* fraction was showed to have a DSC glass transition as much as 40 – 60 °C higher than that of the bulk polymer. A similar situation was also found for the adsorption of poly(vinyl acetate) (PVAc) on silica. For PVAc–silica the elevation in glass transition was lower about 25 °C. Simulations have shown that the strength of the interaction between PMMA and silica was stronger than PVAc on silica.[39] The strength of the interaction plus the inherent difference in T_g (Bulk) because of their different mobilities and likely the reason for the differences in the elevation of the T_g's for both systems. The sensitivity of these measurements was due to the ΔC_p measurements over the glass transitions. For adsorbed PMMA, the fractional heat capacity has been measured and has been estimated for the polymer first adsorbed on silica. The values of the fractional heat capacities of the polymer, first adsorbed range from 0.3 to 0.8 from 30 to 200 °C. Interestingly, for

PMMA/silica system, for the adsorbed amount of 1.2 mg/m^2, the fractional heat capacity was found to be 80% of the tightly adsorbed amount.[3] Also, the change in heat capacity at the tightly adsorbed amount was estimated to be about 1/6 of that for the bulk polymer. This smaller ΔC_p means reduced intensity for the thermal signal of the *tightly-bound* polymer making its measurement more difficult.

For the PVP–rGO composites, it was not possible to clearly distinguish the *tightly-bound* fraction from the *bulk–like* polymer in the thermograms, unlike PMMA or PVAc on silica. The recognizable thermal transition peak of tightly bound PMMA at elevated temperatures may be due to the larger values of C_p, ΔC_p, relating to the strength of the interaction with the substrate or the decreased breadth of the transition for *tightly-bound* PMMA-silica compared to PVP-rGO. In any case, based on the analysis we used, we obtained quite a reasonable value for the amount of *tightly-bound* PVP on rGO.

5.5. CONCLUSIONS:

In this work, we used FTIR spectroscopy and TMDSC analyses to study the interface between PVP and rGO composites. The study of PVP on the GO surface is challenging due to the thermal degradation of the GO functional groups near the T_g of the polymer. Therefore, the composites were heat treated to carry out the in-situ reduction of GO to make rGO. The FTIR spectra of composites before and after heat treatment still showed evidence of hydrogen bonding between PVP carbonyl groups and functional groups of the GO surface. Some of the functional groups, which had already been covered by the PVP molecules, remained on the surface even after thermal treatment. Hence, a shift of the carbonyl peak of PVP in FTIR spectra was observed in PVP–rGO composites. TMDSC analysis was carried out to estimate the amount of PVP that was *tightly-bound* to the GO surface, indicative of the interaction between the polymer and the GO. This thermal treatment did not seem to remove the PVP interactions which result in a higher glass transition for the PVP interphase. Despite the complications due to not observing a separate peak for the *tightly-bound*

PVP, it was possible to account for it. Gaussian fit thermogram peaks were fitted to the model to estimate the *tightly-bound* fraction of PVP on the GO surface as 0.84 ± 0.03 mg/m2. The T_g of the loosely-bound PVP was also elevated in the composite by as much as 12 °C compared to the bulk polymer

5.6. ACKNOWLEDGEMENTS

The authors acknowledge the financial support provided by H.I. Bartlett Chair Endowment for this work.

ORCID

Ishan N. Jayalath: 0000-0002-0855-5663

Ranji Vaidyanathan: 0000-0003-3697-4264

Frank D. Blum: 0000-0002-7884-3134

5.7. REFERENCES

1. Yin, B.; Wang, J.; Jia, H.; He, J.; Zhang, X.; Xu, Z., Enhanced mechanical properties and thermal conductivity of styrene–butadiene rubber reinforced with polyvinylpyrrolidone-modified graphene oxide. *Journal of Materials Science* **2016,** *51* (12), 5724-5737.

2. Fontana, B. J.; Thomas, J. R., The configuration of adsorbed alkyl methacrylate polymers by infrared and sedimentation studies. *The Journal of Physical Chemistry* **1961,** *65* (3), 480-487.

3. Khatiwada, B. K.; Hetayothin, B.; Blum, F. D., Thermal properties of PMMA on silica using temperature-modulated differential scanning calorimetry. *Macromolecular Symposia* **2013,** *327* (1), 20-28.

4. Maddumaarachchi, M.; Blum, F. D., Thermal analysis and FT-IR studies of adsorbed poly(ethylene-stat-vinyl acetate) on silica. *Journal of Polymer Science Part B: Polymer Physics* **2014,** *52* (10), 727-736.

5. Chen, S.; Cheng, B.; Ding, C., Synthesis and characterization of Poly(vinyl pyrrolidone)/Reduced graphene oxide nanocomposite. *Journal of Macromolecular Science, Part B* **2015,** *54* (4), 481-491.

6. Ma, X.; Xie, G.; Su, Y.; Du, H.; Xie, T.; Jiang, Y., Polyvinylpyrrolidone/graphene oxide thin films coated on quartz crystal microbalance electrode for NH_3 detection at room temperature. *Science China Technological Sciences* **2016,** *59* (9), 1377-1382.

7. Li, X.; Deng, H.; Li, Z.; Xiu, H.; Qi, X.; Zhang, Q.; Wang, K.; Chen, F.; Fu, Q., Graphene/thermoplastic polyurethane nanocomposites: Surface modification of graphene through oxidation, polyvinyl pyrrolidone coating and reduction. *Composites Part A: Applied Science and Manufacturing* **2015,** *68*, 264-275.

8. Gill, F. S.; Uniyal, D.; Prasad, B.; Saluja, S.; Mishra, A.; Bachheti, R. K.; Juyal, S., Investigation of increased electrical conductivity by rGO in rGO/PVDF/PMMA/PTFE nanocomposites. *Journal of Molecular Structure* **2022,** *1267*, 133541.

9. Marami, G.; Nazari, S. A.; Faghidian, S. A.; Vakili-Tahami, F.; Etemadi, S., Improving the mechanical behavior of the adhesively bonded joints using RGO additive. *International Journal of Adhesion and Adhesives* **2016,** *70*, 277-286.

10. Chen, J.; Wu, J.; Ge, H.; Zhao, D.; Liu, C.; Hong, X., Reduced graphene oxide deposited carbon fiber reinforced polymer composites for electromagnetic interference shielding. *Composites Part A: Applied Science and Manufacturing* **2016,** *82*, 141-150.

11. Yang, B.; Wei, Y.; Liu, Q.; Luo, Y.; Qiu, S.; Shi, Z., Polyvinylpyrrolidone functionalized magnetic graphene-based composites for highly efficient removal of lead from wastewater. *Colloids and Surfaces A: Physicochemical and Engineering Aspects* **2019,** *582*, 123927.

12. Wu, X.; Field, R. W.; Wu, J. J.; Zhang, K., Polyvinylpyrrolidone modified graphene oxide as a modifier for thin film composite forward osmosis membranes. *Journal of Membrane Science* **2017,** *540*, 251-260.

13. Zhang, X.; Wang, J.; Jia, H.; Yin, B.; Ding, L.; Xu, Z.; Ji, Q., Polyvinyl pyrrolidone modified graphene oxide for improving the mechanical, thermal conductivity and solvent resistance properties of natural rubber. *Royal Society of Chemistry Advances* **2016,** *6* (60), 54668-54678.

14. Zou, R.; Su, L.; Zhang, L.; Hu, N.; Yue, D., Polyvinyl pyrrolidone grafted silica reinforced hydrogenated carboxylated nitrile latex film with improved mechanical properties. *Composites Communications* **2017,** *6*, 25-28.

15. Fleer, G. J., Polymers at interfaces and in colloidal dispersions. *Advances in Colloid and Interface Science* **2010,** *159* (2), 99-116.

16. Ploehn, H. J., Polymers at Interfaces. *Journal of the American Chemical Society* **1996,** *118* (1), 297-298.

17. Blum, F. D., Glass Transition Behavior of PMMA Thin Films. *Polymer Preprints, American Chemical Society* **2001,** *42(2)*, 67-98.

18. Oliveira, A. E. F.; Braga, G. B.; Tarley, C. R. T.; Pereira, A. C., Thermally reduced graphene oxide: synthesis, studies and characterization. *Journal of Materials Science* **2018,** *53* (17), 12005-12015.

19. Yu, W.; Fu, J.; Dong, X.; Chen, L.; Shi, L., A graphene hybrid material functionalized with POSS: synthesis and applications in low-dielectric epoxy composites. *Composites Science and Technology* **2014,** *92*, 112-119.

20. Divakaran, N.; Kale, M. B.; Senthil, T.; Mubarak, S.; Dhamodharan, D.; Wu, L.; Wang, J., Novel unsaturated polyester nanocomposites via Hybrid 3D POSS-modified graphene oxide reinforcement: electro-technical application perspective. *Nanomaterials (Basel)* **2020,** *10* (2).

21. Zhang, M.; Yan, H.; Yuan, L.; Liu, C., Effect of functionalized graphene oxide with hyperbranched POSS polymer on mechanical and dielectric properties of cyanate ester composites. *Royal Society of Chemistry Advances* **2016,** *6* (45), 38887-38896.

22. Zhang, R. L.; Gao, B.; Du, W. T.; Zhang, J.; Cui, H. Z.; Liu, L.; Ma, Q. H.; Wang, C. G.; Li, F. H., Enhanced mechanical properties of multiscale carbon fiber/epoxy composites by fiber surface treatment with graphene oxide/polyhedral oligomeric silsesquioxane. *Composites Part A: Applied Science and Manufacturing* **2016,** *84*, 455-463.

23. Lu, Y.; Zhang, S.; Geng, Z.; Zhu, K.; Zhang, M.; Na, R.; Wang, G., Hybrid formation of graphene oxide–POSS and their effect on the dielectric properties of poly(aryl ether ketone) composites. *New Journal of Chemistry* **2017,** *41* (8), 3089-3096.

24. Ata, S.; Banerjee, S. L.; Singha, N. K., Polymer nano-hybrid material based on graphene oxide/POSS via surface initiated atom transfer radical polymerization (SI-ATRP): Its application in specialty hydrogel system. *Polymer* **2016,** *103*, 46-56.

25. Kulkeratiyut, S.; Kulkeratiyut, S.; Blum, F. D., Bound carbonyls in PMMA adsorbed on silica using transmission FTIR. *Journal of Polymer Science Part B: Polymer Physics* **2006,** *44* (15), 2071-2078.

26. Zhang, X.; Wang, J.; Jia, H.; Yin, B.; Ding, L.; Xu, Z.; Ji, Q., Polyvinyl pyrrolidone modified graphene oxide for improving the mechanical, thermal conductivity and solvent resistance properties of natural rubber. *RSC Advances* **2016,** *6* (60), 54668-54678.

27. Huang, J.; Xie, G.; Zhou, Y.; Xie, T.; Tai, H.; Yang, G., Polyvinylpyrrolidone/reduced graphene oxide nanocomposites thin films coated on quartz crystal microbalance for NO_2 detection at room temperature. SPIE: 2014; Vol. 9285.

28. Blum, F. D.; Young, E. N.; Smith, G.; Sitton, O. C., Thermal analysis of adsorbed poly(methyl methacrylate) on silica. *Langmuir* **2006,** *22* (10), 4741-4744.

29. Kabomo, T.; Blum, F., Glass transition behavior of PMMA thin films. *Polymer Preprints, American Chemical Society* **2001,** *42* (2), 67-68.

30. El Achaby, M.; Essamlali, Y.; El Miri, N.; Snik, A.; Abdelouahdi, K.; Fihri, A.; Zahouily, M.; Solhy, A., Graphene oxide reinforced chitosan/polyvinylpyrrolidone polymer bio-nanocomposites. *Journal of Applied Polymer Science* **2014,** *131* (22), 41042-41053.

31. Justh, N.; Berke, B.; László, K.; Szilágyi, I. M., Thermal analysis of the improved Hummers' synthesis of graphene oxide. *Journal of Thermal Analysis and Calorimetry* **2017,** *131* (3), 2267-2272.

32. Salavagione, H. J.; Martínez, G.; Gómez, M. A., Synthesis of poly(vinyl alcohol)/reduced graphite oxide nanocomposites with improved thermal and electrical properties. *Journal of Materials Chemistry* **2009,** *19* (28).

33. Kuila, T.; Bose, S.; Hong, C. E.; Uddin, M. E.; Khanra, P.; Kim, N. H.; Lee, J. H., Preparation of functionalized graphene/linear low density polyethylene composites by a solution mixing method. *Carbon* **2011,** *49* (3), 1033-1037.

34. Mortazavian, H.; Fennell, C. J.; Blum, F. D., Structure of the interfacial region in adsorbed poly(vinyl acetate) on silica. *Macromolecules* **2015,** *49* (1), 298-307.

35. Khatiwada, B. K.; Blum, F. D., Tightly bound PMMA on silica has reduced heat capacities. *Langmuir* **2019,** *35* (35), 11482-11490.

36. Cassu, S. N.; Felisberti, M. I., Poly(vinyl alcohol) and poly(vinyl pyrrolidone) blends: miscibility, microheterogeneity and free volume change. *Polymer* **1997,** *38* (15), 3907-3911.

37. Kurakula, M.; Rao, G., Pharmaceutical assessment of polyvinylpyrrolidone (PVP): As excipient from conventional to controlled delivery systems with a spotlight on COVID-19 inhibition. *J Drug Deliv Sci Technol* **2020,** *60*, 102046.

38. Sargsyan, A. G.; Tonoyan, A.; Davtyan, S.; Schick, C., The amount of immobilized polymer in PMMA SiO2 nanocomposites determined from calorimetric data. *European Polymer Journal* **2007**, 3113-3127.

39. Mortazavian, H.; Fennell, C. J.; Blum, F. D., Structure of the interfacial region in adsorbed poly(vinyl acetate) on silica. *Macromolecules* **2016,** *49* (1), 298-307.

40. Montes-Navajas, P.; Asenjo, N. G.; Santamaria, R.; Menendez, R.; Corma, A.; Garcia, H., Surface area measurement of graphene oxide in aqueous solutions. *Langmuir* **2013,** *29* (44), 13443-8.

41. http://polymerdatabase.com/polymers/polyvinylpyrrolidone.html.

42. Mark, J. E., *Physical properties of polymers handbook*. Springer New York, NY: p 1076.

5.8. SUPPORTING INFORMATION

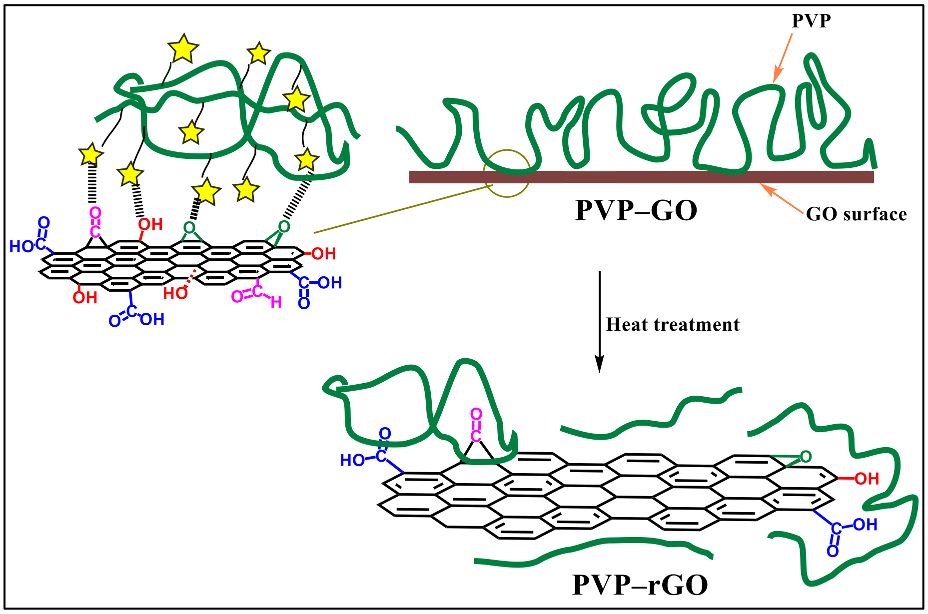

Contents

5.S1. GLOSSARY OF SYMBOLS

A mathematical model was developed to estimate the tightly bound polymer on the rGO surface using the specific heat capacity of bulk polymer and polymer composites. Different symbols used for the model are listed in Table 5.S1.

Table 5.S1. Glossary of symbols and description

Sign	**Description**
$\Delta \boldsymbol{C}_{\boldsymbol{sample}}$	Specific heat capacity change of sample per mass of sample (J/g)
$\Delta \boldsymbol{C}_{\boldsymbol{PVP}}$	Specific heat capacity change of PVP per mass of the polymer (J/g)
$\Delta \mathrm{C}_{\mathrm{PVP}}^{\boldsymbol{Bulk}}$	Specific heat capacity change of bulk PVP per mass of PVP (J/g)
$\mathrm{m}_{\mathrm{PVP}}$	Mass of PVP in the sample (g)
$\mathrm{m}_{\boldsymbol{sample}}$	Mass of the sample (sum of PVP and or GO) (g)
$\boldsymbol{m'}_{\mathbf{B}}$	Amount of tightly-bound polymer at full tightly-bound polymer amount (mg/m^2)
AA	Adsorbed amount (mg of PVP per m^2 of GO or rGO)
$\boldsymbol{f}_{\mathrm{PVP}}^{\mathrm{A}}$	Fraction of loosely-bound PVP
$\boldsymbol{f}_{\mathrm{PVP}}^{\boldsymbol{B}}$	Fraction of tightly-bound PVP

5.S2. FTIR SPECTRA OF PVP-GO COMPOSITES

The ATR-FTIR spectroscopy was used to identify the probable interaction between GO and PVP molecules. The full FTIR spectra of composites are shown in Figure 5.S1.

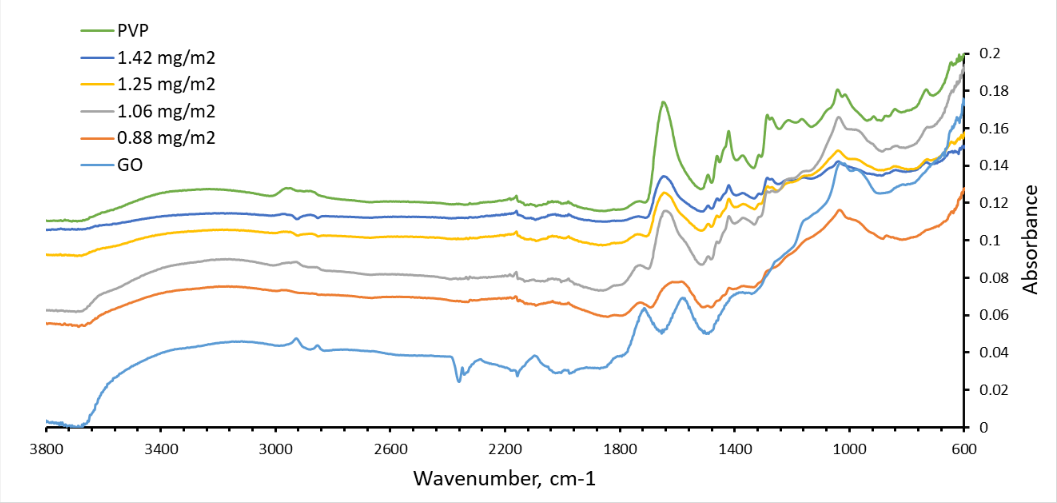

Figure 5.S1. FTIR spectra of GO, PVP, and untreated PVP–GO composites

5.S3. A PLOT OF TIGHTLY BOUND FRACTION (f_B) AS A FUNCTION OF RECIPROCAL OF ADSORBED AMOUNT (1/AA*)*

The least-squares fit of the data with Gaussian peak fitting without using a forced fit to zero f_B is shown in Figure 5.S2.

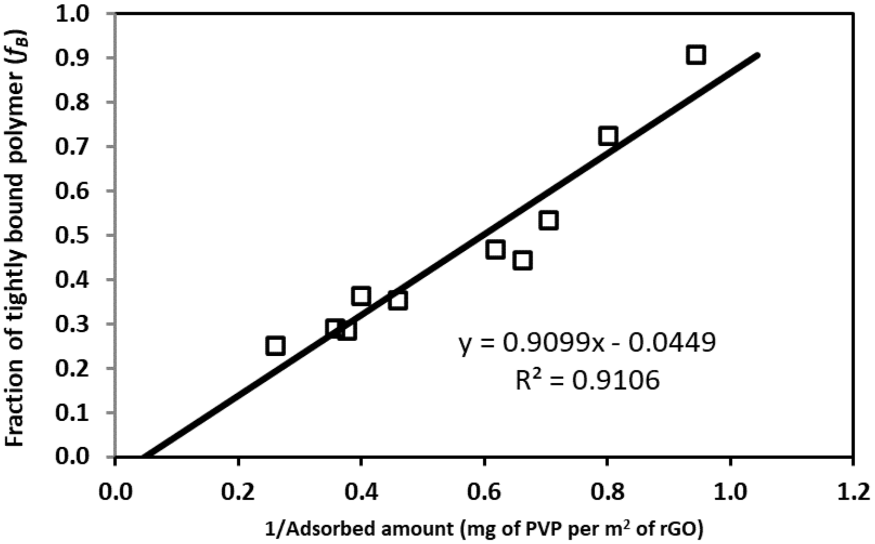

Figure 5.S2. The linear regression data of area under the peak of loosely bound PVP in TMDSC thermograms fitted to the model allow the intercept as a parameter.

5.S4. EXAMPLES OF GAUSSIAN PEAK FIT OF THE TMDSC THERMOGRAMS

The Gaussian peak fit of the 1.06 mg/m^2 sample is shown in Figure 5.S3. The area under the bulk-like peak (ΔC_{comp}) was estimated as 0.00802.

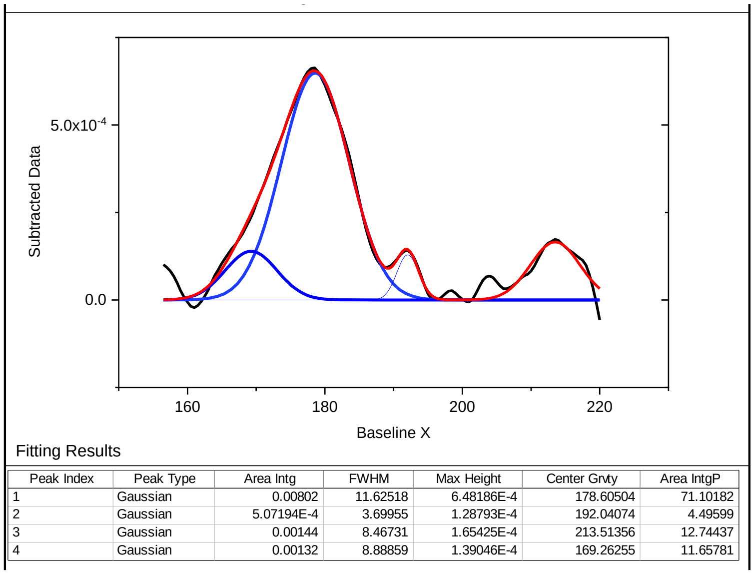

Fitting Results

Peak Index	Peak Type	Area Intg	FWHM	Max Height	Center Grvty	Area IntgP
1	Gaussian	0.00802	11.62518	6.48186E-4	178.60504	71.10182
2	Gaussian	5.07194E-4	3.69955	1.28793E-4	192.04074	4.49599
3	Gaussian	0.00144	8.46731	1.65425E-4	213.51356	12.74437
4	Gaussian	0.00132	8.88859	1.39046E-4	169.26255	11.65781

Figure 5.S3. Gaussian peak fitting of 1.06 mg/m^2 PVP–rGO sample.

The Gaussian peak fit of the 1.25 mg/m^2 sample is shown in Figure 5.S4. The area under the bulk-like peak (ΔC_{comp}) was estimated as 0.026.

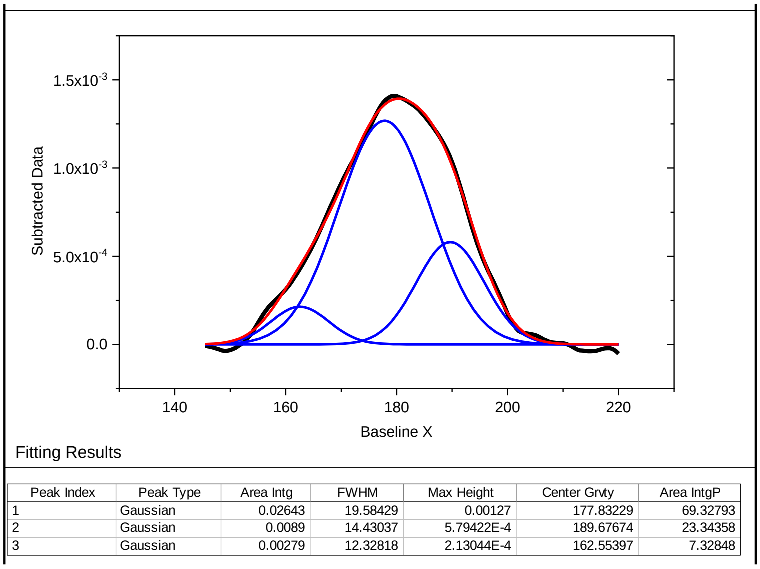

Fitting Results

Peak Index	Peak Type	Area Intg	FWHM	Max Height	Center Grvty	Area IntgP
1	Gaussian	0.02643	19.58429	0.00127	177.83229	69.32793
2	Gaussian	0.0089	14.43037	5.79422E-4	189.67674	23.34358
3	Gaussian	0.00279	12.32818	2.13044E-4	162.55397	7.32848

Figure 5.S4. Gaussian peak fitting of 1.25 mg/m^2 PVP–rGO sample.

The Gaussian peak fit of the 1.42 mg/m^2 sample is shown in Figure 5.S5. The area under the bulk-like peak (ΔC_{comp}) was estimated as 0.047.

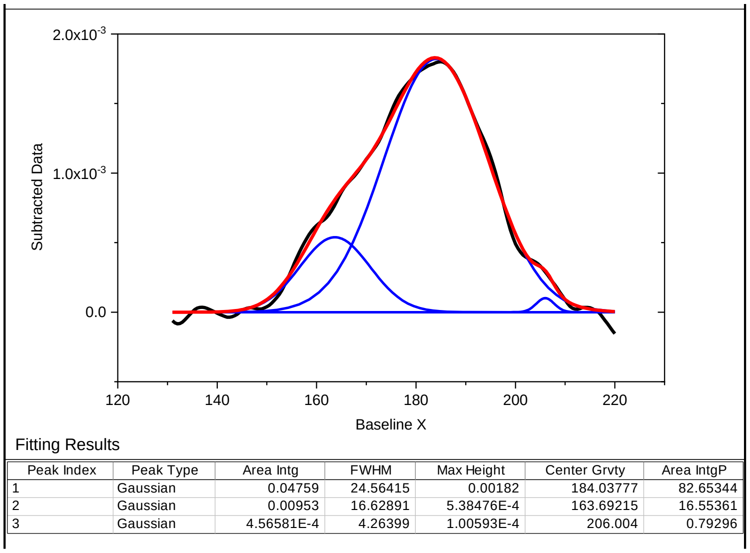

Fitting Results

Peak Index	Peak Type	Area Intg	FWHM	Max Height	Center Grvty	Area IntgP
1	Gaussian	0.04759	24.56415	0.00182	184.03777	82.65344
2	Gaussian	0.00953	16.62891	5.38476E-4	163.69215	16.55361
3	Gaussian	4.56581E-4	4.26399	1.00593E-4	206.004	0.79296

Figure 5.S5. Gaussian peak fitting of 1.42 mg/m^2 PVP–rGO sample.

The Gaussian peak fit of the 1.51 mg/m^2 sample is shown in Figure 5.S6. The area under the bulk-like peak (ΔC_{comp}) was estimated as 0.058.

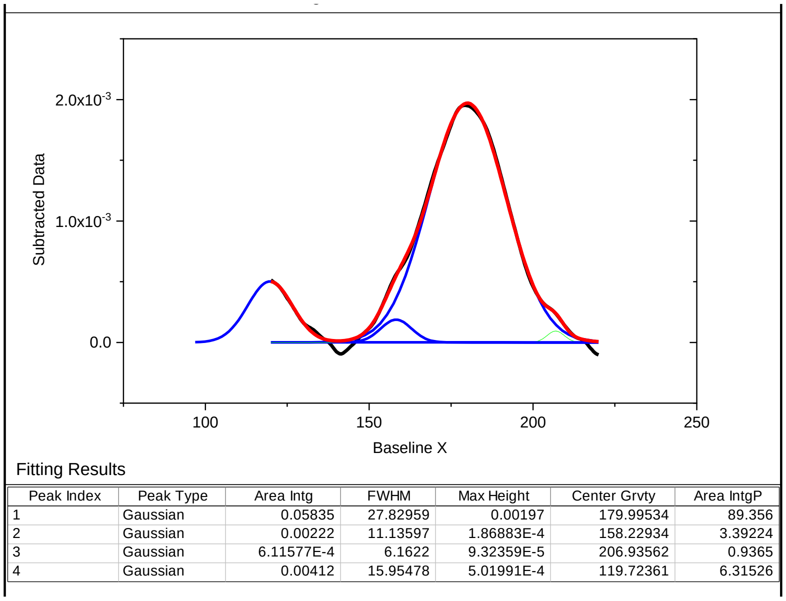

Fitting Results

Peak Index	Peak Type	Area Intg	FWHM	Max Height	Center Grvty	Area IntgP
1	Gaussian	0.05835	27.82959	0.00197	179.99534	89.356
2	Gaussian	0.00222	11.13597	1.86883E-4	158.22934	3.39224
3	Gaussian	6.11577E-4	6.1622	9.32359E-5	206.93562	0.9365
4	Gaussian	0.00412	15.95478	5.01991E-4	119.72361	6.31526

Figure 5.S6. Gaussian peak fitting of 1.51 mg/m^2 PVP–rGO sample

The Gaussian peak fit of the 1.62 mg/m^2 sample is shown in Figure 5.S7. The area under the bulk-like peak (ΔC_{comp}) was estimated as 0.079.

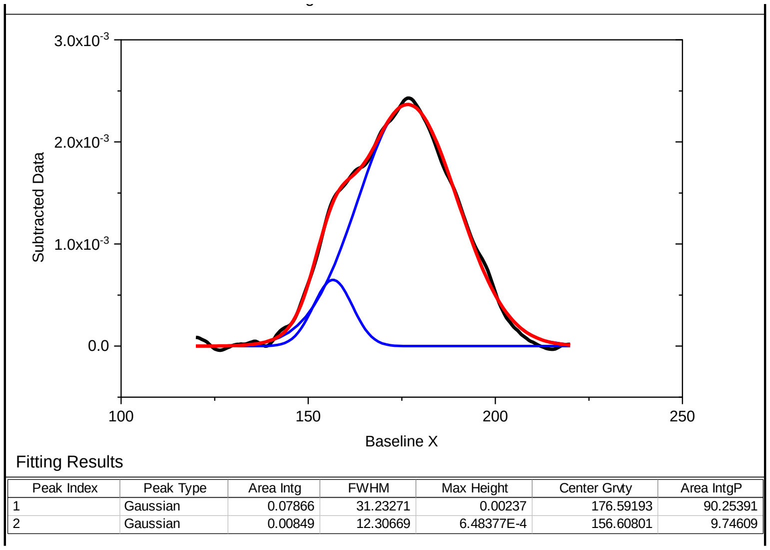

Fitting Results

Peak Index	Peak Type	Area Intg	FWHM	Max Height	Center Grvty	Area IntgP
1	Gaussian	0.07866	31.23271	0.00237	176.59193	90.25391
2	Gaussian	0.00849	12.30669	6.48377E-4	156.60801	9.74609

Figure 5.S7. Gaussian peak fitting of 1.62 mg/m^2 PVP–rGO sample.

The Gaussian peak fit of the 2.18 mg/m^2 sample is shown in Figure 5.S8. The area under the bulk-like peak (ΔC_{comp}) was estimated as 0.12.

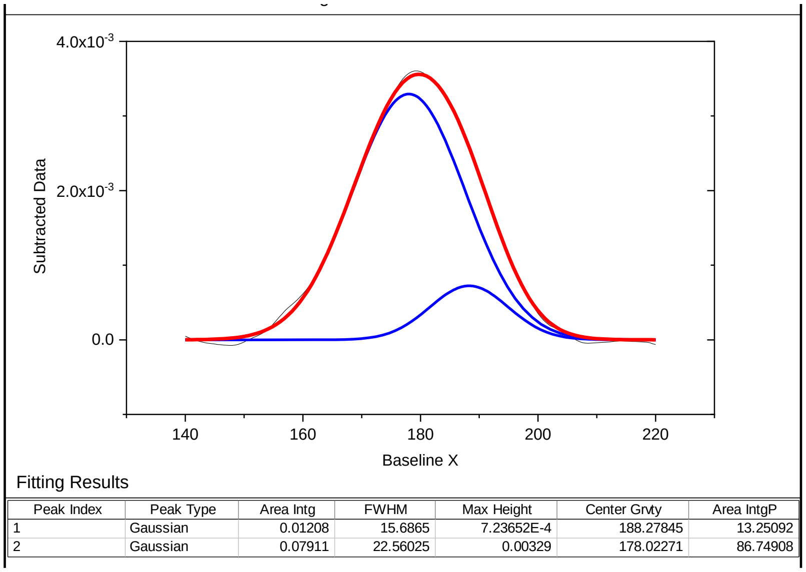

Fitting Results

Peak Index	Peak Type	Area Intg	FWHM	Max Height	Center Grvty	Area IntgP
1	Gaussian	0.01208	15.6865	7.23652E-4	188.27845	13.25092
2	Gaussian	0.07911	22.56025	0.00329	178.02271	86.74908

Figure 5.S8. Gaussian peak fitting of 2.18 mg/m^2 PVP–rGO sample

The Gaussian peak fit of the 2.51 mg/m^2 sample is shown in Figure 5.S9. The area under the bulk-like peak (ΔC_{comp}) was estimated as 0.08.

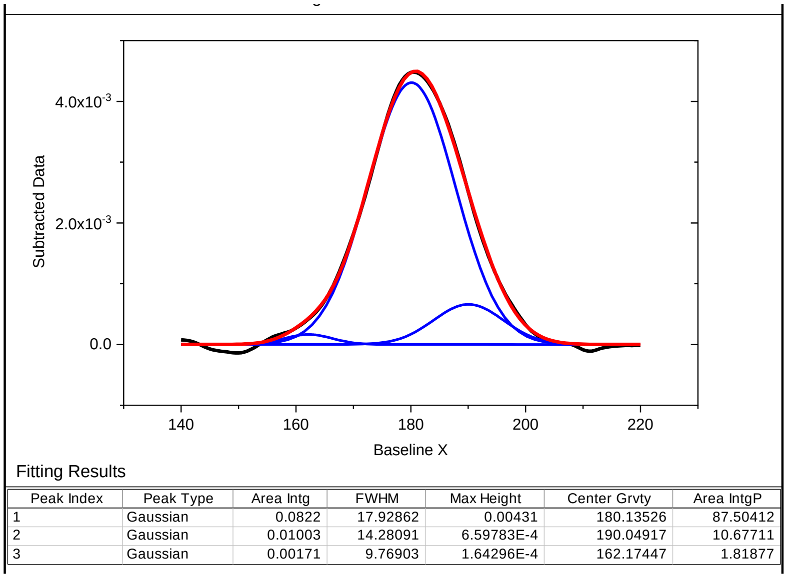

Fitting Results

Peak Index	Peak Type	Area Intg	FWHM	Max Height	Center Grvty	Area IntgP
1	Gaussian	0.0822	17.92862	0.00431	180.13526	87.50412
2	Gaussian	0.01003	14.28091	6.59783E-4	190.04917	10.67711
3	Gaussian	0.00171	9.76903	1.64296E-4	162.17447	1.81877

Figure 5.S9. Gaussian peak fitting of 2.51 mg/m^2 PVP–rGO sample

The Gaussian peak fit of the 2.66 mg/m^2 sample is shown in Figure 5.S10. The area under the bulk-like peak (ΔC_{comp}) was estimated as 0.095.

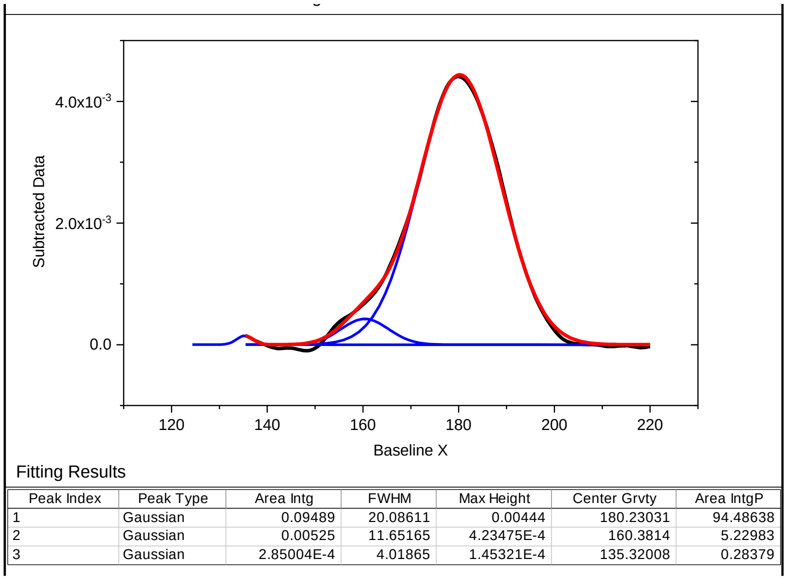

Fitting Results

Peak Index	Peak Type	Area Intg	FWHM	Max Height	Center Grvty	Area IntgP
1	Gaussian	0.09489	20.08611	0.00444	180.23031	94.48638
2	Gaussian	0.00525	11.65165	4.23475E-4	160.3814	5.22983
3	Gaussian	2.85004E-4	4.01865	1.45321E-4	135.32008	0.28379

Figure 5.S10. Gaussian peak fitting of 2.66 mg/m2 PVP–rGO sample

The Gaussian peak fit of the 2.80 mg/m^2 sample is shown in Figure 5.S11. The area under the bulk-like peak (ΔC_{comp}) was estimated as 0.113.

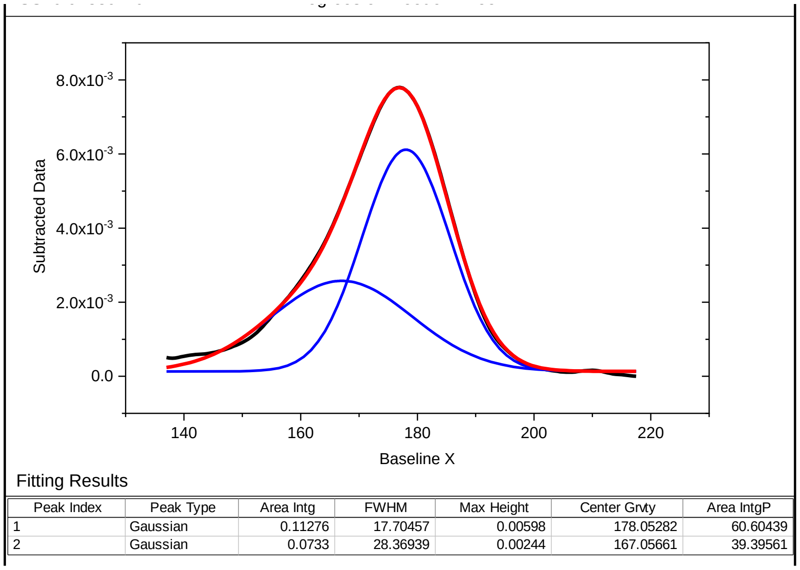

Fitting Results

Peak Index	Peak Type	Area Intg	FWHM	Max Height	Center Grvty	Area IntgP
1	Gaussian	0.11276	17.70457	0.00598	178.05282	60.60439
2	Gaussian	0.0733	28.36939	0.00244	167.05661	39.39561

Figure 5.S11. Gaussian peak fitting of 2.80 mg/m^2 PVP–rGO sample

The Gaussian peak fit of the 3.84 mg/m^2 sample is shown in Figure 5.S12. The area under the bulk-like peak (ΔC_{comp}) was estimated as 0.095.

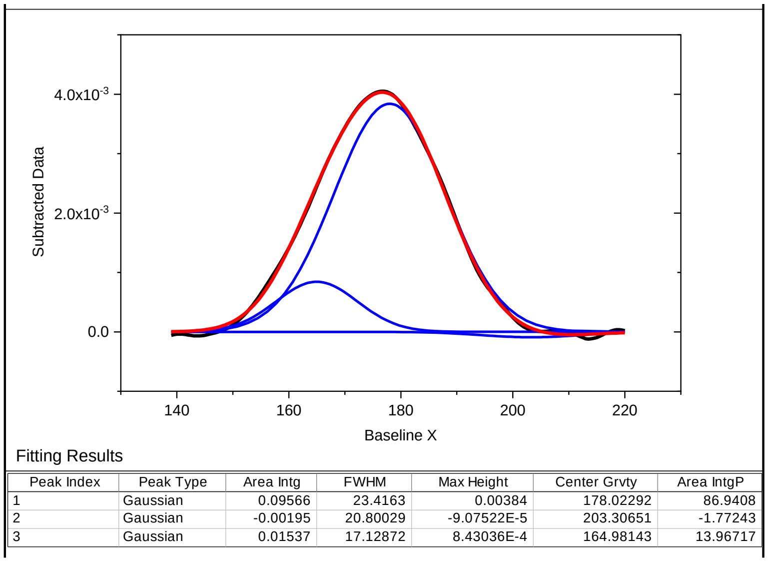

Fitting Results

Peak Index	Peak Type	Area Intg	FWHM	Max Height	Center Grvty	Area IntgP
1	Gaussian	0.09566	23.4163	0.00384	178.02292	86.9408
2	Gaussian	-0.00195	20.80029	-9.07522E-5	203.30651	-1.77243
3	Gaussian	0.01537	17.12872	8.43036E-4	164.98143	13.96717

Figure 5.S12. Gaussian peak fitting of 3.84 mg/m^2 PVP–rGO sample

CHAPTER VI

AMINOPROPYL ISOBUTYL POSS (POSS–NH_2) GRAFTED GRAPHENE OXIDE (GO)

6.1. INTRODUCTION

Graphene oxide (GO) is a prominent additive that has revolutionized the area of polymer composites over the last decade. The key factor behind the success of graphene-based additives is the large specific area of individual graphene sheets. The surface area plays a key role when determining the overall strength of the interphase interactions between the additive and the resin and ultimately affects the mechanical and thermal properties of the composite. The performance of GO with the resin heavily depends on the efficiency of dispersion with minimum coagulation and macro phase separation. Therefore, continuous efforts are being made by scientists to improve the dispersion efficiency of GO in moderately hydrophobic resins such as epoxy. It can be recognized that the poor dispersion of GO in resins is mainly due to attractions between the graphene sheets. Hydrophobic modification of GO is a major way to reduce the interactions between graphene sheets while promoting interactions with the resin. Therefore, there is high demand for a hydrophobically modified graphene-based material with expanded graphene sheets that can easily be dispersed in polymers and resins.

Aminopropyl isobutyl polyhedral oligomeric silsesquioxane (POSS–NH_2) is a hybrid inorganic and organic molecule that is surrounded by seven isobutyl groups and one propylamine group. For several reasons, the POSS–NH_2 molecule has good potential as a modification agent for GO. First, the isobutyl of POSS–NH_2 molecules provide essential hydrophobic characteristics when bonded to the GO for important interactions with hydrophobic polymers. Second, grafting POSS–NH_2 to GO can reduce the interlayer interactions and ultimately exfoliate the graphene sheets. Finally, the silicon cage confers several other advantages to the resin, such as thermal stability, flame retardancy,[1,2] and improved mechanical properties.[3]

Here we report the synthesis of a GO/POSS–NH_2 hybrid material for use as an additive in commercially available epoxy resins. First, POSS–NH_2 molecules were grafted to GO using the 1-ethyl-3-(3-dimethyl aminopropyl)-carbodiimide (EDC) and 4-dimethyl aminopyridine (DMAP) catalytic system. Then, the product was characterized using several analytical methods, including Fourier transform infrared (FTIR) spectroscopy, thermogravimetric analysis (TGA), and X-ray diffraction (XRD), to study the effects of the grafting reaction on the chemical and physical characteristics of the GO. The chemical characterization results for the 1 g reaction are discussed in the following sections.

6.2. EXPERIMENTAL

6.2.1. Synthesis of POSS–NH_2-grafted GO

A 40 g portion of 2.5% graphene oxide aqueous dispersion (1 g dry weight) was dispersed in 200 ml of THF, transferred to a 1 L round bottom flask, and stirred for 15 min with a magnetic stirrer. Then, 20 mg of DMAP and 1 g of POSS–NH_2 were added to the mixture at 10 min intervals. Finally, EDC was added to the mixture, and the reaction was conducted at 75 °C for 24 h with moderate stirring in an oil bath. After 24 h, the reaction vessel was cooled to room temperature, and 9 mL of ethylene diamine was added. The mixture was then further stirred for 30 min at room temperature. Finally, the product was filtered and washed with two 200 ml portions of THF and two 100 ml portions of acetone. The product was dried in a vacuum oven at room temperature for 4 h and 50 °C overnight before characterization.

6.2.2 Characterization of GO–POSS–NH_2

The chemical and thermal characterization of the additive was conducted with FTIR, XRF, XRD, TGA, and optical microscopy. The detailed characterization methods are mentioned in the materials and method section in chapter 4.

6.2.3. Dispersion analysis

Analysis of the dispersion characteristics of GO–POSS-NH_2 was carried out to check the hydrophobic characteristics of the GO–POSS-NH_2 additive. Briefly, 10 mg of additive was added to water and ultrasonicated for 5 min. Then, 10 mL of $CHCl_3$ was added to the vial and shaken vigorously for 10 s. The sample was allowed to settle for 10 min, and the photographs were taken. For the dispersion analysis, 10 mg of additive was added to a 25 ml glass vial, followed by 10 mL of solvent. Next, the dispersion was sonicated for 5 min to enhance the dispersion of the additive.

6.3. RESULTS AND DISCUSSION

As illustrated in Figure 6.1. the amidation reaction was carried out between the carboxylic acid group of GO and the amine groups of POSS–NH_2 in the presence of the EDC/DMAP catalytic system. The GO was pale yellow aqueous dispersion, and the product was observed to be black dispersion.

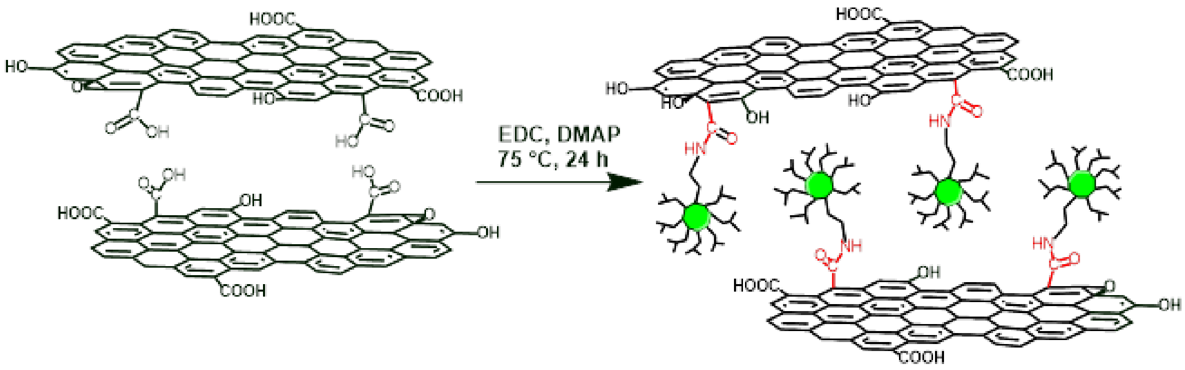

Figure 6.1. Schematic representation of synthetic route from GO to GO–POSS-NH_2 hybrid material.

6.3.1. FTIR spectroscopy

The amidation reaction was confirmed by FTIR spectroscopy. The FTIR spectra of POSS–NH_2, GO, and the GO–POSS-NH_2 nanomaterial are shown in Figure 6.2. For POSS–NH_2, the intense peaks at 1085 cm^{-1} can be ascribed to the stretching vibrations of the Si–O–Si of the silicon cage. The C-N and C-H stretching bands of the POSS–NH_2 can be found at 1228 and 2869 cm^{-1}, respectively.[4,5] The chemical structure of GO can be characterized using the appearance of the peaks at 1715 and 1550 cm^{-1} that are assigned to the C=O stretch of carboxylic acid groups and the C=C bonds in GO, respectively.[6]

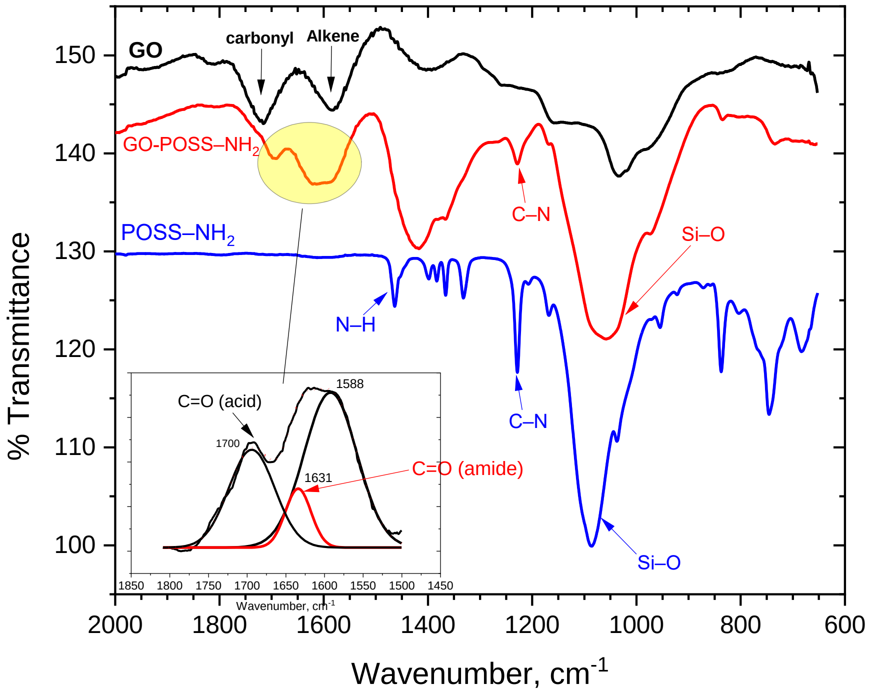

Figure 6.2. FTIR spectra of GO, POSS–NH_2, and GO/POSS–NH_2 hybrid material. The full FTIR spectra are shown in Supporting Information.

The structural change that can occur during the reaction is the formation of a covalent bond between the nitrogen atoms of POSS–NH_2 and the carbon atoms of the carboxylic acid groups in GO. The formation of an amide bond results in the appearance of new carbonyl stretches with resonances closer to those of the carbonyl groups of carboxylic acid. The carbonyl peak of the carboxylic acid group was broadened due to the overlapping with the amide carbonyl stretches. The carbonyl region of the FTIR spectrum of additive was analyzed using Origin software using the gaussian function and shown in Figure 6.2 inset. The objective of the fitting is to resolve the amide stretching[7] band and the carboxylic acid carbonyl band in the GO–POSS-NH_2 FTIR spectrum. The results obtained from the fitting are tabulated in Table 6.1 which shows the list of resolved peaks in the carbonyl region of the additive. Based on the analysis, the formation of amide linkages between POSS-NH_2 and GO were confirmed.

Table 6.1 The list of resonances in the “carbonyl region“

Type of bond	Wavenumber, cm^{-1}	FWHM*
C=O (acid)	1699	80
C=O (amide)	1634	39
C=C (alkene)	1592	70

*FWHM is the full width at half maximum

According to the analysis, the residual carbonyl stretching of the acids group can be observed in 1699 cm^{-1}. The sharp small intensity peak at 1634 cm^{-1} can be attributed to the newly formed amide bond. The peak at 1592 cm^{-1} can be assigned to the alkene stretching vibrations of GO.

6.3.2. Thermogravimetric analysis

The thermal properties of the material and the amount of POSS-NH_2 grafted on the GO surface were studied using TGA analysis. The thermograms of GO–POSS-NH_2 and reactants are shown in Figure 6.3. In the GO–POSS-NH_2 hybrid material, the mass fraction of silica was estimated from TGA as 4.6–5%, based on the final residue being SiO_2. The mass percentage of POSS-NH_2 grafted onto the GO in the composite was calculated as ~13%.

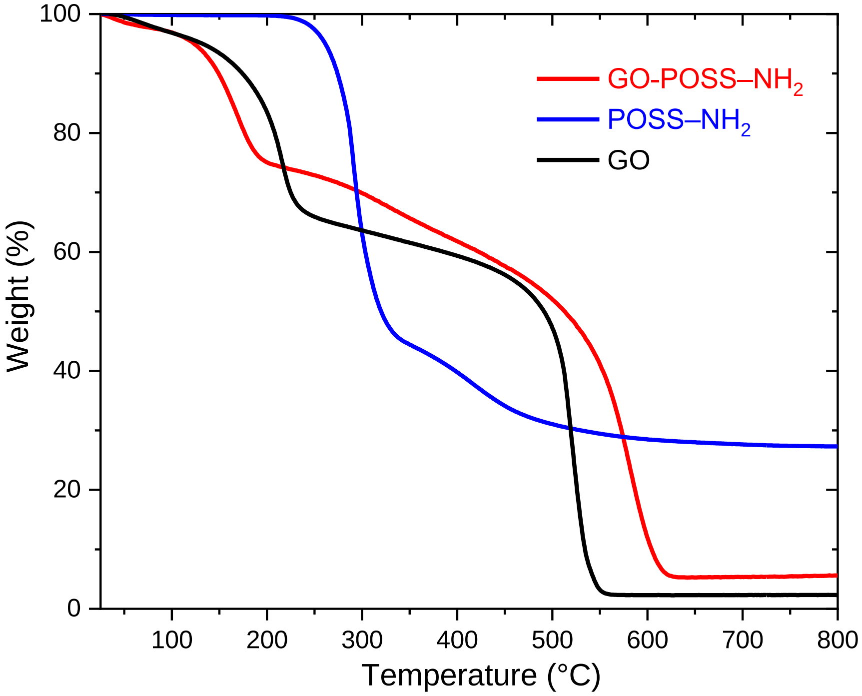

Figure 6.3. TGA thermograms of GO, POSS-NH_2, and the GO-POSS-NH_2 hybrid material

6.3.3. Dispersion of GO–POSS-NH_2 in different solvents

As illustrated in Figure 6.4a, the reaction of POSS–NH_2 with GO changed the physical and chemical characteristics of the GO. The initial color of the GO dispersion in water was pale yellow, which changed to black dispersion after the grafting reaction. Initially, the GO showed good dispersion in water due to its hydrophilic characteristics (Figure 6.4a. Right vial). After the modification, the GO-POSS–NH_2 additive was transferred to the chloroform phase (Figure 6.4a. left vial) due to its more hydrophobic nature. This suggests a change in the chemical nature of GO after the grafting of POSS-NH_2.

The dispersion of material in different solvents shows clear evidence of the hydrophobic modification of GO by POSS–NH_2. The dispersion characteristics of the GO–POSS-NH_2 additive were evaluated by dispersing the additive in different solvents, as shown in Figures 6.4b and 6.4c. The solvents used for the study were pentane (most hydrophobic), toluene, tetrahydrofuran

(THF), ethanol, and water (most hydrophilic). A picture taken just after 5 min of ultra-sonication of the material in each solvent is shown in Figure 6.4b. After the reaction, the GO-POSS–NH_2 material dispersed in pentane and toluene. In contrast, the pristine GO shows decent dispersion and stability in hydrophilic solvents such as water and IPA. However, very poor dispersion was observed in pentane. As can be seen in Figure 6.4 c), GO remained at the bottom of the glass vial without dispersion in the pentane.

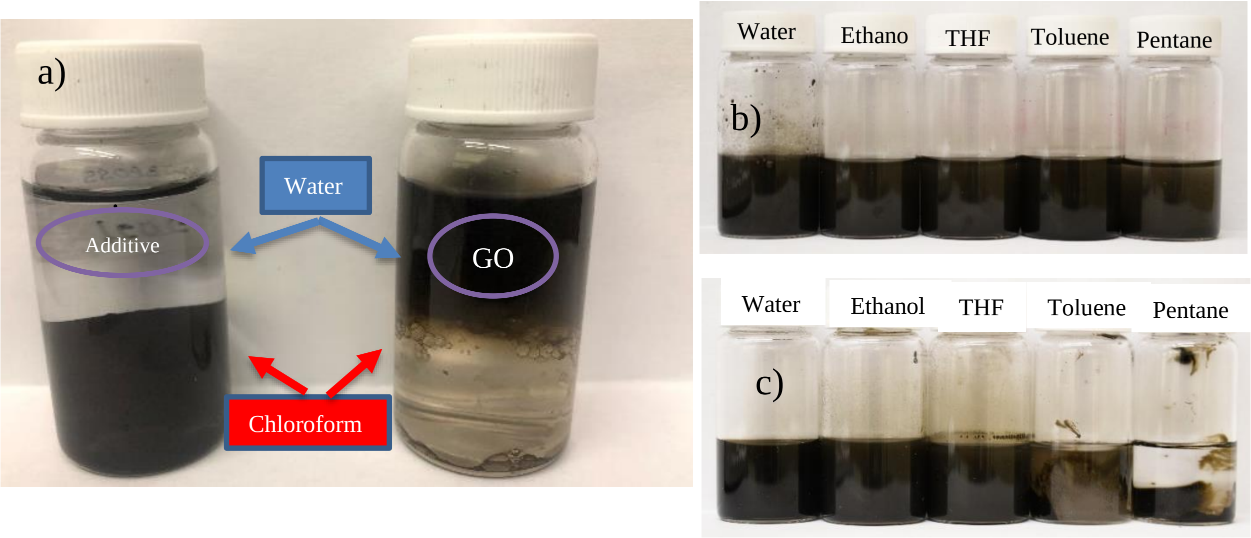

Figure 6.4. a) The change of solubility of GO alone (left) from water to chloroform after reaction with POSS-NH_2 b) dispersion of GO–POSS-NH_2 additive (right) c) dispersion of GO in various solvents.

6.3.4. Contact angle

The water contact angles on the pristine GO and GO–POSS-NH_2 were carried out to evaluate the baseline effect of the POSS-NH_2 grafting on the hydrophilic characteristics of the GO. The contact angle of pristine GO could be not measured using the pellet method due to the relatively fast absorption of water into the pellet. The GO–POSS–NH_2 was shown to have significantly more hydrophobicity compared to GO. As illustrated in Figure 6.5 the water droplet on the pellet surface was stable and measured as 98°.

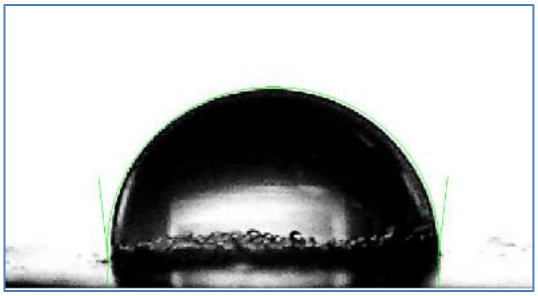

Figure 6.5. The picture of the water droplet on the GO-POSS-NH_2 surface

6.3.5. Dispersion of GO–POSS–NH_2 in epoxy

The goal of synthesizing the GO–POSS-NH_2 was to increase the dispersion of GO in hydrophobic polymers and solvents. Therefore, the modified additive was dispersed in epoxy resins to evaluate its dispersion characteristics. To test the ease of dispersion, the additive was dispersed in EPON 828 by manual mixing for 1 min, followed by 1 and 10 min ultrasonication. Then about 2 mL of resin was spread on a white sheet, and photographs were taken, as shown in Figure 6.6. As illustrated in the picture, the hand-mixed dispersion shows black particles that are not dispersed in the resin. However, once the dispersion is ultrasonicated, efficient dispersion of the additive was observed in the resin.

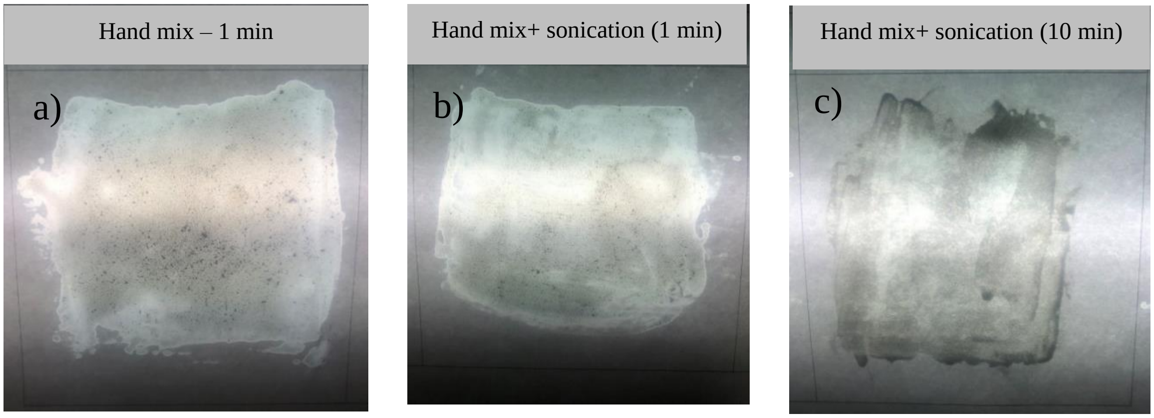

Figure 6.6. The dispersion of GO–POSS-NH_2 additive in epoxy resin

6.4. FUTURE WORK

The dispersion characteristics of the material in different resin systems and the scale-up of the product need to be studied. Also, the effect of additives on the mechanical properties of resin will be evaluated using an Instron and dynamic mechanical analyzer.

6.5. REFERENCES

1. Tang, C.; Yan, H.; Li, S.; Li, M.; Chen, Z., Novel phosphorus-containing polyhedral oligomeric silsesquioxane functionalized Graphene oxide: preparation and its performance on the mechanical and flame-retardant properties of bismaleimide composite. *Journal of Polymer Research* **2017,** *24* (10).

2. Qu, L.; Sui, Y.; Zhang, C.; Li, P.; Dai, X.; Xu, B.; Fang, D., POSS-functionalized graphene oxide hybrids with improved dispersive and smoke-suppressive properties for epoxy flame-retardant application. *European Polymer Journal* **2020,** *122*.

3. Jiang, D.; Xing, L.; Liu, L.; Yan, X.; Guo, J.; Zhang, X.; Zhang, Q.; Wu, Z.; Zhao, F.; Huang, Y.; Wei, S.; Guo, Z., Interfacially reinforced unsaturated polyester composites by chemically grafting different functional POSS onto carbon fibers. *Journal of Materials Chemistry A* **2014,** *2* (43), 18293-18303.

4. Vijayakumar, V.; Son, T. Y.; Kim, H. J.; Nam, S. Y., A facile approach to fabricate poly(2,6-dimethyl-1,4-phenylene oxide) based anion exchange membranes with extended alkaline stability and ion conductivity for fuel cell applications. *Journal of Membrane Science* **2019,** *591*, 1-11.

5. Zhang, X.; Ma, R.; Du, A.; Liu, Q.; Fan, Y.; Zhao, X.; Wu, J.; Cao, X., Corrosion resistance of organic coating based on polyhedral oligomeric silsesquioxane-functionalized graphene oxide. *Applied Surface Science* **2019,** *484*, 814-824.

6. Oliveira, A. E. F.; Braga, G. B.; Tarley, C. R. T.; Pereira, A. C., Thermally reduced graphene oxide: synthesis, studies and characterization. *Journal of Materials Science* **2018,** *53* (17), 12005-12015.

7. Yu, W.; Fu, J.; Dong, X.; Chen, L.; Shi, L., A graphene hybrid material functionalized with POSS: synthesis and applications in low-dielectric epoxy composites. *Composites Science and Technology* **2014,** *92*, 112-119.

6.6. SUPPORTING INFORMATION

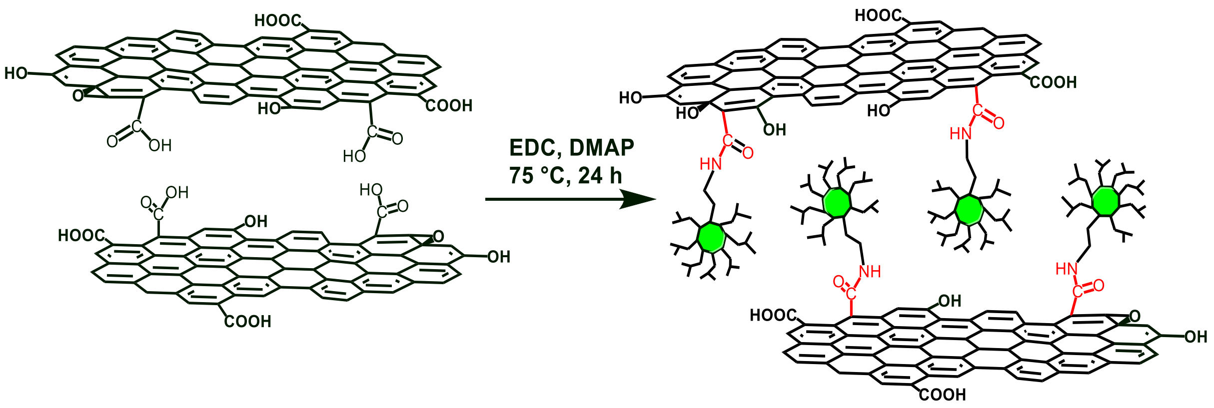

Contents:

6.S1. FITR SPECTRA OF GO, POSS-NH_2 AND GO-POSS-NH_2

The ATR-FTIR spectroscopy was used to identify the covalent bond between GO and POSS-NH_2 molecules. The full FTIR spectra of composites are shown in Figure 6.S1.

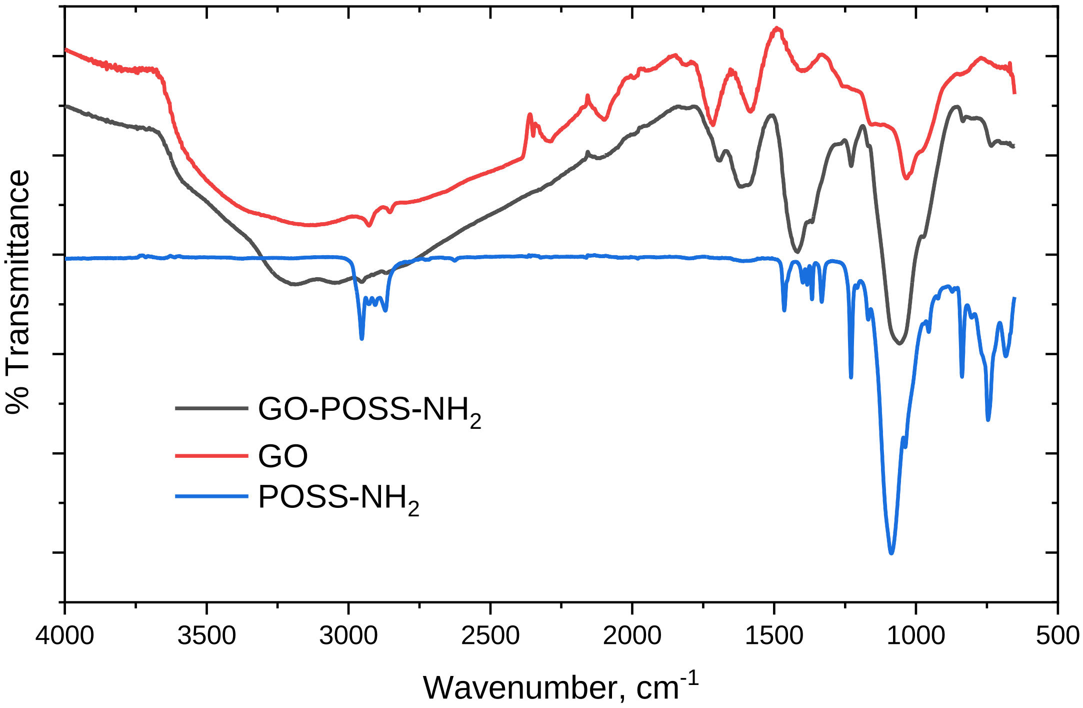

Figure 6.S1. Full FTIR spectra of the GO, POSS-NH_2, and GO-POSS-NH_2

REFERENCES

1. Hsissou, R.; Seghiri, R.; Benzekri, Z.; Hilali, M.; Rafik, M.; Elharfi, A., Polymer composite materials: A comprehensive review. Composite Structures 2021, 262.

2. Baidya, M.; Mayr, H., Nucleophilicities and carbon basicities of DBU and DBN. Chemical Communications 2008, (15), 1792-4.

3. Altin Karataş, M.; Gökkaya, H., A review on machinability of carbon fiber reinforced polymer (CFRP) and glass fiber reinforced polymer (GFRP) composite materials. Defence Technology 2018, 14 (4), 318-326.

4. Beck, M.; Jekle, M.; Becker, T., Starch re-crystallization kinetics as a function of various cations. Starch - Stärke 2011, 63 (12), 792-800.

5. Liu, P.; Yu, L.; Wang, X.; Li, D.; Chen, L.; Li, X., Glass transition temperature of starches with different amylose/amylopectin ratios. Journal of Cereal Science 2010, 51 (3), 388-391.

6. Le Corre, D.; Bras, J.; Dufresne, A., Starch Nanoparticles: A Review. Biomacromolecules 2010, 11 (5), 1139-1153.

7. Zhang, Z.; Macquarrie, D. J.; Clark, J. H.; Matharu, A. S., Chemical modification of starch and the application of expanded starch and its esters in hot melt adhesive. RSC Advances 2014, 4 (79), 41947-41955.

8. Imberty, A.; Chanzy, H.; Pérez, S.; Bulèon, A.; Tran, V., The double-helical nature of the crystalline part of A-starch. Journal of Molecular Biology 1988, 201 (2), 365-378.

9. Lv, X.; Hong, Y.; Zhou, Q.; Jiang, C., Structural features and digestibility of corn starch with different amylose content. Frontiers in Nutrition 2021, 8 (263).

10. Palanisamy, C. P.; Cui, B.; Zhang, H.; Jayaraman, S.; Kodiveri Muthukaliannan, G., A Comprehensive review on corn starch-based nanomaterials: properties, simulations, and applications. Polymers (Basel) 2020, 12 (9).

11. Wang, S.; Li, C.; Copeland, L.; Niu, Q.; Wang, S., Starch retrogradation: A comprehensive review. Comprehensive Reviews in Food Science and Food Safety 2015, 14 (5), 568-585.

12. Buléon, A.; Colonna, P.; Planchot, V.; Ball, S., Starch granules: structure and biosynthesis. International Journal of Biological Macromolecules 1998, 23 (2), 85-112.

13. Harding, S. E.; Adams, G. G.; Gillis, R. B., Molecular weight analysis of starches: Which technique? Starch - Stärke 2016, 68 (9-10), 846-853.

14. Mua, J. P.; Jackson, D. S., Fine structure of corn amylose and amylopectin fractions with various molecular weights. Journal of Agricultural and Food Chemistry 1997, 45 (10), 3840-3847.

15. Jiang, T.; Duan, Q.; Zhu, J.; Liu, H.; Yu, L., Starch-based biodegradable materials: Challenges and opportunities. Advanced Industrial and Engineering Polymer Research 2020, 3 (1), 8-18.

16. Hung, P.-y.; Lau, K.-t.; Fox, B.; Hameed, N.; Jia, B.; Lee, J. H., Effect of graphene oxide concentration on the flexural properties of CFRP at low temperature. Carbon 2019, 152, 556-564.

17. Saeb, M. R.; Bakhshandeh, E.; Khonakdar, H. A.; Mader, E.; Scheffler, C.; Heinrich, G., Cure kinetics of epoxy nanocomposites affected by MWCNTs functionalization: a review. Scientific World Journal 2013, 2013, 703708.

18. Salavagione, H. J.; Martínez, G.; Gómez, M. A., Synthesis of poly(vinyl alcohol)/reduced graphite oxide nanocomposites with improved thermal and electrical properties. Journal of Materials Chemistry 2009, 19 (28).

19. Kuila, T.; Bose, S.; Hong, C. E.; Uddin, M. E.; Khanra, P.; Kim, N. H.; Lee, J. H., Preparation of functionalized graphene/linear low density polyethylene composites by a solution mixing method. Carbon 2011, 49 (3), 1033-1037.

20. Izmar, M. H.; Afiq, M. M.; Azura, A. R., Effects of different additions of sago starch filler on physical and biodegradation properties of pre-vulcanized NR latex composites. Composites Part B: Engineering 2012, 43 (7), 2746-2750.

21. Roy, S. B.; Ramaraj, B.; Shit, S. C.; Nayak, S. K., Polypropylene and potato starch biocomposites: Physicomechanical and thermal properties. Journal of Applied Polymer Science 2011, 120 (5), 3078-3086.

22. Khan, M. A.; Khan, R. A.; Haydaruzzaman; Ghoshal, S.; Siddiky, M. N. A.; Saha, M., Study on the physico-mechanical properties of starch-treated jute Yarn-reinforced polypropylene composites: Effect of gamma radiation. Polymer-Plastics Technology and Engineering 2009, 48 (5), 542-548.

23. Lu, X. L.; Du, F. G.; Ge, X. C.; Xiao, M.; Meng, Y. Z., Biodegradability and thermal stability of poly(propylene carbonate)/starch composites. J Biomed Mater Res A 2006, 77 (4), 653-8.

24. Wang, X. L.; Li, R. K. Y.; Cao, Y. X.; Meng, Y. Z., Essential work of fracture analysis for starch filled poly(propylene carbonate) composites. Materials & Design 2007, 28 (6), 1934-1939.

25. Joshi, S. S.; Mebel, A. M., Computational modeling of biodegradable blends of starch amylose and poly-propylene carbonate. Polymer 2007, 48 (13), 3893-3901.

26. Morantes, D.; Munoz, E.; Kam, D.; Shoseyov, O., Highly charged cellulose nanocrystals applied as a water treatment flocculant. Nanomaterials (Basel) 2019, 9 (2).

27. Trinh, B. M.; Mekonnen, T., Hydrophobic esterification of cellulose nanocrystals for epoxy reinforcement. Polymer 2018, 155, 64-74.

28. Hui, R.; Qi he, C.; Ming liang, F.; Qiong, X.; Guo qing, H., Preparation and properties of octenyl succinic anhydride modified potato starch. Food Chemistry 2009, 114 (1), 81-86.

29. Hu, Z.; Berry, R. M.; Pelton, R.; Cranston, E. D., One-Pot water-based hydrophobic surface modification of cellulose nanocrystals using plant polyphenols. ACS Sustainable Chemistry & Engineering 2017, 5 (6), 5018-5026.

30. Marefati, A.; Matos, M.; Wiege, B.; Haase, N. U.; Rayner, M., Pickering emulsifiers based on hydrophobically modified small granular starches Part II - Effects of modification on emulsifying capacity. Carbohydrate Polymers 2018, 201, 416-424.

31. Zerroukhi, A.; Jeanmaire, T.; Raveyre, C.; Ainser, A., Synthesis and characterization of hydrophobically modified starch by ring opening polymerization using imidazole as catalyst. Starch - Stärke 2012, 64 (8), 613-620.

32. Peng, S. X.; Chang, H.; Kumar, S.; Moon, R. J.; Youngblood, J. P., A comparative guide to controlled hydrophobization of cellulose nanocrystals via surface esterification. Cellulose 2016, 23 (3), 1825-1846.

33. Habibi, Y., Key advances in the chemical modification of nanocelluloses. Chemical Society Reviews 2014, 43 (5), 1519-42.

34. Marefati, A.; Wiege, B.; Haase, N. U.; Matos, M.; Rayner, M., Pickering emulsifiers based on hydrophobically modified small granular starches – Part I: Manufacturing and physico-chemical characterization. Carbohydrate Polymers 2017, 175, 473-483.

35. Xiong, Z.; Ma, S.; Fan, L.; Tang, Z.; Zhang, R.; Na, H.; Zhu, J., Surface hydrophobic modification of starch with bio-based epoxy resins to fabricate high-performance polylactide composite materials. Composites Science and Technology 2014, 94, 16-22.

36. Xiong, Z.; Yang, Y.; Feng, J.; Zhang, X.; Zhang, C.; Tang, Z.; Zhu, J., Preparation and characterization of poly(lactic acid)/starch composites toughened with epoxidized soybean oil. Carbohydrate Polymers 2013, 92 (1), 810-816.

37. Belhassen, R.; Vilaseca, F.; Mutjé, P.; Boufi, S., Thermoplasticized starch modified by reactive blending with epoxidized soybean oil. Industrial Crops and Products 2014, 53, 261-267.

38. Tratnik, N.; Kuo, P.-Y.; Tanguy, N. R.; Gnanasekar, P.; Yan, N., Biobased epoxidized atarch wood adhesives: Effect of amylopectin and amylose content on adhesion properties. ACS Sustainable Chemistry & Engineering 2020, 8 (49), 17997-18005.

39. Williams, D. B.; Lawton, M., Aluminium triflate: a remarkable Lewis acid catalyst for the ring opening of epoxides by alcohols. Organic Biomolecular Chemistry 2005, 3 (18), 3269-72.

40. Hansen, T.; Vermeeren, P.; Haim, A.; van Dorp, M. J. H.; Codée, J. D. C.; Bickelhaupt, F. M.; Hamlin, T. A., Regioselectivity of epoxide ring-openings via SN2 reactions under basic and acidic conditions. European Journal of Organic Chemistry 2020, 2020 (25), 3822-3828.

41. Payard, P. A.; Gu, Q.; Guo, W.; Wang, Q.; Corbet, M.; Michel, C.; Sautet, P.; Grimaud, L.; Wischert, R.; Pera-Titus, M., Direct Amination of Alcohols Catalyzed by Aluminum Triflate: An Experimental and Computational Study. Chemistry 2018, 24 (53), 14146-14153.

42. Gohain, M.; Marais, C.; Bezuidenhoudt, B. C. B., Al(OTf)3: an efficient recyclable catalyst for direct nucleophilic substitution of the hydroxy group of propargylic alcohols with carbon- and heteroatom-centered nucleophiles to construct C–C, C–O, C–N and C–S bonds. Tetrahedron Letters 2012, 53 (9), 1048-1050.

43. Bastola, K., Prasas; Vaidyanathan,Ranji,K; System and method for synthesis of POSS–starch derivatives as effective fillers for developing high performacnce composites. World 2015/143434 Al, 09-24-2015, 2015.

44. Williams, D. B. G.; Cullen, A., Al(OTf)3-mediated epoxide ring-opening reactions: toward piperazine-derived physiologically active products. The Journal of Organic Chemistry 2009, 74 (24), 9509-9512.

45. Wu, J.; Xia, H.-G., Tertiary amines as highly efficient catalysts in the ring-opening reactions of epoxides with amines or thiols in H2O: expeditious approach to β-amino alcohols and β-aminothioethers. Green Chemistry 2005, 7 (10), 708-710.

46. Baidya, M.; Kobayashi, S.; Brotzel, F.; Schmidhammer, U.; Riedle, E.; Mayr, H., DABCO and DMAP--why are they different in organocatalysis? Angew Chemie International Edition 2007, 46 (32), 6176-9.

47. Salmi, T.; Tolvanen, P.; Wärnå, J.; Mäki-Arvela, P.; Murzin, D.; Sorokin, A., Mathematical modeling of starch oxidation by hydrogen peroxide in the presence of an iron catalyst complex. Chemical Engineering Science 2016, 146, 19-25.

48. Łabanowska, M.; Bidzińska, E.; Pietrzyk, S.; Juszczak, L.; Fortuna, T.; Błoniarczyk, K., Influence of copper catalyst on the mechanism of carbohydrate radicals generation in oxidized potato starch. Carbohydrate Polymers 2011, 85 (4), 775-785.

49. Pietrzyk, S.; Juszczak, L.; Fortuna, T.; Ciemniewska, A., Effect of the oxidation level of corn starch on its acetylation and physicochemical and rheological properties. Journal of Food Engineering 2014, 120, 50-56.

50. Ferry, J. D., Viscoelastic Properties of Polymers. John Wiley & Sons, Inc.: New York, 1980.

51. Ausili, A.; Sánchez, M.; Gómez-Fernández, J., Attenuated total reflectance infrared spectroscopy: A powerful method for the simultaneous study of structure and spatial orientation of lipids and membrane proteins. Biomedical Spectroscopy and Imaging 2015, 4, 159-70.

52. Menard, K. P., Dynamic mechanical analysis : a practical introduction. CRC Press LLC: Florida, 1999

53. Menard, K. P., & Menard, N. (2020), Dynamic Mechanical Analysis 3rd edition ed.; CRC press.

54. Sadrykia, F.; Arsalani, N., Preparation and characterization of hydrogel nanocomposites based on oxidized starch and incompletely condensed polyhedral oligomeric silsesquioxanes. Procedia Materials Science 2015, 11, 531-535.

55. Marefati, A.; Matos, M.; Wiege, B.; Haase, N. U.; Rayner, M., Pickering emulsifiers based on hydrophobically modified small granular starches Part II - Effects of modification on emulsifying capacity. Carbohydrate Polymers 2018, 201, 416-424.

56. Trinh, B. M.; Mekonnen, T., Hydrophobic esterification of cellulose nanocrystals for epoxy reinforcement. Polymer 2018, 155, 64-74.

57. Xiong, Z.; Ma, S.; Fan, L.; Tang, Z.; Zhang, R.; Na, H.; Zhu, J., Surface hydrophobic modification of starch with bio-based epoxy resins to fabricate high-performance polylactide composite materials. Composites Science and Technology 2014, 94, 16-22.

58. Zerroukhi, A.; Jeanmaire, T.; Raveyre, C.; Ainser, A., Synthesis and characterization of hydrophobically modified starch by ring opening polymerization using imidazole as catalyst. Starch - Stärke 2012, 64 (8), 613-620.

59. Hu, Z.; Berry, R. M.; Pelton, R.; Cranston, E. D., One-Pot water-based hydrophobic surface modification of cellulose nanocrystals using plant polyphenols. ACS Sustainable Chemistry & Engineering 2017, 5 (6), 5018-5026.

60. Hui, R.; Qi he, C.; Ming liang, F.; Qiong, X.; Guo qing, H., Preparation and properties of octenyl succinic anhydride modified potato starch. Food Chemistry 2009, 114 (1), 81-86.

61. Peng, S. X.; Chang, H.; Kumar, S.; Moon, R. J.; Youngblood, J. P., A comparative guide to controlled hydrophobization of cellulose nanocrystals via surface esterification. Cellulose 2016, 23 (3), 1825-1846.

62. Habibi, Y., Key advances in the chemical modification of nanocelluloses. Chemical Society Reviews 2014, 43 (5), 1519-42.

63. Ojogbo, E.; Blanchard, R.; Mekonnen, T., Hydrophobic and Melt Processable Starch-Laurate Esters: Synthesis, Structure–Property Correlations. Journal of Polymer Science Part A: Polymer Chemistry 2018, 56 (23), 2611-2622.

64. Marefati, A.; Wiege, B.; Haase, N. U.; Matos, M.; Rayner, M., Pickering emulsifiers based on hydrophobically modified small granular starches – Part I: Manufacturing and physico-chemical characterization. Carbohydrate Polymers 2017, 175, 473-483.

65. Ghani, K.; Kiomarsipour, N.; Ranjbar, M., New high-efficiency protective coating containing glycidyl-POSS nanocage for improvement of solar cell electrical parameters. Journal of Nanostructures 2019, 9 (1), 103-111.

66. Rahman, M. M.; Filiz, V.; Khan, M. M.; Gacal, B. N.; Abetz, V., Functionalization of POSS nanoparticles and fabrication of block copolymer nanocomposite membranes for CO2 separation. Reactive and Functional Polymers 2015, 86, 125-133.

67. Arslan, I.; Tasdelen, M. A., POSS-based hybrid thermosets via photoinduced copper-catalyzed azide–alkyne cycloaddition click chemistry. Designed Monomers and Polymers 2016, 19 (2), 155-160.

68. Jiang, D.; Xing, L.; Liu, L.; Yan, X.; Guo, J.; Zhang, X.; Zhang, Q.; Wu, Z.; Zhao, F.; Huang, Y.; Wei, S.; Guo, Z., Interfacially reinforced unsaturated polyester composites by chemically grafting different functional POSS onto carbon fibers. Journal of Materials Chemistry A 2014, 2 (43), 18293-18303.

69. Zhang, R. L.; Gao, B.; Du, W. T.; Zhang, J.; Cui, H. Z.; Liu, L.; Ma, Q. H.; Wang, C. G.; Li, F. H., Enhanced mechanical properties of multiscale carbon fiber/epoxy composites by fiber surface treatment with graphene oxide/polyhedral oligomeric silsesquioxane. Composites Part A: Applied Science and Manufacturing 2016, 84, 455-463.

70. Bastola, K., Prasas; Vaidyanathan,Ranji,K; System and method for synthesis of POSS–starch derivatives as effective fillers for developing high performacnce composites. World 2015/143434 Al, 09-24-2015, 2015.

71. Zhang, Y. R.; Wang, X. L.; Zhao, G. M.; Wang, Y. Z., Preparation and properties of oxidized starch with high degree of oxidation. Carbohydrate Polymers 2012, 87 (4), 2554-2562.

72. Kavaliauskaite, R.; Klimaviciute, R.; Zemaitaitis, A., Factors influencing production of cationic starches. Carbohydrate Polymers 2008, 73 (4), 665-75.

73. Sedai, B. R.; Khatiwada, B. K.; Mortazavian, H.; Blum, F. D., Development of superhydrophobicity in fluorosilane-treated diatomaceous earth polymer coatings. Applied Surface Science 2016, 386, 178-186.

74. Luo, F.; Huang, Q.; Fu, X.; Zhang, L.; Yu, S., Preparation and characterisation of crosslinked waxy potato starch. Food Chemistry 2009, 115 (2), 563-568.

75. Liu, X.; Wang, Y.; Yu, L.; Tong, Z.; Chen, L.; Liu, H.; Li, X., Thermal degradation and stability of starch under different processing conditions. Starch - Stärke 2013, 65 (1-2), 48-60.

76. Stawski, D., New determination method of amylose content in potato starch. Food Chemistry 2008, 110 (3), 777-781.

77. Liu, Y.; Yang, L.; Ma, C.; Zhang, Y., Thermal behavior of sweet potato starch by non-isothermal thermogravimetric analysis. Materials (Basel, Switzerland) 2019, 12 (5), 699.

78. Karić, N.; Grzetic, J.; Đolić, M.; Kovacevic, T.; Pecić, L.; Radovanović, Ž.; Marinkovic, A., Preparation and properties of hydrogen peroxide oxidized starch for industrial use. Hemijska industrija 2020, 74, 25-36.

79. Rudnik, E.; Matuschek, G.; Milanov, N.; Kettrup, A., Thermalstability and degradation of starch derivatives. Journal of Thermal Analysis and Calorimetry 2006, 85 (2), 267-270.

80. Vanier, N. L.; El Halal, S. L. M.; Dias, A. R. G.; da Rosa Zavareze, E., Molecular structure, functionality and applications of oxidized starches: A review. Food Chemistry 2017, 221, 1546-1559.

81. Zhang, Z.; Macquarrie, D. J.; Clark, J. H.; Matharu, A. S., Chemical modification of starch and the application of expanded starch and its esters in hot melt adhesive. RSC Advances 2014, 4 (79), 41947-41955.

82. Lu, Y.; Zhang, S.; Geng, Z.; Zhu, K.; Zhang, M.; Na, R.; Wang, G., Hybrid formation of graphene oxide–POSS and their effect on the dielectric properties of poly(aryl ether ketone) composites. New Journal of Chemistry 2017, 41 (8), 3089-3096.

83. Divakaran, N.; Kale, M. B.; Senthil, T.; Mubarak, S.; Dhamodharan, D.; Wu, L.; Wang, J., Novel unsaturated polyester nanocomposites via Hybrid 3D POSS-modified graphene oxide reinforcement: electro-technical application perspective. Nanomaterials (Basel) 2020, 10 (2).

84. Sirin, H.; Turan, D.; Ozkoc, G.; Gurdag, S., POSS reinforced PET based composite fibers: "Effect of POSS type and loading level". Composites Part B: Engineering 2013, 53, 395-403.

85. Song, J.; Zhao, J.; Ding, Y.; Chen, G.; Sun, X.; Sun, D.; Li, Q., Effect of polyhedral oligomeric silsesquioxane on water sorption and surface property of Bis-GMA/TEGDMa composites. Journal of Applied Polymer Science 2012, 124 (4), 3334-3340.

86. Hirohara, T.; Kai, T.; Ohshita, J.; Kaneko, Y., Preparation of protic ionic liquids containing cyclic oligosiloxane frameworks. RSC Advances 2017, 7 (17), 10575-10582.

87. Ramírez, M. G. L.; Muniz, G. I. B. d.; Satyanarayana, K. G.; Tanobe, V.; Iwakiri, S., Preparation and characterization of biodegradable composites based on Brazilian cassava starch, corn starch and green coconut fibers. Matéria (Rio de Janeiro) 2010, 15 (2), 330-337.

88. Marinich, J. A.; Ferrero, C.; Jiménez-Castellanos, M. R., Graft copolymers of ethyl methacrylate on waxy maize starch derivatives as novel excipients for matrix tablets: Physicochemical and technological characterisation. European Journal of Pharmaceutics and Biopharmaceutics 2009, 72 (1), 138-147.

89. Kumar; Ganure, A.; Subudhi, b. b.; Shukla, S., Synthesis and characterization of pH sensitive ampiphillic new copolymer of methyl methacrylate grafted on modified starch: Influences of reaction variables on grafting parameters. International Journal of Pharmacy and Pharmaceutical Sciences 2014, 6, 868-880.

90. Dome, K.; Podgorbunskikh, E.; Bychkov, A.; Lomovsky, O., Changes in the crystallinity degree of starch having different types of crystal structure after mechanical pretreatment. Polymers (Basel) 2020, 12 (3).

91. Aradhana, R.; Mohanty, S.; Nayak, S. K., Comparison of mechanical, electrical and thermal properties in graphene oxide and reduced graphene oxide filled epoxy nanocomposite adhesives. Polymer 2018, 141, 109-123.

92. Zhang, M.; Yan, H.; Yuan, L.; Liu, C., Effect of functionalized graphene oxide with hyperbranched POSS polymer on mechanical and dielectric properties of cyanate ester composites. Royal Society of Chemistry Advances 2016, 6 (45), 38887-38896.

93. Zhang, R. L.; Gao, B.; Du, W. T.; Zhang, J.; Cui, H. Z.; Liu, L.; Ma, Q. H.; Wang, C. G.; Li, F. H., Enhanced mechanical properties of multiscale carbon fiber/epoxy composites by fiber surface treatment with graphene oxide/polyhedral oligomeric silsesquioxane. Composites Part A: Applied Science and Manufacturing 2016, 84, 455-463.

94. Tang, C.; Yan, H.; Li, S.; Li, M.; Chen, Z., Novel phosphorus-containing polyhedral oligomeric silsesquioxane functionalized Graphene oxide: preparation and its performance on the mechanical and flame-retardant properties of bismaleimide composite. Journal of Polymer Research 2017, 24 (10).

95. Ye, Y.; Zhang, D.; Liu, T.; Liu, Z.; Liu, W.; Pu, J.; Chen, H.; Zhao, H.; Li, X., Improvement of anticorrosion ability of epoxy matrix in simulate marine environment by filled with superhydrophobic POSS-GO nanosheets. Journal Hazard Materials 2019, 364, 244-255.

96. Xue, Y.; Liu, Y.; Lu, F.; Qu, J.; Chen, H.; Dai, L., Functionalization of graphene oxide with polyhedral oligomeric silsesquioxane (POSS) for multifunctional applications. Journal of Physical Chemistry Letters 2012, 3 (12), 1607-12.

97. Brodie, B. C., XIII. On the atomic weight of graphite. Philosophical Transactions of the Royal Society of London 1859, 149, 249-259.

98. Feicht, P.; Biskupek, J.; Gorelik, T. E.; Renner, J.; Halbig, C. E.; Maranska, M.; Puchtler, F.; Kaiser, U.; Eigler, S., Brodie's or Hummers' Method: Oxidation conditions determine the structure of graphene oxide. Chemistry 2019, 25 (38), 8955-8959.

99. Hummers, W. S.; Offeman, R. E., Preparation of graphitic oxide. Journal of the American Chemical Society 1958, 80 (6), 1339-1339.

100. Justh, N.; Berke, B.; László, K.; Szilágyi, I. M., Thermal analysis of the improved Hummers' synthesis of graphene oxide. Journal of Thermal Analysis and Calorimetry 2017, 131 (3), 2267-2272.

101. Dreyer, D. R.; Park, S.; Bielawski, C. W.; Ruoff, R. S., The chemistry of graphene oxide. Chemical Society Reviews 2010, 39 (1), 228-40.

102. Hofmann, U.; Holst, R., Über die Säurenatur und die Methylierung von Graphitoxyd. Berichte der deutschen chemischen Gesellschaft (A and B Series) 1939, 72 (4), 754-771.

103. Ruess, G.; Vogt, F., Höchstlamellarer Kohlenstoff aus Graphitoxyhydroxyd. Monatshefte für Chemie und verwandte Teile anderer Wissenschaften 1948, 78 (3), 222-242.

104. Scholz, W.; Boehm, H. P., Untersuchungen am graphitoxid. VI. betrachtungen zur struktur des graphitoxids. Zeitschrift für anorganische und allgemeine Chemie 1969, 369 (3-6), 327-340.

105. Lerf, A.; He, H.; Forster, M.; Klinowski, J., Structure of graphite oxide revisited. The Journal of Physical Chemistry B 1998, 102 (23), 4477-4482.

106. Szabó, T.; Berkesi, O.; Forgó, P.; Josepovits, K.; Sanakis, Y.; Petridis, D.; Dékány, I., Evolution of surface functional groups in a series of progressively oxidized graphite oxides. Chemistry of Materials 2006, 18 (11), 2740-2749.

107. Sun, L., Structure and synthesis of graphene oxide. Chinese Journal of Chemical Engineering 2019, 27 (10), 2251-2260.

108. Rourke, J. P.; Pandey, P. A.; Moore, J. J.; Bates, M.; Kinloch, I. A.; Young, R. J.; Wilson, N. R., The real graphene oxide revealed: stripping the oxidative debris from the graphene-like sheets. Angewandte Chemie International Edition English 2011, 50 (14), 3173-7.

109. Dimiev, A. M.; Alemany, L. B.; Tour, J. M., Graphene Oxide. Origin of acidity, its instability in water, and a new dynamic structural model. ACS Nano 2013, 7 (1), 576-588.

110. Johra, F. T.; Lee, J.-W.; Jung, W.-G., Facile and safe graphene preparation on solution based platform. Journal of Industrial and Engineering Chemistry 2014, 20 (5), 2883-2887.

111. Sheehan, J. C.; Hess, G. P., A New method of forming peptide bonds. Journal of the American Chemical Society 1955, 77 (4), 1067-1068.

112. Lutjen, A. B.; Quirk, M. A.; Barbera, A. M.; Kolonko, E. M., Synthesis of (E)-cinnamyl ester derivatives via a greener Steglich esterification. Bioorganic & Medicinal Chemistry 2018, 26 (19), 5291-5298.

113. Divakaran, N.; Kale, M. B.; Senthil, T.; Mubarak, S.; Dhamodharan, D.; Wu, L.; Wang, J., Novel unsaturated polyester nanocomposites via Hybrid 3D POSS-modified graphene oxide reinforcement: electro-technical application perspective. Nanomaterials (Basel) 2020, 10 (2).

114. Hu, L.; Jiang, P.; Bian, G.; Huang, M.; Haryono, A.; Zhang, P.; Bao, Y.; Xia, J., Effect of octa(aminopropyl) polyhedral oligomeric silsesquioxane (OapPOSS) functionalized graphene oxide on the mechanical, thermal, and hydrophobic properties of waterborne polyurethane composites. Journal of Applied Polymer Science 2017, 134 (6), 1-11.

115. Yu, W.; Fu, J.; Dong, X.; Chen, L.; Shi, L., A graphene hybrid material functionalized with POSS: synthesis and applications in low-dielectric epoxy composites. Composites Science and Technology 2014, 92, 112-119.

116. Kurakula, M.; Rao, G. S. N. K., Pharmaceutical assessment of polyvinylpyrrolidone (PVP): As excipient from conventional to controlled delivery systems with a spotlight on COVID-19 inhibition. J Drug Deliv Sci Technol 2020, 60, 102046-102046.

117. Chen, S.; Cheng, B.; Ding, C., Synthesis and characterization of Poly(vinyl pyrrolidone)/Reduced graphene oxide nanocomposite. Journal of Macromolecular Science, Part B 2015, 54 (4), 481-491.

118. Zou, R.; Su, L.; Zhang, L.; Hu, N.; Yue, D., Polyvinyl pyrrolidone grafted silica reinforced hydrogenated carboxylated nitrile latex film with improved mechanical properties. Composites Communications 2017, 6, 25-28.

119. Blum, F. D.; Young, E. N.; Smith, G.; Sitton, O. C., Thermal analysis of adsorbed poly(methyl methacrylate) on silica. Langmuir 2006, 22 (10), 4741-4744.

120. Khatiwada, B. K.; Blum, F. D., Tightly bound PMMA on silica has reduced heat capacities. Langmuir 2019, 35 (35), 11482-11490.

121. Simon, S. L., Temperature-modulated differential scanning calorimetry: theory and application. Thermochimica Acta 2001, 374 (1), 55-71.

122. Thomas, L. C., Modulated DSC® Basics; Calculation and calibration of MDSC® signals. TA instruments.

123. Gill, F. S.; Uniyal, D.; Prasad, B.; Saluja, S.; Mishra, A.; Bachheti, R. K.; Juyal, S., Investigation of increased electrical conductivity by rGO in rGO/PVDF/PMMA/PTFE nanocomposites. Journal of Molecular Structure 2022, 1267, 133541.

124. Xue, Y.; Liu, Y.; Lu, F.; Qu, J.; Chen, H.; Dai, L., Functionalization of graphene oxide with polyhedral oligomeric silsesquioxane (POSS) for multifunctional applications. Journal of Physical Chemistry Letters 2012, 3 (12), 1607-12.

125. Tang, J.; Zhou, H.; Liang, Y.; Shi, X.; Yang, X.; Zhang, J., Properties of graphene oxide/epoxy resin composites. Journal of Nanomaterials 2014, 2014, 1-5.

126. Yu, W.; Fu, J.; Dong, X.; Chen, L.; Shi, L., A graphene hybrid material functionalized with POSS: synthesis and applications in low-dielectric epoxy composites. Composites Science and Technology 2014, 92, 112-119.

127. Smith, A. T.; LaChance, A. M.; Zeng, S.; Liu, B.; Sun, L., Synthesis, properties, and applications of graphene oxide/reduced graphene oxide and their nanocomposites. Nano Materials Science 2019, 1 (1), 31-47.

128. Shi, Y.; Yu, B.; Zheng, Y.; Yang, J.; Duan, Z.; Hu, Y., Design of reduced graphene oxide decorated with DOPO-phosphanomidate for enhanced fire safety of epoxy resin. Journal of Colloid and Interface Science 2018, 521, 160-171.

129. Li, W.; Huang, W.; Kang, Y.; Gong, Y.; Ying, Y.; Yu, J.; Zheng, J.; Qiao, L.; Che, S., Fabrication and investigations of G-POSS/cyanate ester resin composites reinforced by silane-treated silica fibers. Composites Science and Technology 2019, 173, 7-14.

130. Jiang, D.; Xing, L.; Liu, L.; Yan, X.; Guo, J.; Zhang, X.; Zhang, Q.; Wu, Z.; Zhao, F.; Huang, Y.; Wei, S.; Guo, Z., Interfacially reinforced unsaturated polyester composites by chemically grafting different functional POSS onto carbon fibers. Journal of Materials Chemistry A 2014, 2 (43), 18293-18303.

131. Raimondo, M.; Guadagno, L.; Speranza, V.; Bonnaud, L.; Dubois, P.; Lafdi, K., Multifunctional graphene/POSS epoxy resin tailored for aircraft lightning strike protection. Composites Part B: Engineering 2018, 140, 44-56.

132. Yadav, S. K.; Mahapatra, S. S.; Yoo, H. J.; Cho, J. W., Synthesis of multi-walled carbon nanotube/polyhedral oligomeric silsesquioxane nanohybrid by utilizing click chemistry. Nanoscale Research Letters 2011, 6 (1), 122.

133. Zhang, M.; Yan, H.; Yuan, L.; Liu, C., Effect of functionalized graphene oxide with hyperbranched POSS polymer on mechanical and dielectric properties of cyanate ester composites. Royal Society of Chemistry Advances 2016, 6 (45), 38887-38896.

134. Zhang, R. L.; Gao, B.; Du, W. T.; Zhang, J.; Cui, H. Z.; Liu, L.; Ma, Q. H.; Wang, C. G.; Li, F. H., Enhanced mechanical properties of multiscale carbon fiber/epoxy composites by fiber surface treatment with graphene oxide/polyhedral oligomeric silsesquioxane. Composites Part A: Applied Science and Manufacturing 2016, 84, 455-463.

135. Tang, C.; Yan, H.; Li, S.; Li, M.; Chen, Z., Novel phosphorus-containing polyhedral oligomeric silsesquioxane functionalized Graphene oxide: preparation and its performance on the mechanical and flame-retardant properties of bismaleimide composite. Journal of Polymer Research 2017, 24 (10).

136. Ye, Y.; Zhang, D.; Liu, T.; Liu, Z.; Liu, W.; Pu, J.; Chen, H.; Zhao, H.; Li, X., Improvement of anticorrosion ability of epoxy matrix in simulate marine environment by filled with superhydrophobic POSS-GO nanosheets. Journal Hazard Materials 2019, 364, 244-255.

137. Ghani, K.; Kiomarsipour, N.; Ranjbar, M., New high-efficiency protective coating containing glycidyl-POSS nanocage for improvement of solar cell electrical parameters. Journal of Nanostructures 2019, 9 (1), 103-111.

138. Rahman, M. M.; Filiz, V.; Khan, M. M.; Gacal, B. N.; Abetz, V., Functionalization of POSS nanoparticles and fabrication of block copolymer nanocomposite membranes for CO2 separation. Reactive and Functional Polymers 2015, 86, 125-133.

139. Arslan, I.; Tasdelen, M. A., POSS-based hybrid thermosets via photoinduced copper-catalyzed azide–alkyne cycloaddition click chemistry. Designed Monomers and Polymers 2016, 19 (2), 155-160.

140. Zhang, X.; Ma, R.; Du, A.; Liu, Q.; Fan, Y.; Zhao, X.; Wu, J.; Cao, X., Corrosion resistance of organic coating based on polyhedral oligomeric silsesquioxane-functionalized graphene oxide. Applied Surface Science 2019, 484, 814-824.

141. Vijayakumar, V.; Son, T. Y.; Kim, H. J.; Nam, S. Y., A facile approach to fabricate poly(2,6-dimethyl-1,4-phenylene oxide) based anion exchange membranes with extended alkaline stability and ion conductivity for fuel cell applications. Journal of Membrane Science 2019, 591, 1-11.

142. Rattana; Chaiyakun, S.; Witit-anun, N.; Nuntawong, N.; Chindaudom, P.; Oaew, S.; Kedkeaw, C.; Limsuwan, P., Preparation and characterization of graphene oxide nanosheets. Procedia Engineering 2012, 32, 759-764.

143. Chen, S.; Cheng, B.; Ding, C., Synthesis and characterization of Poly(vinyl pyrrolidone)/Reduced graphene oxide nanocomposite. Journal of Macromolecular Science, Part B 2015, 54 (4), 481-491.

144. Liao, W. H.; Yang, S. Y.; Hsiao, S. T.; Wang, Y. S.; Li, S. M.; Ma, C. C.; Tien, H. W.; Zeng, S. J., Effect of octa(aminophenyl) polyhedral oligomeric silsesquioxane functionalized graphene oxide on the mechanical and dielectric properties of polyimide composites. ACS Applied Material Interfaces 2014, 6 (18), 15802-12.

145. Kranauskaitė, I.; Macutkevič, J.; Borisova, A.; Martone, A.; Zarrelli, M.; Selskis, A.; Aniskevich, A.; Banys, J., Enhancing electrical conductivity of multiwalled carbon

nanotube/epoxy composites by graphene nanoplatelets. Lithuanian Journal of Physics 2018, 57 (4), 232-242.

146. Force Tefo, T.; Moloto, M. J.; Nyangiwe, N.; Khenfouch, M.; Maaza, M.; Kotsedi, L.; Dikio, E., Synthesis and Characterization of Graphene Thin Films via Hummer's Method. 2012.

147. Aradhana, R.; Mohanty, S.; Nayak, S. K., Comparison of mechanical, electrical and thermal properties in graphene oxide and reduced graphene oxide filled epoxy nanocomposite adhesives. Polymer 2018, 141, 109-123.

148. Xue, G.; Zhang, B.; Xing, J.; Sun, M.; Zhang, X.; Li, J.; Wang, L.; Liu, C., A facile approach to synthesize in situ functionalized graphene oxide/epoxy resin nanocomposites: mechanical and thermal properties. Journal of Materials Science 2019, 54 (22), 13973-13989.

149. Hu, L.; Jiang, P.; Bian, G.; Huang, M.; Haryono, A.; Zhang, P.; Bao, Y.; Xia, J., Effect of octa(aminopropyl) polyhedral oligomeric silsesquioxane (OapPOSS) functionalized graphene oxide on the mechanical, thermal, and hydrophobic properties of waterborne polyurethane composites. Journal of Applied Polymer Science 2017, 134 (6), 1-11.

150. Yin, B.; Wang, J.; Jia, H.; He, J.; Zhang, X.; Xu, Z., Enhanced mechanical properties and thermal conductivity of styrene–butadiene rubber reinforced with polyvinylpyrrolidone-modified graphene oxide. Journal of Materials Science 2016, 51 (12), 5724-5737.

151. Fontana, B. J.; Thomas, J. R., The configuration of adsorbed alkyl methacrylate polymers by infrared and sedimentation studies. The Journal of Physical Chemistry 1961, 65 (3), 480-487.

152. Khatiwada, B. K.; Hetayothin, B.; Blum, F. D., Thermal properties of PMMA on silica using temperature-modulated differential scanning calorimetry. Macromolecular Symposia 2013, 327 (1), 20-28.

153. Maddumaarachchi, M.; Blum, F. D., Thermal analysis and FT-IR studies of adsorbed poly(ethylene-stat-vinyl acetate) on silica. Journal of Polymer Science Part B: Polymer Physics 2014, 52 (10), 727-736.

154. Chen, S.; Cheng, B.; Ding, C., Synthesis and characterization of Poly(vinyl pyrrolidone)/Reduced graphene oxide nanocomposite. Journal of Macromolecular Science, Part B 2015, 54 (4), 481-491.

155. Ma, X.; Xie, G.; Su, Y.; Du, H.; Xie, T.; Jiang, Y., Polyvinylpyrrolidone/graphene oxide thin films coated on quartz crystal microbalance electrode for NH3 detection at room temperature. Science China Technological Sciences 2016, 59 (9), 1377-1382.

156. Li, X.; Deng, H.; Li, Z.; Xiu, H.; Qi, X.; Zhang, Q.; Wang, K.; Chen, F.; Fu, Q., Graphene/thermoplastic polyurethane nanocomposites: Surface modification of graphene through oxidation, polyvinyl pyrrolidone coating and reduction. Composites Part A: Applied Science and Manufacturing 2015, 68, 264-275.

157. Gill, F. S.; Uniyal, D.; Prasad, B.; Saluja, S.; Mishra, A.; Bachheti, R. K.; Juyal, S., Investigation of increased electrical conductivity by rGO in rGO/PVDF/PMMA/PTFE nanocomposites. Journal of Molecular Structure 2022, 1267, 133541.

158. Marami, G.; Nazari, S. A.; Faghidian, S. A.; Vakili-Tahami, F.; Etemadi, S., Improving the mechanical behavior of the adhesively bonded joints using RGO additive. International Journal of Adhesion and Adhesives 2016, 70, 277-286.

159. Chen, J.; Wu, J.; Ge, H.; Zhao, D.; Liu, C.; Hong, X., Reduced graphene oxide deposited carbon fiber reinforced polymer composites for electromagnetic interference shielding. Composites Part A: Applied Science and Manufacturing 2016, 82, 141-150.

160. Yang, B.; Wei, Y.; Liu, Q.; Luo, Y.; Qiu, S.; Shi, Z., Polyvinylpyrrolidone functionalized magnetic graphene-based composites for highly efficient removal of lead from wastewater. Colloids and Surfaces A: Physicochemical and Engineering Aspects 2019, 582, 123927.

161. Wu, X.; Field, R. W.; Wu, J. J.; Zhang, K., Polyvinylpyrrolidone modified graphene oxide as a modifier for thin film composite forward osmosis membranes. Journal of Membrane Science 2017, 540, 251-260.

162. Zhang, X.; Wang, J.; Jia, H.; Yin, B.; Ding, L.; Xu, Z.; Ji, Q., Polyvinyl pyrrolidone modified graphene oxide for improving the mechanical, thermal conductivity and solvent resistance properties of natural rubber. Royal Society of Chemistry Advances 2016, 6 (60), 54668-54678.

163. Zou, R.; Su, L.; Zhang, L.; Hu, N.; Yue, D., Polyvinyl pyrrolidone grafted silica reinforced hydrogenated carboxylated nitrile latex film with improved mechanical properties. Composites Communications 2017, 6, 25-28.

164. Fleer, G. J., Polymers at interfaces and in colloidal dispersions. Advances in Colloid and Interface Science 2010, 159 (2), 99-116.

165. Ploehn, H. J., Polymers at Interfaces. Journal of the American Chemical Society 1996, 118 (1), 297-298.

166. Blum, F. D., Glass Transition Behavior of PMMA Thin Films. Polymer Preprints, American Chemical Society 2001, 42(2), 67-98.

167. Oliveira, A. E. F.; Braga, G. B.; Tarley, C. R. T.; Pereira, A. C., Thermally reduced graphene oxide: synthesis, studies and characterization. Journal of Materials Science 2018, 53 (17), 12005-12015.

168. Yu, W.; Fu, J.; Dong, X.; Chen, L.; Shi, L., A graphene hybrid material functionalized with POSS: synthesis and applications in low-dielectric epoxy composites. Composites Science and Technology 2014, 92, 112-119.

169. Divakaran, N.; Kale, M. B.; Senthil, T.; Mubarak, S.; Dhamodharan, D.; Wu, L.; Wang, J., Novel unsaturated polyester nanocomposites via Hybrid 3D POSS-modified graphene oxide reinforcement: electro-technical application perspective. Nanomaterials (Basel) 2020, 10 (2).

170. Zhang, M.; Yan, H.; Yuan, L.; Liu, C., Effect of functionalized graphene oxide with hyperbranched POSS polymer on mechanical and dielectric properties of cyanate ester composites. Royal Society of Chemistry Advances 2016, 6 (45), 38887-38896.

171. Zhang, R. L.; Gao, B.; Du, W. T.; Zhang, J.; Cui, H. Z.; Liu, L.; Ma, Q. H.; Wang, C. G.; Li, F. H., Enhanced mechanical properties of multiscale carbon fiber/epoxy composites by fiber surface treatment with graphene oxide/polyhedral oligomeric silsesquioxane. Composites Part A: Applied Science and Manufacturing 2016, 84, 455-463.

172. Lu, Y.; Zhang, S.; Geng, Z.; Zhu, K.; Zhang, M.; Na, R.; Wang, G., Hybrid formation of graphene oxide–POSS and their effect on the dielectric properties of poly(aryl ether ketone) composites. New Journal of Chemistry 2017, 41 (8), 3089-3096.

173. Ata, S.; Banerjee, S. L.; Singha, N. K., Polymer nano-hybrid material based on graphene oxide/POSS via surface initiated atom transfer radical polymerization (SI-ATRP): Its application in specialty hydrogel system. Polymer 2016, 103, 46-56.

174. Kulkeratiyut, S.; Kulkeratiyut, S.; Blum, F. D., Bound carbonyls in PMMA adsorbed on silica using transmission FTIR. Journal of Polymer Science Part B: Polymer Physics 2006, 44 (15), 2071-2078.

175. Zhang, X.; Wang, J.; Jia, H.; Yin, B.; Ding, L.; Xu, Z.; Ji, Q., Polyvinyl pyrrolidone modified graphene oxide for improving the mechanical, thermal conductivity and solvent resistance properties of natural rubber. RSC Advances 2016, 6 (60), 54668-54678.

176. Huang, J.; Xie, G.; Zhou, Y.; Xie, T.; Tai, H.; Yang, G., Polyvinylpyrrolidone/reduced graphene oxide nanocomposites thin films coated on quartz crystal microbalance for NO2 detection at room temperature. SPIE: 2014; Vol. 9285.

177. Blum, F. D.; Young, E. N.; Smith, G.; Sitton, O. C., Thermal analysis of adsorbed poly(methyl methacrylate) on silica. Langmuir 2006, 22 (10), 4741-4744.

178. Kabomo, T.; Blum, F., Glass transition behavior of PMMA thin films. Polymer Preprints, American Chemical Society 2001, 42 (2), 67-68.

179. El Achaby, M.; Essamlali, Y.; El Miri, N.; Snik, A.; Abdelouahdi, K.; Fihri, A.; Zahouily, M.; Solhy, A., Graphene oxide reinforced chitosan/polyvinylpyrrolidone polymer bio-nanocomposites. Journal of Applied Polymer Science 2014, 131 (22), 41042-41053.

180. Justh, N.; Berke, B.; László, K.; Szilágyi, I. M., Thermal analysis of the improved Hummers' synthesis of graphene oxide. Journal of Thermal Analysis and Calorimetry 2017, 131 (3), 2267-2272.

181. Salavagione, H. J.; Martínez, G.; Gómez, M. A., Synthesis of poly(vinyl alcohol)/reduced graphite oxide nanocomposites with improved thermal and electrical properties. Journal of Materials Chemistry 2009, 19 (28).

182. Kuila, T.; Bose, S.; Hong, C. E.; Uddin, M. E.; Khanra, P.; Kim, N. H.; Lee, J. H., Preparation of functionalized graphene/linear low density polyethylene composites by a solution mixing method. Carbon 2011, 49 (3), 1033-1037.

183. Mortazavian, H.; Fennell, C. J.; Blum, F. D., Structure of the interfacial region in adsorbed poly(vinyl acetate) on silica. Macromolecules 2015, 49 (1), 298-307.

184. Khatiwada, B. K.; Blum, F. D., Tightly bound PMMA on silica has reduced heat capacities. Langmuir 2019, 35 (35), 11482-11490.

185. Cassu, S. N.; Felisberti, M. I., Poly(vinyl alcohol) and poly(vinyl pyrrolidone) blends: miscibility, microheterogeneity and free volume change. Polymer 1997, 38 (15), 3907-3911.

186. Kurakula, M.; Rao, G., Pharmaceutical assessment of polyvinylpyrrolidone (PVP): As excipient from conventional to controlled delivery systems with a spotlight on COVID-19 inhibition. J Drug Deliv Sci Technol 2020, 60, 102046.

187. Sargsyan, A. G.; Tonoyan, A.; Davtyan, S.; Schick, C., The amount of immobilized polymer in PMMA SiO2 nanocomposites determined from calorimetric data. European Polymer Journal 2007, 3113-3127.

188. Mortazavian, H.; Fennell, C. J.; Blum, F. D., Structure of the interfacial region in adsorbed poly(vinyl acetate) on silica. Macromolecules 2016, 49 (1), 298-307.

189. Montes-Navajas, P.; Asenjo, N. G.; Santamaria, R.; Menendez, R.; Corma, A.; Garcia, H., Surface area measurement of graphene oxide in aqueous solutions. Langmuir 2013, 29 (44), 13443-8.

190. http://polymerdatabase.com/polymers/polyvinylpyrrolidone.html.

191. Tang, C.; Yan, H.; Li, S.; Li, M.; Chen, Z., Novel phosphorus-containing polyhedral oligomeric silsesquioxane functionalized Graphene oxide: preparation and its performance on the mechanical and flame-retardant properties of bismaleimide composite. Journal of Polymer Research 2017, 24 (10).

192. Qu, L.; Sui, Y.; Zhang, C.; Li, P.; Dai, X.; Xu, B.; Fang, D., POSS-functionalized graphene oxide hybrids with improved dispersive and smoke-suppressive properties for epoxy flame-retardant application. European Polymer Journal 2020, 122.

193. Jiang, D.; Xing, L.; Liu, L.; Yan, X.; Guo, J.; Zhang, X.; Zhang, Q.; Wu, Z.; Zhao, F.; Huang, Y.; Wei, S.; Guo, Z., Interfacially reinforced unsaturated polyester composites by chemically grafting different functional POSS onto carbon fibers. Journal of Materials Chemistry A 2014, 2 (43), 18293-18303.

194. Vijayakumar, V.; Son, T. Y.; Kim, H. J.; Nam, S. Y., A facile approach to fabricate poly(2,6-dimethyl-1,4-phenylene oxide) based anion exchange membranes with extended alkaline stability and ion conductivity for fuel cell applications. Journal of Membrane Science 2019, 591, 1-11.

195. Zhang, X.; Ma, R.; Du, A.; Liu, Q.; Fan, Y.; Zhao, X.; Wu, J.; Cao, X., Corrosion resistance of organic coating based on polyhedral oligomeric silsesquioxane-functionalized graphene oxide. Applied Surface Science 2019, 484, 814-824.

196. Oliveira, A. E. F.; Braga, G. B.; Tarley, C. R. T.; Pereira, A. C., Thermally reduced graphene oxide: synthesis, studies and characterization. Journal of Materials Science 2018, 53 (17), 12005-12015.

197. Yu, W.; Fu, J.; Dong, X.; Chen, L.; Shi, L., A graphene hybrid material functionalized with POSS: synthesis and applications in low-dielectric epoxy composites. Composites Science and Technology 2014, 92, 112-119.

198. Mark, J. E., Physical properties of polymers handbook. Springer New York, NY: p 1076.

VITA

Ishan Niranga, Jayalath Arachchige don

Candidate for the Degree of

Doctor of Philosophy

Dissertation: SYNTHESIS, CHARACTERIZATION, AND APPLICATION OF STARCH AND GRAPHENE OXIDE DERIVATIVES FOR POLYMERS

Major Field: Chemistry

Biographical:

Education:

Completed the requirements for the Doctor of Philosophy in Chemistry at Oklahoma State University, Stillwater, Oklahoma in December, 2022.

Completed the requirements for the Master of Science in Analytical Chemistry at the University of Colombo, Colombo, Sri Lanka in 2016.

Completed the requirements for the Bachelor of Science in Chemistry at the Institute of Chemistry, Colombo, Sri Lanka in 2012.